The Hashemite Kingdom of Jordan Scientific Research Support Fund The Hashemite University

JJEES

Jordan Journal of Earth and Environmental Sciences

Indexed by Scopus

ELSEVIER

Volume (14) Number (3)

Cover photo © Prof. Ghaleb Jarrar

JJEES is an International Peer-Reviewed Research Journal

ISSN 1995-6681 jjees.hu.edu.jo September 2023

Jordan Journal of Earth and Environmental Sciences (JJEES)

JJEES is an International Peer-Reviewed Research Journal, Issued by Deanship of Scientific Research, The Hashemite University, in corporation with, the Jordanian Scientific Research Support Fund, the Ministry of Higher Education and Scientific Research.

Submission address:

Manuscripts should be submitted electronically to the following e-mail:

jjees@hu.edu.jo

For more information and previous issues:

www.jjees.hu.edu.jo

Hashemite Kingdom of Jordan

Scientific Research Support Fund

Hashemite University

Jordan Journal of Earth and Environmental Sciences

JJEES

An International Peer-Reviewed Scientific Journal

Financed by the Scientific Research Support Fund

Volume 14 Number (3)

http:// jjees.hu.edu.jo/

ISSN 1995-6681

Precambrian basement rocks including: metamorphic rocks, granites, and different generations of dikes, at Wadi Rahma, 45 km north of Aqaba.
Photographed by Prof. Ghaleb Jarrar

JJEES

Jordan Journal of Earth and Environmental Sciences

JJEES (2023) 14 (3): 175-181
ISSN 1995-6681

Analysis of Rainfall Trends in Three Selected Rain Gauging Stations from WL3, IL1a, and DL1f Agroecological Regions in Srilanka

Latheef Fathima Zisath Shama[1] and Mohamed M. M. Najim[2*]

[1]Department of Information and Communication Technology, Faculty of Technology, South Eastern University of Sri Lanka, Oluvil, Sri Lanka.
[2] Faculty of Agriculture, Sultan Sharif Ali Islamic University, Kampus Sinaut, Km 33, Jalan Tutong, Tutong TB1741, Brunei.

Received 7th February 2022; Accepted 26th September 2022

Abstract

Rainfall is the primary resource for freshwater. Changes in the rainfall trend pattern influence the economic development of the country by tremendously affecting different economic sectors due to the absence or shifting of rainfall at particular periods of the year. This research aims to find the monthly, seasonal, and annual trend in the precipitation pattern and the relationship between the precipitation and time in Keragala, Bingiriya, and Mahawilachchiya in Sri Lanka in the Agroecological Region WL3, IL1a, DL1f, respectively. Daily Rainfall data were collected from 1961 to 2005 from the selected rainfall gauging stations. The Mann-Kendall test and the Augmented Dickey-Fuller test indicate the stationarity of rainfall. Keragala and Bingiriya show the annually insignificant increasing trend and Mahawilachchiya shows the annually insignificant decreasing rainfall trend. Different seasons show different trends in different agroecological regions. These changes show that climate change has influenced the rainfall trends and hence some impacts are faced by the agriculture and aquaculture sector in the country due to these trend changes, even though those are statistically insignificant. Climate change has taken up an inordinate primary place in the water management system.

Keywords: *Trend analysis; Non-parametric test; Mann-Kendall trend; Sen's slope; Augmented Dickey-Fuller Test; Rainfall pattern*

1. Introduction

The amount of precipitation is a very important factor for those living all over the world. Knowledge of trends in precipitation and environmental changes is important to those who are interested in precipitation, its variation, and patterns related field (Wickramagamage, 2016; Aanderud et al., 2010). Precipitation trends play the primary role in precipitation analysis. While planning agricultural activities, rainfall frequency and the amount of water available through rainfall are considered very important factors (Ekanayake and Perera, 2014; Radaideh et al., 2009). Therefore, water is a critical concern for the farmers and timely rainfall is a major concern in land preparation water management (Lee et al., 2005). Extreme events based on rainfall also play a very important role in agriculture. Extreme floods and droughts affect the agriculture sector badly (Panda and Sahu, 2019). A trend is defined as a sequence of changes over time that are influenced by numerous variables in the series. In terms of variation in rainfall across time, rainfall time series can be defined as stationary or non-stationary. The time series is termed stationary if the averages and variances of rainfall do not vary significantly over the period (Nashwan et al., 2019). The time series has inconsistent patterns in the means or variances of rainfall over time defines as nonstationary (Nashwan et al., 2019).

Researchers are using many different data analysis techniques to find the trends in rainfall and forecast rainfall amounts but this task is very difficult (Burt and Weerasinghe, 2014). Precipitation varies according to months and seasons in every agroecological region. Nowadays, traditional rainfall patterns have changed due to many environmental factors and social factors (Pani et al., 2016). Recent past precipitation records help to find the trend and any relationship that prevail between the months and amounts of precipitation (Jayawardene et al., 2005). Finding the trend helps in water management (Manawadu and Fernando, 2008; Adler et al., 2017). There are two types of trend analysis which are, temporal and spatial. Temporal trend analysis is a technique for modeling and analyzing data over time (Şen, 2017a; Şen, 2017b).

As the Sri Lankan economy is dependent on agricultural products and hydropower, a conducive climate is mostly expected. The analysis of long-term changes in precipitation fluctuations is a fundamental task in studies on climate change detection (Karunathilaka et al., 2017). The understanding of past and recent precipitation trends has obtained significant interest through upgrades and extensions of many datasets and more advanced data analyses (Panda and Sahu, 2019). Further, anthropogenic activities have led to a decrease in the availability of freshwater sources (Al-Shibli et al., 2017; Obeidat and Awawdeh, 2021) . Therefore, maintaining and planning water resources has become crucial. Predicting the fluctuations in spatial and temporal variabilities in rainfall is essential to formulate effective management strategies in the management of water resources (Kaba et al., 2020).

Sri Lanka has been divided into three zones according

* Corresponding author e-mail: najim.mujithaba@unissa.edu.bn

to annual rainfall received, that are Wet Zone (annual precipitation > 2500 mm), Intermediate Zone (annual precipitation between 2500 mm and 1750 mm), and Dry Zone (annual precipitation <1750 mm) (Burt and Weerasinghe, 2014). The precipitation patterns in the three climatic zones have changed differently and the differences of these zones need to be investigated. Identification of changes in historical rainfall trends is important in climate change investigation (Pani et al., 2016). The most important physical parameter in climate change is rainfall variation (Manawadu and Fernando, 2008; Panda and Sahu, 2019). The analysis of long-term changes in rainfall is a fundamental task in studies on climate change detection. Rainfall trend investigations exhibit increasing or decreasing trends in Sri Lanka and which is most relevant to agriculture (Nisansala et al., 2020).

In addition, freshwater availability and changes in rainfall patterns affect biodiversity (Dinpashoh et al., 2011). On random certain days, extreme rainfall can be received due to sudden natural phenomena and extreme drought can also occur but the extreme drought is an accumulation of several natural phenomena for a longer term. The occurrence of drought has become more frequent in recent years (Wickramagamage, 2016). These are unavoidable circumstances in natural phenomena (Ahmad et al., 2015; Karunathilaka et al., 2017).

Jayawardene et al. (2005) analyzed 100 years of rainfall records from 15 rainfall stations in Sri Lanka to examine the annual trend of rainfall. The data set was divided into two categories which were short-term and long-term. They used a Mann-Kandall trend test, the Spearman rank statistic, and the regression slope methods in their analysis. However, during the previous century, no consistent growth or decline in trends was recorded for the stations in the wet and dry zones. Alahacoon and Edirisinghe (2021) analyzed the spatial variability of rainfall trends in Sri Lanka from 1989 to 2019. The Mann–Kendall test and Sen's slope estimators were used to study the trends in annual and seasonal rainfall across all the districts and climatic zones of Sri Lanka. The wet zone has the highest increasing trend, while the semi-arid zone has the lowest increasing trend. However, the results of The Mann–Kendall trend test show that there is an increase in rainfall in all the districts in Sri Lanka during the South West Monsoon. Nisansala et al., (2020) examined trend analysis of rainfall over Sri Lanka from 1987 to 2017 using Innovative Trend Analysis (ITA) and Mann Kendall test (MK) with Sen's slope estimator. The result shows that the eastern, south-eastern, north, and north-central regions of the country showed increasing rainfall trends while the western, part of the northwestern, and central parts of the country indicated a decreasing rainfall trend.

Wickramagamage (2016) analyzed daily rainfall records from 1981 to 2010 to identify the spatial pattern of rainfall trends using linear regression. This study illustrates that the rainfall trends of the Southwest Monsoon season are largely positive across the country. The Northeast and the Central Highlands had the most significant negative trends. The Inter-Monsoon (IM) periods have mostly positive tendencies practically everywhere, but there are still some negative trends in the highlands and Northeast region. Sayd et al. (2020) illustrated the rainfall trend in Nigeria using Pearson's Product Moment Correlation using 27 years of rainfall data. They showed a decreasing trend in the annual mean rainfall in the Kilange catchment in Nigeria. Salahat et al. (2015) analyzed the rainfall fluctuations in Jordan using Monthly rainfall data for the period from 1961 to 2012 using 22 weather stations covering the whole country. Salahat et al. (2015) analyzed ten years of moving average aridity trends and tested using the Tukey test, Mann-Kendall rank, and simple linear regression. According to the historical trend analysis, the overall rainfall trend is significantly decreasing in Jordan.

Literature gives information about the rainfall trend in Sri Lanka, but those studies did not talk about the monthly, seasonal, and annual rainfall trends in selected agro-ecological regions WL3, IL1a, and DL1f in Sri Lanka. Moreover, in addition to the Mann-Kendall trend test, this study attempted to analyze the stationarity of rainfall trends using the Augmented Dickey-Fuller test. The aim of this study focuses on extracting the trends, magnitudes of trends, and the stationarity of the rainfall data based on the monthly and seasonal pattern of rainfall on a set of selected weather stations by utilizing selected statistical techniques, where three selected rain gauging stations from three climatic zones which are, Bingiriya from Intermediate zone, Keragala from the wet zone and Mahawilachchiya from the dry zone were used.

2. Materials and methods

2.1 Study Sites and precipitation data collection

Daily precipitation records at Bingiriya, Keragala, and Mahawilachchiya rainfall stations in Low Country Intermediate Zone (IL), Low Country Wet Zone (WL), and Low Country Dry Zone (DL), respectively were collected for the period from 1961 to 2005 from the Department of Meteorology, Colombo. To understand the trend and the pattern of precipitation, daily precipitation records for 45 years (from 1961 to 2005) because of the availability of data were used in this study from randomly selected three rain gauging stations from three main climate zone in Sri Lanka which are, Bingiriya (7.62N, 79.95E) is located in IL1a Agro-Ecological Regions (AER) in Kurnuegala district. Keragala (6.80N, 80.36E) is located in WL3 AER in Rathnapura district, and Mahawilachchiya lies (8.48N, 80.18E) in DL1f AER in Anuradhapura district. Figure 01 illustrates the places on the Sri Lanka geographical map.

Very few amounts of missing data were supplemented by records from the nearest rain gauge. Missing data were a single day or a few consecutive days' data. The r software tool was used to calculate the Mann-Kendall statistics and the Augmented Dickey-Fuller test for the three AERs. These data were grouped into twelve calendar months and four seasons; North East monsoon (December, January, February), South West monsoon (May, June, July, August, September), First inter monsoon (March, April), Second inter monsoon (October, November).

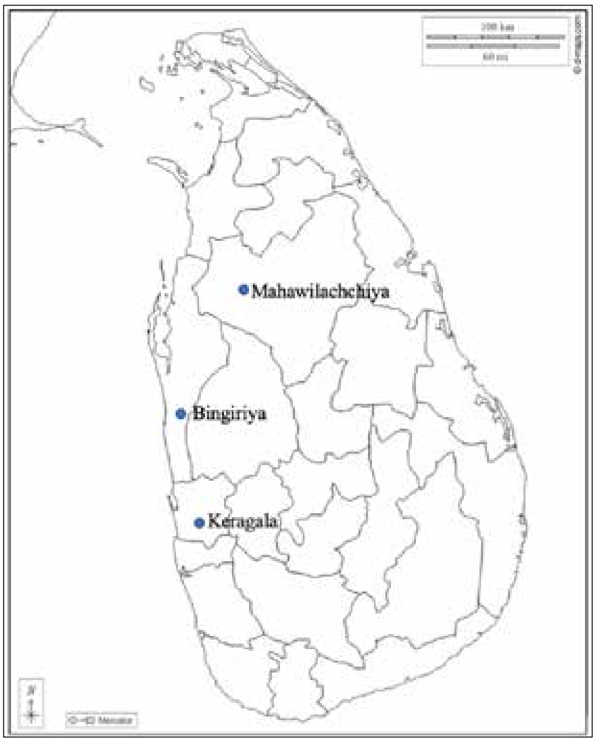

Figure 1. Selected rain gauges in Sri Lanka map

2.2 Mann-Kendall trend test

The Mann-Kendall trend test is the mostly used method to detect the trend in the data series. Parametric tests are more powerful than the non-parametric tests in trend analysis but require the data to be independent and normally distributed, which is rarely obtained for precipitation time series data (Karunathilaka et al., 2017; Prashanth, 2005) Mann-Kendall test is one of the non-parametric tests for diagnostic trends in the time series data. The advantage of this method is that it does not need to conform to the distribution and this test is not affected by the outliers in the data sample (Adler et al., 2017). Mann-Kendall values are calculated by comparing all subsequent data in the time series. Positive values of Mann-Kendall statistics indicate an increasing trend while negative values indicate a decreasing trend in the time series. The Z value indicates whether there are any significant trends in the series (Khambhammettu, 2005).

In this paper, the Mann-Kendall test and Sen's slope estimator methods were used to find the trend and magnitudes of the trends of rainfall distribution in the selected AERs (Khambhammettu, 2005). Mann- Kendall trend test is used to find the monotonic trend in the data series as well as Sen's slope helps to find the magnitude of the trend that appears in the data set.

If the trend in precipitation is monotonically decreasing, then the Z is negative and the computed probability value is greater than the significant level. If the Z value is negative but the computed probability value is not exceeding the significant level then it is a non-monotonically decreasing trend. If the trend is monotonically increasing, then the Z is positive and the computed probability value is greater than the significant level. If the Z value is positive but the computed probability value is not exceeding the significant level then it is a non-monotonically increasing trend.

Let x1, x2, … xn represent n data points where xj represents the data point at time j; n is the number of data points in the dataset, then the Mann-Kendall statistic (S) is given by,

$$S=\sum_{k=1}^{n-1}\sum_{j=k+1}^{n} sign\,(x_j - x_k) \quad \text{......} (1)$$

Sign(x_j-x_k) is indicated as,

$$\text{Sign}(x_j\text{-}x_k)=\begin{cases} =1\,;\ x_j - x_k > 0 \\ =0\,;\ x_j - x_k = 0 \\ =-1\,;\ x_j - x_k < 0 \end{cases} \quad \text{......} (2)$$

The procedure to calculate the Mean of S (E(S)) and Variance of S (Var(S)) is given as,

$$E(S)=0$$

$$\text{Var}(S)=\begin{cases} \frac{(n(n-1)(2n+5))}{18} & ;no\ ties \\ \frac{n(n-1)(2n+5)-\sum_{p-1} t_p(t_p-1)(2t_p+5)}{18} & ;tie\ is\ present \end{cases} \quad (3)$$

Where,

p- tied ranks

t_p- number of times that the rank p appears (i.e., frequency)

The standardized statistic (Z) of S for a one-tailed test is given as follows,

$$Z=\begin{cases} \frac{S-1}{[Var(S)]^{\frac{1}{2}}} & ;S>0 \\ 0 & ;\ S=0 \\ \frac{S+1}{[Var(S)]^{\frac{1}{2}}} & ;s<0 \end{cases} \quad \text{......} (4)$$

The probability density function for a normal distribution with a mean of 0 and a standard deviation of 1 is,

$$f(z)=\frac{1}{\sqrt{2\pi}}e^{\frac{-z^2}{2}} \quad \text{......} (5)$$

If Z is negative and the computed probability is greater than the level of significance, then the trend is said to be monotonically decreasing. If the Z is positive and the computed probability is greater than the level of significance, then the trend is said to be monotonically increasing. If the computed probability is less than the level of significance, there is no trend.

Kendall's tau indicates the statistical relation based on the ranks of the data, further, it ranges between -1 to 1. The positive values of Kendall's tau confirmed an increasing trend on the other hand and the negative values of Kendall's tau confirmed a decreasing trend in the data set (Tarawneh and Chowdhury, 2018).

Sen's slope estimator is used to estimate the magnitude of the trend. In this method, a linear model is assumed.

$$f(t)=Qt+C \quad \text{......} (6)$$

Where C is a constant, the slope of all data pairs is calculated as,

$$Q_i=\frac{x_i-x_j}{i-j}\,;\ i=1,2,3\ldots\ldots,N \quad \text{......} (7)$$

x_i, x_j are the values at times i and j further i>j.

The median of these N values of is Sen's estimator (Q) of the slope, which is calculated as,

$$Q=\begin{cases} Q_{\left(\frac{N+1}{2}\right)}; N \text{ is odd} \\ \frac{1}{2}\left(Q_{\left(\frac{N}{2}\right)} + Q_{\left(\frac{N+1}{2}\right)}\right); N \text{ is even} \end{cases} \quad (8)$$

A positive value of Q indicates an upward trend and a negative value indicates a downward trend in the time series.

The hypothesis is,

H_0: There is no trend in the rainfall

H_1: There is a trend in the rainfall

The null–hypothesis is rejected if where is taken from the standard normal distribution table and α is the level of significance. The statistic was calculated as 1.96 at 5% of the significant level using the normal probability distribution table. When > 1.96, the rainfall will have a significantly increasing trend when < -1.96, the rainfall will have a significantly decreasing trend. Sen's Slope is used to find the magnitude of the trend (Karunathilaka et al., 2017). In R software, the Precintcon package was used to perform the Mann-Kendall analysis for the three agroecological regions separately.

2.3 Stationary test

If a series has a constant mean and variance at a level that stationary series besides nonstationary series has changing mean and variance (Nashwan et al., 2019). Augmented Dickey Fuller Test was used to test the stationarity in the rainfall time series data (Dickey and Fuller, 1979). The average monthly rainfall and average seasonal and annual rainfall were used to find the stationarity. The null hypothesis of this test is the time series is not stationary and the test was conducted at 0.05 significance level. Thus, the null hypothesis is rejected when the P value is smaller than the significant level (Nashwan et al., 2019; Dickey and Fuller, 1979).

A stationary error and random walk is expressed as,

$$X_t=r_t+\beta_t+\varepsilon_t \quad (9)$$

where,

X_t – Linear regression

r_t – Random walk

β_t – Deterministic trend

ε_t – Stationary error

A Dicky Fuller Regression is considered as,

$$\Delta x_n = \alpha + \beta t + \gamma x_{t-1} + \sum_{j=1}^{p}\left(\delta_t \Delta x_{t-j}\right) + e_t \quad (10)$$

where

Δx- differenced series at a lag of n years,

α - Drift,

β - Represents the coefficient on a time trend

p- Lag order autoregressive process

γ - Process root coefficient

δ_t- lag operator

e_t- Residual term

Residual is an independent identical distribution residual term with mean zero and constant variance σ^2.

3. Results and discussion

Table 1 interprets the results of the Mann-Kendall trend test in the Mahawilachchiya. This result revealed negative trends in February, March, May, July, August, September, October, December, South West monsoon, North East monsoon, Second inter monsoon as well as annual precipitation while the first inter monsoon is showing a positive trend. The Sen's estimator which is to measure the magnitude of rainfall was found as 0.38mm/y, 0.53mm/y, 0.63mm/y, 1.5 mm/y, 1.4 mm/y for South West monsoon, First inter monsoon, North East monsoon, second inter monsoon and annual rainfall, respectively. Highly insignificant increasing and decreasing trends appear in April as 1.05 mm/y, and in December as 1.92 mm/y in Mahawilachchiya. Moreover, the Tau value also indicates that downward trends persist in February, March, May, July, August, September, October, December, South West monsoon, North East monsoon, Second inter monsoon as well as annual precipitation, and also upward trends persist in January, April, June, November and First inter monsoon. Liyanaarachchi et al. (2017) attempted to identify trends of seasonal rainfall anomalies with the aid of SPI values calculated for different time scales and they suggested that Dry zone AER DL1f shows a significant increasing trend in the First inter monsoon rainfall anomalies. They also showed that the Second inter monsoon rainfall anomalies show a significantly increasing trend. Jayawardene et al. (2005) exhibited non-significant trends in rainfall by Mann-Kendall and Spearmann's test to the higher inter-annual variability of rainfall at this location. Karunathilaka et al. (2017) suggested that a significantly increasing trend was detected in the first inter-monsoon and annual rainfall, a non-significant decreasing trend in South West monsoon, a non-significant increasing trend in the second inter-monsoon and North East monsoon by Mann Kendall trend test.

Table 1. Result of Mann-Kendall analysis at Mahawilachchiya

Month and Season	Z-Value	Sen's slope	S	P-value	Tau
January	1.2658	0.2333	126	0.2056	0.1273
February	-0.0986	-0.0221	-11	0.9215	-0.0111
March	-1.5365	-0.5829	-158	0.1244	-0.1596
April	1.1054	1.0515	114	0.269	0.1152
May	-0.1859	-0.1274	-20	0.8526	-0.0202
June	1.2658	0.0121	126	0.2056	0.1273
July	-0.4063	-0.0133	-42	0.6845	-0.0424
August	-1.6315	-0.0111	-160	0.1028	-0.1616
September	-0.0392	-0.2910	-5	0.9688	-0.0051
October	-0.4402	-0.5375	-46	0.6598	-0.0465
November	0.0098	0.075	2	0.9922	0.002
December	-1.575	-1.9253	-162	0.1153	-0.1636
First inter monsoon	0.4011	0.5332	42	0.6884	0.0424
South West monsoon	-0.3815	-0.3812	-40	0.7028	-0.0404
Second inter monsoon	-0.7728	-1.465	-80	0.4396	-0.0808
North-East monsoon	-0.2837	-0.6291	-30	0.7767	-0.0303
Annual	-0.4989	-1.4117	-52	0.6179	-0.0525

Table 2 illustrates the results of the Mann-Kendall test at Keragala station. April, August, the First inter monsoon, and South West monsoon have a decreasing trend in rainfall. Kendall's Tau indicated increasing trends in January, February, March, May, June, July, September, October, November, Second inter monsoon, North East monsoon, and the Annual precipitation. November has a high amount of increasing trend at 2.93 mm/y whereas August has a high amount of decreasing at 1.31mm/yr. Although Jayawardene et al. (2005) used the Mann-Kendall test and Spearman's test to find the rainfall trend, they suggested that the annual trend exhibits a non-significant downward trend. Karunathilaka et al. (2017) suggested that a non-significant increasing trend was detected in the first inter-monsoon, second inter-monsoon, North East monsoon, and annually, and a non-significant decreasing trend in South West monsoon by Mann Kendall trend test.

Table 2. Result of Mann-Kendall analysis at Keragala

Month and Season	Z-Value	Sen's slope	S	P-value	Tau
January	0.8706	1.8768	90	0.384	0.0909
February	0.8414	0.9805	87	0.4001	0.0879
March	0.6163	0.9163	64	0.5377	0.0646
April	-0.4402	-1.0261	-46	0.6598	-0.0465
May	0.5967	1.6525	62	0.5507	0.0626
June	0.8706	1.8768	90	0.384	0.0909
July	0.2641	0.5453	28	0.7917	0.0283
August	-0.5185	-1.313	-54	0.6041	-0.0545
September	0.4011	1.6212	42	0.6884	0.0424
October	0.7337	1.6029	76	0.4631	0.0768
November	1.7315	2.9316	178	0.0834	0.1798
December	0.4793	0.7912	50	0.6317	0.0505
First inter monsoon	-0.675	-2.251	-70	0.4997	-0.0707
South West monsoon	-0.4402	-2.9225	-46	0.6598	-0.0465
Second inter monsoon	1.3793	4.5845	142	0.1678	0.1434
North-East monsoon	1.1054	2.3807	114	0.269	0.1152
Annual	0.7728	4.6564	80	0.4396	0.0808

Table 3 is showing the results of the Mann-Kendall test at Bingiriya. Table 3 indicated that February, March, May, July, August, September, and December, first inter-monsoon, North East and South West monsoon seasons show decreasing trends in precipitation. January, April, June, October, and November, the Second inter-monsoon as well as Annual precipitation show an increasing trend. November shows a highly increasing trend of 3.65 mm/y while May has a highly decreasing magnitude trend of 0.78 mm/y. The annual magnitude of the trend is 2.65 mm/y. Furthermore, Tau values also exhibit downward trends in February, March, May, July, August, September, and December, first inter-monsoon, North East and South West monsoon seasons and upward trends in January, April, June, October, November, Second inter-monsoon and annually. Udayanga and Najim (2014) also suggested a significant decrease in the dry events while a significant increase in wet events at Bingiriya, annually. However, Liyanaarachchi et al. (2017) attempted to identify any trends of seasonal rainfall anomalies with the aid of SPI values calculated for different time scales and they suggested that the Intermediate Zone IL1a showed a significant increasing trend in the Second inter-monsoon and North East monsoon rainfall anomalies.

Table 3. Results of Mann-Kendall analysis at Bingiriya

Month and Season	Z-Value	Sen's slope	S	P-value	Tau
January	0.2446	0.1608	26	0.8068	0.0263
February	-0.8529	-0.3238	-88	0.3937	-0.0889
March	-0.8022	-0.6353	-83	0.4224	-0.0838
April	0.1467	0.1488	16	0.8833	0.0162
May	-0.5576	-0.7896	-58	0.5771	-0.0586
June	0.2446	0.1608	26	0.8068	0.0263
July	-0.8119	-0.4115	-84	0.4168	-0.0848
August	-0.0294	-0.0057	-4	0.9766	-0.004
September	-0.0489	-0.0364	-6	0.961	-0.0061
October	0.7337	1.6253	76	0.4631	0.0768
November	1.937	3.6518	199	0.0527	0.201
December	-1.1054	-0.7338	-114	0.269	-0.1152
First inter monsoon	-0.1076	-0.2521	-12	0.9143	-0.0121
South West monsoon	-0.988	-1.9572	-102	0.3231	-0.103
Second inter monsoon	1.7902	6.1646	184	0.0734	0.1859
North-East monsoon	-0.675	-0.7966	-70	0.4997	-0.0707
Annual	0.5772	2.65	60	0.5638	0.0606

When the trends among the three AERs are compared for the four seasons and annual precipitation, Mahawilachchiya has shown an increasing trend while Keragala and Bingiriya have shown decreasing trends in the First inter monsoon. South West monsoon period shows a decreasing trend in all three stations. Mahawilachchiya has shown a decreasing trend whereas Keragala and Bingiriya have shown an increasing trend in the Second inter monsoon. Keragala has shown an increasing trend in the North East monsoon. Mahawilachchiya only shows a decreasing trend whereas Keragala and Bingiriya show increasing trends in annual rainfall. The increasing trends are higher than the decreasing trends, in all three stations. Further, annual rainfall trend analysis for the Mahawilachchiya is interesting to appraise water scarcity in future climate scenarios. The dry area would be drier in the future. At the same time, In Bingiriya and Keragala, the annual rainfall trend shows that it can be justified that water availability in the catchment was not affected over the 45 years and will not have a lack of water availability future. Furthermore, the wet zone and the intermediate zone would be wetter in the future.

According to Figure 2, the bimodal rainfall pattern due to both the monsoons is apparent at the three stations. Monthly precipitation at Keragala station has two peak points and the wet months are April, May, June, September, and October. The dry months are January and February. March is the transition month from the dry season to the wet season and December is the transition month from the wet season to the dry season. January has the lowest and May has the highest monthly mean rainfall. In Mahawilachchiya, the dry months are January, February, March, June, July, and August. April, October, November, and December are the wet months. March and September are the transition months from the dry season to the wet season and May and January are the transition months from the wet season to the dry season. June has the lowest and November has the highest monthly average rainfall. Monthly analysis of Bingiriya rainfall shows that October, November, April, and May are the wet season months, while the dry season months are January, February, July, and August. September is the transition month from the dry season to the wet season and December is the transition month from the wet season to the dry season. Monthly analysis of Bingiriya and Mahawilachchiya stations show a prominent bi-model pattern in April, May, and October, and November having peak precipitation.

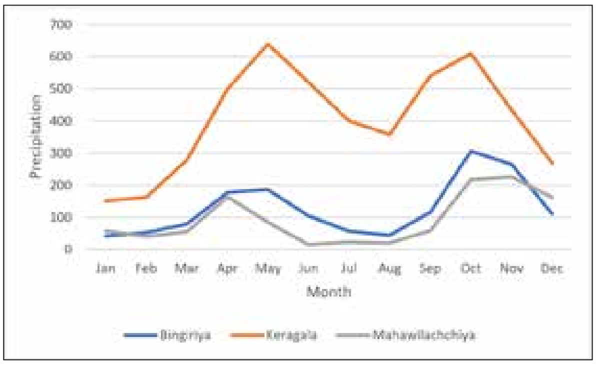

Figure 2. Monthly spatial rainfall at the three rain gauging stations

The results for the Augmented Dickey-Fuller test for monthly, seasonal, and annual average rainfall of selected rain gauges are shown in Table 4. In the Mahawilachchiya, January, March, May, June, July, and the First inter-monsoon were noted as stationary besides, other months and seasons were noted as non-stationary in rainfall pattern. August and September months have shown the highest changing rate of nonstationary monthly rainfall, P-values for August and September were higher than other months. Therefore, South West monsoon also appeared the highest rate of nonstationary.

Table 4. P –Values of Augmented Dickey Fuller Test at each station

Month and Season	P –Values		
	Mahawilachchiya	Keragala	Bingiriya
January	0.01	0.04944	0.05371
February	0.1363	0.01784	0.02872
March	0.04977	0.715	0.491
April	0.3035	0.9782	0.01047
May	0.01	0.06753	0.07357
June	0.01	0.3678	0.04739
July	0.01	0.01	0.01575
August	0.439	0.1554	0.02754
September	0.495	0.04733	0.07081
October	0.2466	0.2243	0.09831
November	0.1717	0.5491	0.07717
December	0.189	0.3653	0.14
North-East Monsoon	0.1314	0.99	0.03873
First inter Monsoon	0.03374	0.267	0.02984
South West Monsoon	0.2854	0.3747	0.08439
Second inter Monsoon	0.06782	0.1062	0.1066
Annual	0.08051	0.3903	0.2372

According to the results shown in Table 4, in Keragala station, January, February, July, and September months were shown a stationary rainfall pattern, on the other hand, other moths were shown a nonstationary rainfall pattern. March and April were shown the highest rate of nonstationary monthly average rainfall, with P-values noted as extremely large. Therefore, the First inter monsoon was also noted as having the highest rate of nonstationary.

In the Bingiriya station, February, April, June, July, and August were noted as stationary as well as other months and seasons show nonstationary in the average rainfall pattern. None of the months and seasons were shown the highest rate of nonstationary monthly average rainfall. When the three stations are compared, July was shown as stationary in monthly average rainfall and all the seasons and annual rainfall are not stationary.

4. Conclusion

On an annual and seasonal scale, statistically insignificant increasing and decreasing trends in rainfall are found in the three rain gauging stations that were studied. The rainfall patterns in the three AERs WL3, IL1a, and DL1f have changed differently in each season and annually. These changes show that climate change has influenced the rainfall trends and hence some impacts are faced by the agriculture and aquaculture sector in the country due to these trend changes, even though those are statistically insignificant. In the examined rain gauges, no significant increase or decrease in rainfall was found.

Acknowledgment

The authors are grateful to the Department of Meteorology, Colombo for providing precipitation data.

References

Aanderud, Z. T., Richards, J. H., Svejcar, T., and James, J. J. (2010). A shift in seasonal rainfall reduces soil organic carbon storage in a cold desert. Ecosystems 13: 673-682.

Adler, R. F., Gu, G., Sapiano, M., Wang, J. J., and Huffman, G. J. (2017). Global precipitation: Means, variations, and trends during the satellite era (1979–2014). Surveys in Geophysics 38: 679-699.

Ahmad, I., Tang, D., Wang, T., Wang, M., and Wagan, B. (2015). Precipitation trends over time using Mann-Kendall and Spearman's rho tests in the swat river basin, Pakistan. Advances in Meteorology Article ID: 431860.

Alahacoon, N., and Edirisinghe, M. (2021). Spatial variability of rainfall trends in Sri Lanka from 1989 to 2019 as an indication of climate change. ISPRS International Journal of Geo-Information 10: 84.

Al-Shibli, F. M., Maher, W. A., and Thompson, R. M. (2017). The need for a quantitative analysis of risk and reliability for formulation of water budget in Jordan. Jordan Journal of Earth and Environmental Sciences, 8(2), 77-89.

Burt, T. P., and Weerasinghe, K.D.N. (2014). Rainfall distributions in Sri Lanka in time and space: an analysis based on daily rainfall data. Climate 2: 242-263.

Dickey, D. A., and Fuller, W. A. (1979). Distribution of the estimators for autoregressive time series with a unit root. Journal of the American statistical association 74: 427-431.

Dinpashoh, Y., Jhajharia, D., Fakheri-Fard, A., Singh, V. P., and Kahya, E. (2011). Trends in reference crop evapotranspiration over Iran. Journal of Hydrology 399: 422-433.

Ekanayake, E. M. R. S. B., and Perera, K. (2014). Analysis of drought severity and duration using copulas in Anuradhapura, Sri Lanka. British Journal of Environment and Climate Change 4: 312.

Jayawardene, H.K.W.I., Sonnadara, D. U. J., and Jayewardene, D. R. (2005). Trends of rainfall in Sri Lanka over the last century. Sri Lankan Journal of Physics 6: 7-1.

Kaba, R., and Majar, A. (2020). Spatial and Temporal Variability Analyses of Water Quality in Jaghjagh River, Syria. Jordan Journal of Earth and Environmental Sciences 11: 62-70.

Karunathilaka, K.L.A.A., Dabare, H.K.V., and Nandalal, K.D.W. (2017). Changes in rainfall in Sri Lanka during 1966–2015. Engineer: Journal of the Institution of Engineers, Sri Lanka 50: 39-48.

Khambhammettu, P. (2005). Mann-Kendall analysis for the Fort Ord site. USACE, HydroGeoLogic, Inc., Memorandum. Monterey County, CA, USA.

Lee, T.S., Haque, M.A. and Najim, M.M.M., (2005). Modeling water resources allocation in a run-of-the-river rice irrigation scheme. Water resources management 19: 571-584.

Liyanaarachchi, L.A.T.S., Wijesuriya, B.W., Sankalpa, J.K.S., Herath, H.M.L.K., Premalal, S., and Karunaratne, S.B. (2017). Identification of temporal trends in rainfall anomalies of different rainfall seasons in Sri Lanka using the Standardized Precipitation Index (SPI). In: Proceedings of The Young Scientists Forum Symposium – 2017.

Manawadu, L., and Fernando, N. (2008). Climate Change in Sri Lanka. Review Journal of the University of Colombo 1: 1–26.

Nashwan, M.S., Ismail, T., and Ahmed, K. (2019). Non-stationary analysis of extreme rainfall in peninsular Malaysia. Journal of Sustainability Science and Management, 14: 17-34.

Nisansala, W.D.S., Abeysingha, N.S., Islam, A.,and Bandara, A.M.K.R. (2020). Recent rainfall trend over Sri Lanka (1987–2017). International Journal of Climatology 40: 3417-3435.

Obeidat, M., and Awawdeh, M. (2021). Assessment of groundwater quality in the area surrounding Al-Zaatari Camp, Jordan, using cluster analysis and water quality index (WQI). Jordan Journal of Earth and Environmental Sciences, 12(3).

Panda, A., and Sahu, N. (2019). Trend analysis of seasonal rainfall and temperature pattern in Kalahandi, Bolangir, and Koraput districts of Odisha, India. Atmospheric Science Letters 20: e932.

Pani, P., Alahacoon, N., Amarnath, G., Bharani, G., Mondal, S., and Jeganathan, C. (2016). Comparison of SPI and IDSI applicability for agriculture drought monitoring in Sri Lanka. In: 37th Asian conference on remote sensing. Colombo. pp 17-21.

Prashanth, K. (2005). Mann-Kendall Analysis for the Fort Ord Site, 1155, HydroGeoLogic, Inc. Annual Groundwater Monitoring Report, California. US, Army Corps of Engineers, 1-7.

Radaideh, J., Al-Zboon, K., Al-Harahsheh, A., and Al-Adamat, R. (2009). Quality assessment of harvested rainwater for domestic uses. Jordan Journal of Earth and Environmental Sciences, 2(1), 26-31.

Salahat, M.A., and Al-Qinna, M.I. Rainfall fluctuation for exploring desertification and climate change: new aridity classification. Jordan Journal of Earth and Environmental Sciences 7: 27-35.

Sayd, D., Yonnana, E., and Mubi, A. (2020). An Analysis of Rainfall and Discharge Relationship at the River Kilange Catchment, Adamawa State, Nigeria. Jordan Journal of Earth and Environmental Sciences 11: 248-252.

Şen, Z. (2017 a). Spatial Trend Analysis. In: Innovative Trend Methodologies in Science and Engineering. Edited by Şen, Z. Springer, Cham. pp: 227-280.

Şen, Z. (2017 b). Temporal trend analysis. In: Innovative Trend Methodologies in Science and Engineering. Edited by Şen, Z. Springer, Cham. pp. 133-174

Tarawneh, Q.Y., and Chowdhury, S. (2018). Trends of climate change in Saudi Arabia: Implications on water resources. Climate 6: 8.

Udayanga, N.W.B.A.L., and Najim, M.M.M. (2014). Assessment and comparison of climatic patterns in Thanamalvila and Bingiriya (DL 1b and IL1a) regions of Sri Lanka. In: Proceedings of The Young Scientists Forum Symposium - 2013, pp. 1–5.

Wickramagamage, P. (2016). Spatial and temporal variation of rainfall trends of Sri Lanka. Theoretical and Applied Climatology 125: 427-438.

JJEES

JJEES (2023) 14 (3): 182-194
ISSN 1995-6681

Jordan Journal of Earth and Environmental Sciences

Geotechnical Investigation, Modelling and Visualization of Shallow Subsurface Soil at Khobash District, Najran, Saudi Arabia

Adnan Aqeel*[1,2], Stanley Nwokebuihe[3], Saleh Qaysi[4], Ahmed Abd El-Al[5,6], Adel Elkrry[7]

[1]Dept. of Geology, College of Science, Taibah University, P.O. Box 30002, Madinah, Zip Code: 41477
[2]Dept. of Earth and Environmental Sciences, Faculty of Science, Sana'a University, Yemen
[3]Faith Technologies Inc., Huntsville, AL, USA
[4]Geology and Geophysics Dept., King Saud University, Riyadh, Saudi Arabia
[5]Geology Dept. Al Azhar University (Assiut Branch), Assiut, Egypt
[6]Dept. of Civil Engineering, Najran University, Najran, Saudi Arabia
[7]Dept. of Geology and Applied Geophysics, University of Al-Jabel Al-Gharibi, Libya

Received 23rd March 2022; Accepted 26th September 2022

Abstract

2D and 3D Geotechnical models of the top 10-meter depth of the study area were created to reflect the investigated geotechnical spatial variation behavior of subsurface soil. The geotechnical investigation included advancing boreholes down to 10 m at 50 stations reflecting the resistance of soil (N-value) and collecting 250 soil samples at different depths to identify soil geotechnical properties. For foundation construction purposes, 15 random test pits were also excavated down to 3 m depth to mainly measure soil compaction parameters.

Soil particles of sand (61 – 99%) silt (0 – 26%), and gravel (0 – 23%), with no clay particles, were identified in the area; thus, the soils were classified into SP, SP-SM, and SM. These soils also have shown a wide range of water content (2.90 – 20.10%), N-value (13 – 85), relative density (medium to very dense), maximum dry density (2.0- 2.2 g/cm^3), and an internal friction angle of 25° to 28°.

The produced geotechnical models have made correlation and linking spatial variations of geotechnical properties with each other, and even within each property, an easy and significant task. Therefore, producing such geotechnical models was a powerful and useful technique to interpret and predict the geotechnical behavior of subsurface soil.

Keywords: *Geotechnical Investigation, Subsurface Soil, Spatial Variation, 2D geotechnical Models, 3D geotechnical Models, Najran*

1. Introduction

Earthen materials have commonly wide variations in their geological and geotechnical properties which can lead to severe geotechnical problems and hazards and even cause catastrophic events. Therefore, accurate assessment of the uncertainty of engineering behavior is an important phase of all civil engineering projects particularly for those projects which involve significant interactions with subsurface earthen materials (Parsons et al., 2002). In recent years, many human-made geohazards, such as ground subsidence, engineering slope instability and foundation settlements, have been witnessed with more regularity in growing urban areas due to the lack of adequate and accurate subsurface geological and geotechnical studies, resulting in threats to human lives and properties (Tang and Xu, 2009; Dong et al., 2015; Aqeel et al., 2019; Abd El Al et al., 2019, 2020).

In general, the in-situ geotechnical behavior of subsurface soils is complex and heavily dependent on the nexus of factors related to the complicated nature and exacerbated by human practices (Breysses et al., 2005; Massoud, 2016). Therefore, engineering geologists and civil engineers have been facing a challenge on how to clarify and accurately depict and visualize the underground surface conditions considering, at the same time, the horizontal and vertical distributions, and variations of geotechnical parameters.

Although producing traditional geological and geotechnical maps (2D models) has been intensely used to visualize ground conditions in fields of geoengineering, geology, and civil engineering (Kanu et al., 2013; Ayodele and Ajigo, 2020; Khallouf et al., 2020: Tobore et al., 2023), one of the biggest limitations is that these 2D models are restrictive in their ability to depict the subsurface across a range of depths and to chart the variations in geotechnical properties underground (Ding et al., 2015). In contrast, creating three-dimensional (3D) models with a thickness corresponding to different depths of interest can be integrated with various geotechnical, geological, hydrogeological, and geometrical parameters. As a result, representation, visualization, analysis, and interpretation of the underground conditions can be accurately conducted (Ford et al., 2008; Royse et al., 2009; Thierry et al., 2009; Dong et al., 2015).

Furthermore, the 3D geotechnical model is distinguished by including both a boundary model, which delineates the boundary between the different defined subsurface

* Corresponding author e-mail: ben_aqeel_2005@yahoo.com

geotechnical units, and a property model, which depicts the spatial distribution and variation of the geotechnical properties within those defined units (Hack et al., 2006).

Briefly, creating a 3D Model of the distribution of the geotechnical properties of the subsurface is increasingly becoming crucial in the decision-making process for commercial development and urban planning and management. It is not only a cost-effective method for characterizing the earths subsurface in geoengineering and civil engineering design practices but also it is an effective way to save effort and time in the analysis of data. Moreover, producing such subsurface geotechnical modeling is crucial for environmental risk assessment especially in rapidly growing cities (Mends and Lorandi, 2008; Kolat et al., 2006, 2012; Donghee et al., 2012; Abd El Aal and Rouaiguia, 2020).

All aforementioned studies pointed out the main objective of creating these 3D subsurface geotechnical models, which is usually to analyze and visualize the investigated geotechnical parameters of the area of interest concerning its vertical extension and thus to effectively assess its geotechnical performance.

Accordingly, most potential critical zones can be accurately depicted and identified. Hence, such information could result in the optimization of the proper design process of a construction as well as it could actively assist in reducing the construction risks.

In this research, geotechnical investigation and analysis, and producing of geotechnical spatial variations models (2D and 3D models) of the shallow subsurface soil of Khobash district, Najran Province, were conducted. Briefly, the main objectives of this research are to address the geotechnical properties of the study area concerning its vertical extension (depths), to correlate and link horizontal and vertical spatial variations of the investigated geotechnical properties with each other and even within each property, and thus to predict its geotechnical behavior as well as to predict any potential geotechnical problem that might affect any current and/or future construction and urban development in the area.

2. The study area

Najran Region is situated in the southwestern part of Saudi Arabia; bordered to the east by the Empty Quarter Desert, the Asir region to the west, both Riyadh and the Eastern Provinces to the north, and the Republic of Yemen to the south. Najran region, which has an area of about 149,511 km^2, is considered one of the fastest-growing southern regions in Saudi Arabia. Its population has increased nearly 2 times from 300,994 in 1992 to 595,705 in 2018 (Saudi General Authority for Statistics, 2018). The Geomorphology of Najran Province can be classified into three major geomorphological units: i) high-mountain areas in the west, ii) floodplain areas with alluvial deposits along Wadi Najran, and (iii) eastward dominating dunes along the Empty Quarter as shown in Fig. 1b.

The study area is located within the dunes unit to the east of Najran City occupying a major part of Khobash district. It lies between 17°31'16.00" and 17°31'47.926" North and 44°29'10.62" and 44°31'08.686"East (Fig. 1c). The study area has an area of about 1.5 km^2 with a length of about 2000 m and a width of approximately 750 m as shown in Fig. 1c.

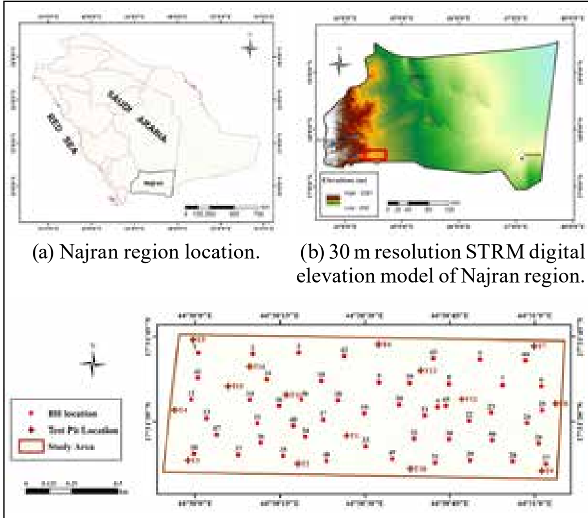

(a) Najran region location. (b) 30 m resolution STRM digital elevation model of Najran region.

(c) Study area boundary and soil sampling locations.

Figure 1. Study area location, geomorphology, geology (a and b), and soil sampling locations (c).

In terms of geology, the rocks in Najran Region belong to the Precambrian and consist of igneous rocks, as well as some stratified rocks of the Cambrian–Ordovician Wajeed sandstone, and occasional Tertiary bedrock (Shanti, 1993; Vincent, 2008; Stern and Johnson, 2010) as shown in Fig. 1b. Alluvial deposits along Wadi Najran as well as dunes are considered Quaternary deposits (Shanti, 1993).

3. Data and methodology

In this research, the geotechnical investigation involved the following three main stages: i) geotechnical field investigation; ii) geotechnical laboratory testing; and iii) Geotechnical data modeling and visualization

3.1 Geotechnical field investigation

3.1.1 Reconnaissance field visit

Based on a reconnaissance field visit, it was found that the ground surface of the study area is almost flat covered by dry sand particles and its southern boundary is adjacent to a strategic Najran-Sharourah highway linking Saudi Arabia and Yemen (Figs. 1 and 2). Therefore, preliminary geotechnical investigation for such an area is crucial for urban planning and commercial development plans.

3.1.2 Subsurface soil sampling

The study area has an area of about 1.5 km^2 estimated using ArcGIS technology. 50 random sampling locations were selected to cover this area to conduct a shallow borehole drilling process up to 10 m of depths investigating its geotechnical properties. These boreholes, denoted hereafter as BH (Fig. 1), were prepared according to the American Society for Testing and Materials ASTM D4428 standards (ASTM, 1995) and drilled using a rotary mobile borehole drilling machine (ACKER mobile rig) with a hole diameter of 50.8 mm as shown in Fig. 2.

Figure 2. General view of the study area condition showing the used drilling rig machine for the SPT test and soil sampling

At each BH, boring was advanced to the desired intervals of depths, which were 1, 3, 5, 8, and 10 m sequentially as illustrated in the created 3D model (Fig. 3). The point of selecting those intervals of depths is to reflect the geotechnical properties and, thus, the ground conditions of the investigated depths for further foundation and construction purposes at different levels of depth. Subsequently, disturbed soil samples were collected at each interval of depth at each borehole with a total of 250 BH soil samples.

To measure soil compaction parameters (maximum dry density and corresponding optimum moisture content of soil) and for foundation investigation purposes as well, open test pits with a width of about 1.2 m and a length of roughly 2 m were excavated to 3 m of depth using Backhoe Loader Machine at 15 different locations over the study area (Figs. 3 and 4, 5). 15 disturbed soil samples were collected from these test pits, denoted hereafter as TP soil samples.

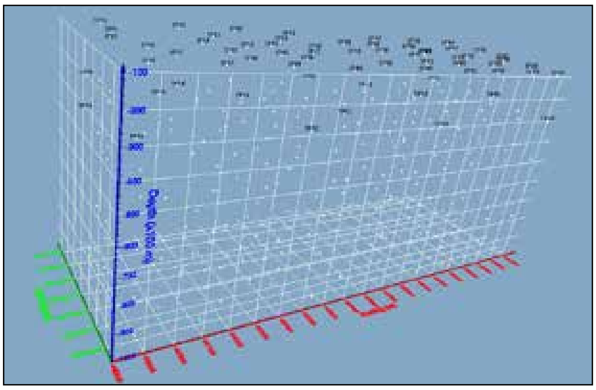

Figure 3. 3D- perspective view of the BH locations (ST locations) starting from the ground surface to 10 m depth with data points at 1, 3, 5, 8, and 10 m of depths using Voxler software. TPs represent the location of test pits. The vertical extension was exaggerated by one hundred times.

As a result, 265 soil samples were collected during the fieldwork (both 250 BH soil samples and 15 TP soil samples). All the collected samples were kept in plastic bags, and then transferred to the geotechnical lab of Al-Jazzar Consulting Engineers Company, Najran City, to measure their geotechnical index properties.

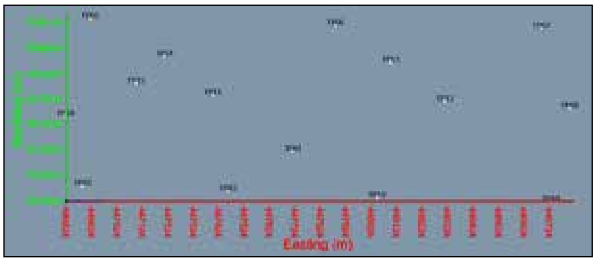

Figure 4. 2D map showing the spatial distribution of the 15 test pits (TP) across the study area

Figure 5. Excavation process of test pits in the study area

3.1.3 Standard penetration test (SPT)

Standard Penetration Test (SPT) is an important geotechnical method used to reflect the consistency and resistance of subsurface soils. During the BH drilling process, SPT was conducted according to ASTM D 1586. At each borehole (BH), the boring was, first, advanced to the desired depth level (1, 3, 5, 8, and 10 m) sequentially. Then, the split-spoon sampler attached to the drill rod was placed at the top of each testing point. The SPT-hammer, then, was dropped driving the sampler into the soil layer until reaching 15 cm of depth. This procedure was repeated two more times until 45 cm of total penetration was achieved. The total number of blows required to penetrate the last 30 cm depth is accounted as the "N-value", which is used to determine the relative density of coarse soils (D_r) and/or the strength of stiff cohesive soils based on the type of soil encountered (Table 1). All the results of the SPT (N-Value) are listed in Table 2.

Table 1. N-Value of SPT and its corresponding relative density of coarse soils (Modified after Rogers, 2006)

N-Value	D%	Description	Symbol
Less than 4	Less than 15	Very loose	VL
4 – 10	15 – 60	Loose	L
11 – 30	61 – 75	Medium	MD
31 – 50	76 – 90	Dense	D
0ver 50	Over 90	Very Dense	VD

Table 2. Geotechnical Lab results of BH soil samples at depths 1, 3, 5, 8, and 10 m

St. No.	1 m of Depth				3 m of Depth				5 m of Depth				8 m of Depth				10 m of Depth			
	Soil Type	SPT Results		w%	Soil Type	SPT Results		w%	Soil Type	SPT Results		w%	Soil Type	SPT Results		w%	Soil type	SPT Results		w%
		N	D_r			N	D_r			N	D_r			N	D_r			N	D_r	
1	SP	15	MD	5.6	SP	43	D	7.1	SP	54	VD	2.9	SP	55	VD	12.3	SP-SM	70	VD	9.1
2	SP	26	MD	12.3	SP-SM	26	MD	11.1	SP-SM	30	MD	13.5	SP	52	VD	15.6	SP-SM	54	VD	15.5
3	SP-SM	22	MD	11.9	SP-SM	36	D	13.6	SP-SM	59	VD	16.3	SP-SM	57	VD	14.2	SP	59	VD	18.5
4	SP	16	MD	14.3	SP	45	MD	9.3	SP-SM	57	VD	12.6	SP-SM	76	VD	10.5	SP-SM	75	VD	14.1
5	SP-SM	23	MD	15.2	SP-SM	43	D	18.2	SP-SM	50	D	18.2	SM	50	D	12.5	SM	68	VD	12.7
6	SP-SM	32	D	18.3	SP-SM	45	D	15.9	SM	58	VD	17.3	SP	53	VD	12.1	SP-SM	62	VD	16.4
7	SM	30	MD	12.1	SM	24	MD	12.9	SP	27	MD	11.5	SM	53	VD	11.9	SP	62	VD	11.8
8	SP	18	MD	11.8	SP	27	MD	8.9	SP-SM	55	VD	11.2	SM	60	VD	9.6	SP	54	VD	11.5
9	SP-SM	22	MD	14.9	SP-SM	29	MD	8.8	SP-SM	43	D	15.6	SP	51	VD	18.3	SP-SM	65	VD	17.4
10	SP	44	D	10.9	SP-SM	34	D	13.5	SP-SM	50	D	13.5	SP	63	VD	10.9	SP-SM	63	VD	9.8
11	SP-SM	17	MD	12.5	SP-SM	26	MD	14.2	SP	47	D	12.7	SP-SM	70	VD	12.7	SM	80	VD	16.9
12	SP	23	MD	8.7	SP-SM	19	MD	9.8	SM	55	VD	11.5	SM	52	VD	10.1	SP-SM	56	VD	6.7
13	SP	30	MD	11.5	SP	35	D	13.8	SP	60	VD	14.6	SM	74	VD	15.6	SP	72	VD	17.9
14	SP	24	MD	6.4	SP	22	MD	9.1	SP	25	MD	14.4	SM	37	D	6.8	SP	44	D	7.9
15	SP	27	MD	16.4	SP	24	MD	15.5	SP-SM	42	D	14.2	SM	61	VD	16	SP-SM	78	VD	20.1
16	SM	31	D	12.9	SM	28	D	15.5	SM	49	D	11.6	SM	50	D	5.9	SP-SM	76	VD	4.71
17	SP-SM	20	MD	13.8	SP-SM	13	MD	11.2	SM	33	D	11.3	SM	44	D	11.9	SM	48	D	13.4
18	SP	22	MD	11.5	SP	26	MD	14.4	SP-SM	50	D	13.1	SP	80	VD	7.7	SM	82	VD	14.1
19	SP	24	MD	9.5	SP	24	MD	8.6	SP-SM	25	MD	6.9	SP-SM	45	D	5.4	SP-SM	48	D	9.2
20	SP	23	MD	11.3	SP	25	MD	9.1	SM	47	D	8.7	SP-SM	42	D	11.1	SP-SM	40	D	12
21	SP	20	MD	12.9	SP	29	MD	14.3	SP	41	D	14.4	SP-SM	50	D	14.4	SP-SM	60	VD	12.9
22	SP	26	MD	5	SP	28	MD	11.4	SP-SM	35	D	8.9	SP	41	D	9.4	SM	40	D	11.2
23	SP-SM	31	D	13	SP-SM	32	D	11.1	SP-SM	41	D	11.9	SM	45	D	15.5	SP-SM	56	VD	17.2
24	SP-SM	20	MD	7.8	SP-SM	28	MD	15.4	SP-SM	48	D	6.6	SM	51	VD	12.9	SP-SM	44	D	12.9
25	SM	26	MD	15.9	SM	27	MD	17.6	SP-SM	50	D	10.5	SM	67	VD	16.9	SP-SM	75	VD	12.11

Table 2. (continued) Geotechnical Lab results of BH soil samples at depths 1, 3, 5, 8, and 10 m

St. No.	1 m of Depth				3 m of Depth				5 m of Depth				8 m of Depth				10 m of Depth			
	Soil Type	SPT Results		w%	Soil Type	SPT Results		w%	Soil Type	SPT Results		w%	Soil Type	SPT Results		w%	Soil type	SPT Results		w%
		N	D_r			N	D_r			N	D_r			N	D_r			N	D_r	
26	SP-SM	21	MD	11.7	SP-SM	30	MD	12.1	SP-SM	34	D	10.1	SP-SM	46	D	11.9	SP-SM	68	VD	14.7
27	SP-SM	24	MD	11.9	SP-SM	27	MD	13.1	SP	40	D	13.4	SM	34	D	12.7	SP-SM	61	VD	11.6
28	SP	23	MD	11.7	SP-SM	30	MD	16.1	SM	44	D	16.1	SP-SM	69	VD	16.3	SP-SM	57	VD	17.9
29	SP-SM	28	MD	12.1	SP-SM	26	MD	9.8	SP-SM	50	D	13.1	SM	51	VD	16.4	SP-SM	80	VD	12.3
30	SP	26	MD	6.8	SP	25	MD	9.9	SP-SM	31	D	4.3	SP-SM	36	D	12.7	SM	40	D	11.5
31	SP	23	MD	14.2	SP	27	MD	16.8	SP	48	D	14.1	SP-SM	50	D	17	SP-SM	61	VD	15.7
32	SP-SM	21	MD	9.9	SP-SM	25	MD	10.2	SP-SM	44	D	7.3	SM	47	D	14.4	SP-SM	47	D	13.4
33	SM	22	MD	15.6	SM	21	MD	9.3	SP-SM	26	MD	6.6	SM	44	D	13.9	SP	42	D	13.9
34	SP	21	MD	18.2	SP-SM	36	D	15.9	SP-SM	72	VD	15.2	SP-SM	75	VD	13.7	SP-SM	85	VD	13.6
35	SM	18	MD	7.4	SM	31	D	9.6	SP-SM	41	D	7.7	SM	43	D	12.1	SP-SM	41	D	12.1
36	SP	21	MD	13.1	SP	31	D	11.7	SM	50	D	10.2	SP-SM	43	D	11.3	SM	44	D	8.7
37	SP	31	D	13.1	SP	46	D	14.4	SM	58	VD	15.7	SP-SM	62	VD	18.2	SP-SM	65	VD	20.1
38	SP	19	MD	10.5	SP	29	MD	12.8	SM	33	D	12.7	SP-SM	31	D	16.9	SM	45	D	16.4
39	SP-SM	18	MD	13.2	SP-SM	30	MD	16.4	SP-SM	50	D	14.8	SP-SM	60	VD	16.3	SM	67	VD	16.4
40	SP	35	D	10.9	SP	46	D	9.8	SP	68	VD	13.2	SP-SM	71	VD	12.8	SP-SM	73	VD	12.8
41	SP	28	MD	7	SP	30	MD	8	SP	33	D	11.2	SP	63	VD	13.5	SP-SM	69	VD	13.3
42	SP	23	MD	9.8	SP	23	MD	10.1	SP	30	MD	11.3	SP	56	VD	12.6	SP-SM	80	VD	12.3
43	SP-SM	22	MD	12	SP-SM	30	MD	12.9	SP-SM	50	D	13.1	SP-SM	71	VD	13.5	SP-SM	62	VD	13.1
44	SP-SM	23	MD	6.4	SP-SM	23	MD	7.1	SP-SM	39	D	7.9	SP-SM	41	D	9.1	SP-SM	48	D	8.9
45	SP-SM	23	MD	10.5	SP-SM	33	D	12.1	SP-SM	67	VD	13.3	SM	53	VD	12.4	SM	58	VD	11.4
46	SP	20	MD	11.2	SP	24	MD	11.7	SP	25	MD	12.1	SP	50	D	12.6	SP-SM	63	VD	12.1
47	SP	19	MD	14.9	SP	26	MD	15.1	SP	50	D	12.3	SP	68	VD	9.7	SP-SM	81	VD	9.7
48	SP	25	MD	14.4	SP	26	MD	13.3	SP	32	D	11.9	SP-SM	35	D	15.2	SP-SM	31	D	12.2
49	SP	20	MD	15.9	SP	30	MD	14.8	SP	50	D	8.1	SM	56	VD	8.9	SM	61	VD	10.2
50	SM	21	MD	12.4	SM	25	MD	4.9	SM	25	MD	5.4	SP-SM	36	D	7.7	SP-SM	52	VD	8.5
Min		15	MD	5		13	MD	4.9		25	MD	2.9		31	D	5.4		31	D	4.71
Max		44	D	18.3		46	D	18.2		72	VD	18.2		80	VD	18.3		85	VD	20.1
Ave				11.82				12.16				11.7				12.6				12.98

3.1.4 Groundwater investigation

During the drilling of the shallow boreholes process as well as the excavation of the test pits, groundwater was not encountered in the study area.

3.2 Geotechnical lab testing

All the geotechnical tests of the collected subsurface soil samples were performed according to the American Society for Testing and Materials (ASTM, 1995). As aforementioned, two types of disturbed subsurface soil samples were collected in this research: 250 BH soil samples and 15 TP soil samples (in a total of 265 soil samples).

3.2.1 Laboratory testing of BH soil samples

250 subsurface soil samples were collected from all 50 BH locations at five different successive depth levels (1, 3, 5, 8, and 10 m). All those collected samples were subjected to the following lab tests:

- Natural water content test according to ASTM D 2216.
- Soil grain size analysis according to the ASTM D422.
- Soil classification using the Unified Soil Classification System (USCS) and according to ASTM D2487. For those coarse soils containing significant portions of fine particles, fine soil particles were identified according to both ASTM D4318 (Atterberg Limits test). The Atterberg limits test is commonly used as an integral part of several engineering classification systems such as USCS to characterize fine-grained fractions of soils.
- Modified Proctor Compaction test according to ASTM D 1557.

Although the SPT was conducted for all the soils at the intervals of desired depths, a direct shear box test was also conducted according to ASTM D3080 for those soil samples collected at a depth of 3 m but at only twelve selected borehole locations as shown in Fig. 6. The purpose of conducting this test was to measure the strength of the soil of the investigated area and thus to create more accurate and reliable measurements about the subsurface conditions of the area. All the geotechnical lab results of the BH soil samples are listed in Tables 2 and 3.

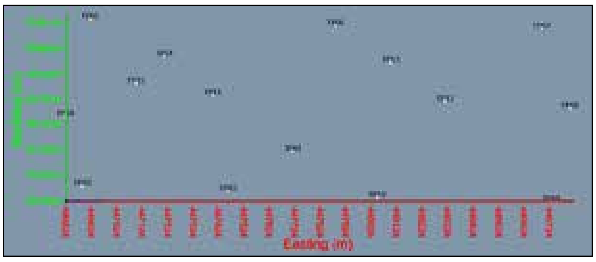

Figure 6. 2D map showing the location of the 12 BH stations selected to measure the shear strength of soils

3.2.2 TP soil samples

All the 15 collected TP soil samples were subjected to the following lab tests:

- Soil grain size analysis according to the ASTM D422
- Soil classification using the Unified Soil Classification System (USCS) and according to ASTM D2487 and ASTM D4318.
- Modified Proctor Compaction test according to ASTM D 1557.

Soil types and maximum dry density (ρ_{dry}) and the corresponding optimum moisture content (OMC) were determined for all the 15 TP soil samples as listed in Table 3.

Table 3. Soil types and their compaction parameter values at the excavated test pits at 3 m depth in the study area

St. No.	Soil Type	ρ_{dry} (g/cm^3)	OMC %
TP1	SP	2.15	7.20
TP2	SP	2.15	7.00
TP3	SP-SM	2.12	7.30
TP4	SP	2.14	7.50
TP5	SP	2.09	8.60
TP6	SP	2.01	8.70
TP7	SP	2.19	8.20
TP8	SP	2.14	7.70
TP9	SP	2.16	7.60
TP10	SP	2.17	7.50
TP11	SP	2.15	7.70
TP12	SP-SM	2.01	9.70
TP13	SP	2.12	7.40
TP14	SP	2.10	7.10
TP15	SP	2.18	8.20
Min.		2.01	7.00
Max.		2.19	9.70
Ave		2.13	7.83

3.3 Geotechnical data modeling and visualization

Three-dimensional models of the obtained results of natural water content, soil types, SPT results (N-Value), relative density (D_r), maximum dry density (ρ_{dry}), optimum moisture content (OMC), and shear strength were created using the Voxler v.3 software package (http://www.goldensoftware.com/products/Voxler).

In general, the first step in the 3D modeling process is data preparation. In this research, each set of geotechnical data was arranged in a format compatible with input to the software – including the 3D coordinates and corresponding geotechnical properties of each data point. Next, the Gridding function was used to convert the input data into a lattice node interpolated file based on the defined gridding parameters. Finally, the VolRender function was used to generate the 3D models by choosing the appropriate color scales that best highlight the spatial variation in geotechnical properties across the study area. Similarly, the Oblique-Image tool was used to generate 2D models of the study area, where applicable - which were 2D slices of the created 3D models at the desired various levels of depths (1, 3, 5, 8, and 10 m consecutively) as will be illustrated later in the next sections.

4. Results and discussion

4.1 Soil Grain Size Analysis and Soil Types

Based on the grain size analysis results of the 265 collected subsurface soils, only three main types of soil grain size were identified in the investigated area: sand (61 – 99%), silt (0 – 26%), and gravel (0 – 23%) with an average of 87.24%, 7.81%, and 4.70%, respectively. The absence of clay particles was a strong indicator of the low plasticity, or even non-plasticity, character that those soils may have. These results reflected a significant range of variation in soil particle sizes which certainly affects the soil engineering behavior vertically and horizontally across the study area.

In terms of soil classification, it is found that only sandy soil covers the whole investigated area. Precisely, three different soil types have been identified: poorly graded sand (SP), poorly graded sand with silt (SP-SM), and silty sand (SM) as listed in Tables 2 and 3. As noticed, this soil is poorly graded (well sorted) which is generally characterized by higher porosity compared to well-graded sand soil.

The other observation is that SP soil occupies the major portion of the first three-meter depths of investigation with a percent of occurrence ranging between 46% and 86.67% and, then, this occurrence decreases gradually with increasing depth of investigation (Table 4). This spatial variation was portrayed through the created geotechnical models (Fig. 7). These created 2D and 3D geotechnical models showed that SP soil particles are concentrated mainly in the western and the middle parts of the study area.

Table 4. Frequency and percent of identified soil types of the investigated depths of the study area.

			Investigated Depth level									
	No. of Samples	Soil Type	1 m		3 m		5 m		8 m		10 m	
			Freq.	%	Freq.	%	Freq.	%	Freq.	%	Freq.	%
BH samples	250	SP	28	*56*	23	*46*	15	30	11	22	6	12
		SP-SM	16	32	21	42	25	*50*	20	*40*	33	*66*
		SM	6	12	6	12	10	20	19	*38*	11	22
TP samples	15	SP	-		13	86.67	-					
		SP-SM			2	13.33						
		SM			0	0						
BH + TP samples at 3 m of depth	65	SP	-		36	55.38	-					
		SP-SM			23	35.38						
		SM			6	9.24						

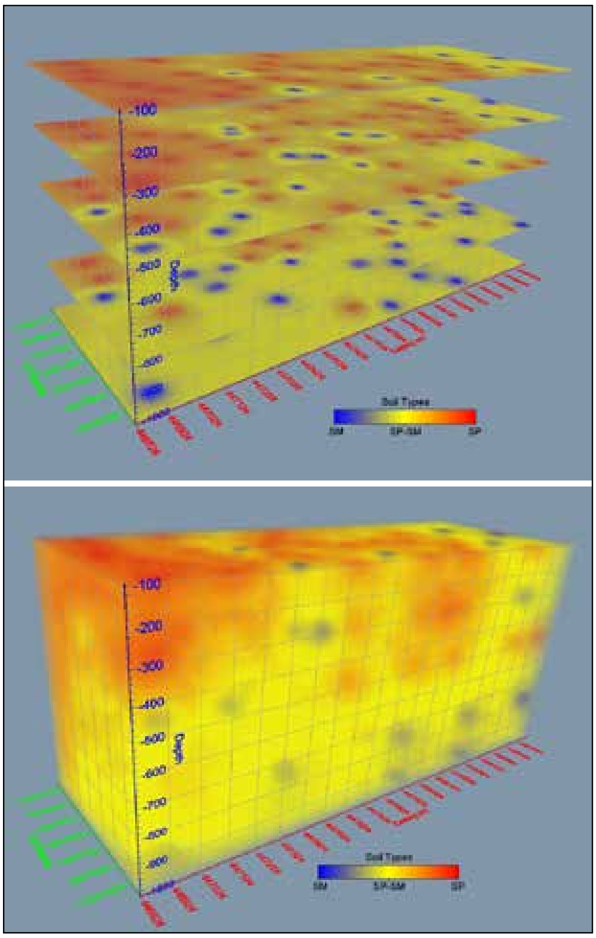

Figure 7. 2D slices (above) and 3D model (below) of the spatial distribution of soil types in the investigated area.

Moreover, it can be noted that SP-SM and SM soil types occur a little more at the depth of 3 m compared to the first investigated meter of depths (Table 4; Fig.7). This occurrence of silty sand was more significantly observed at the depths below 3 m where SP-SM soil occupies the major parts covering 40% and up to 66% of those investigated depth (Table 4, Fig.7).

Furthermore, as shown in Fig. 7, the 2D geotechnical models of soil types depicted the horizontal spatial distributions of the SM soil where a significant occurrence of it (38%) can be shown at the depth of 8 m (Table 4).

According to the created geotechnical models (Fig. 7) as well as the results listed in Table 4, it can, briefly, be concluded that the SP soil is the dominant soil type that occurs within the first three meters of depth. Then, SP-SM soil type is the one that significantly occurred within the rest of the investigated depth (below 3 m) but with the presence of a considerable amount of SM soil (38%) particularly at the depth of 8 m of investigation (Fig.7, Table 4).

4.3 Natural water content

Because natural water content (w) has a profound effect on soil engineering behavior, all the 250 BH soil samples were examined to determine their natural water content.

The current geotechnical investigation showed that the water content values of the soils in the study area were between 2.9 and 20.1% with an average of 12.26% and a range of 17.2%. In general, such a wide range in water content values of the soils should be taken into consideration for any urban planning and construction that may take place in the area.

Based on the results listed in Table 2, the range of water content (w) values was almost constant for those samples collected at depths 1m (w = 5% – 18.3%), 3m (w = 4.9% – 18.2%), and 8 m (w = 5.4% – 18.3%) with a range value of about 13%. The highest range of water content recorded in the area was at a depth of 5 m (w = 2.9% to 18.2% with a range of 15.3%) and a depth of 10 m (w = 4.71% to 20.10% with a range of 15.39%). The significant vertical variation of water content values especially at depths below 3 m can be referred to the presence of a considerable portion of silt particles where SP-SM and then SM soil types are the dominant types below 3 m of depth (Tables 2 and 4; Figs. 8 and 7). Based on the created geotechnical models (Fig. 8), the most common range of water content measured within the investigated depths was between 9% and 16% with a range of 7.

4.4 Standard penetration test (N-value and relative density of soil)

SPT results (N-value) are mainly used to estimate consistency, strength, and, in some cases, soil compressibility. In general, the SPT results (N-value) of the investigated area ranged between 13 and 85 representing a range of soil relative density (D_r) of medium to very dense soils as listed in Tables 1 and 2.

N-value was correlated to relative density and then summarized as listed in Table 5. According to the measured relative density, three types of soils have been identified in the study area: medium-dense soil (MD-soil), dense soil (D-soil), and very dense soil (VD-soil). It is found that, within the first three meters of depths, all the soils showed a relative density level of medium (MD) to dense (D). In other words, SPT results revealed that there was no very dense soil (VD) encountered within the first three meters of depths of investigation. In contrast, very dense soil was encountered below 3 m of depths, particularly at depths of 8 m and 10 m where no medium-dense soil was encountered at all (Table 5; Fig. 9).

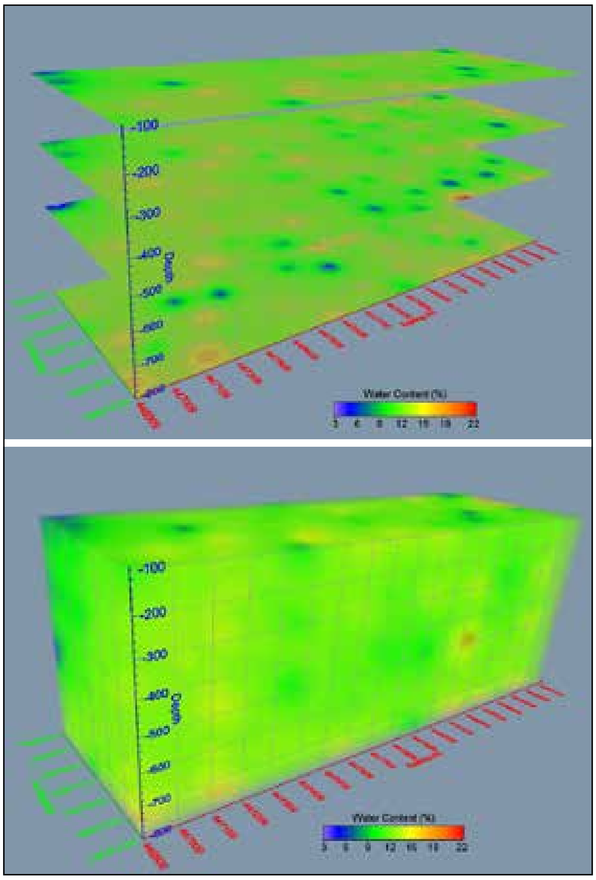

Figure 8. 3D Model (above) and 2D slices (below) of the spatial distribution of water content in the investigated area

Table 5. Estimated frequency and percent of each relative density type (Dr) of the 250 BH soil samples.

	D_r Type	Investigated Depth									
		1 m deep		3 m deep		5 m deep		8 m deep		10 m deep	
		Freq.	%	Freq.	%	Freq.	%	Freq.	%	Freq.	%
D_r	MD	44	*88*	36	*72*	8	16	-	-	-	-
	D	6	12	14	28	31	*62*	22	44	14	28
	VD	-	-	-	-	11	22	28	*56*	36	*72*
D_r Zone	MD- Soil Level			D- Soil Level				VD- Soil Level			

As the depth of investigation increases, the density of soils increases which can be due to the overburden of the above layers of soils as well as because of increasing fine soil (silt) particles in those soils occurring below 3 m of depth (Figs. 7 and 9).

In general, (N-value), the vertical extension of the study area can be divided into three main zones based on the measured relative densities as follows (Table 5, Fig. 9):

i- MD-Soil Zone: This zone of density was observed within the first three meters of the investigated depths where N- N-values were between 13 and 46 while the corresponding relative density was medium dense to dense soil (MD – D). Within the depth of 1 m, it can be observed that 44 (88%) out of 50 soil samples have medium-dense relative density (MD). Additionally, 36 soil samples (72%) were characterized as MD as well at the depth of 3 m (Table 5, Fig 9). Therefore, the majority of soils that occur within the first three meters of investigated depths are medium dense where the SP soil is the dominant soil type (Table 4; Figs. 7 and 9).

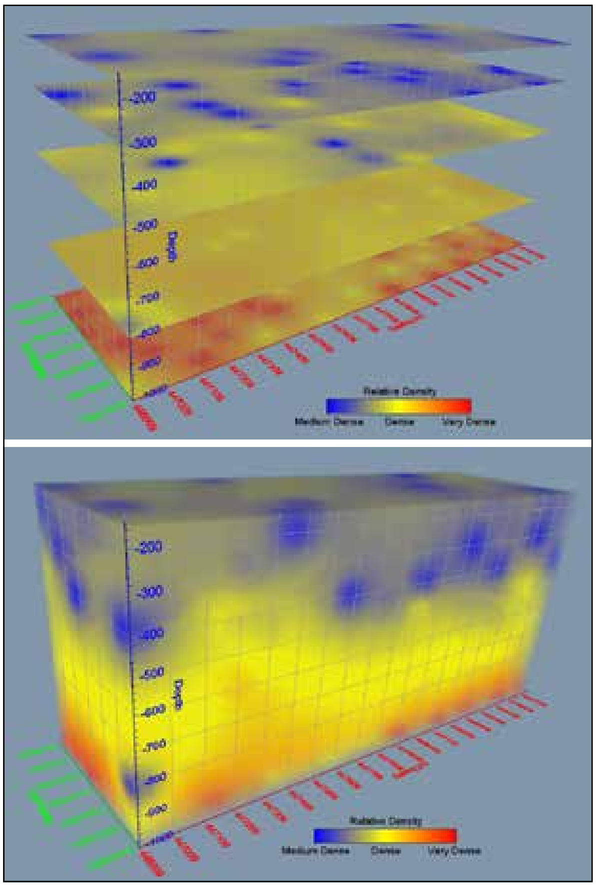

Figure 9. 2D Model (above) and 3D slices (below) of the spatial distribution of relative density (Dr) in the investigated area.

ii- D-Soil Zone: This zone of density was observed at only 5 m of depth where the soils had a range of N-value of 25 to 72 with a relative density ranging from medium (MD) to very dense (VD). Although, 8 soil samples were identified as medium dense (MD) and 11 samples measured as very dense (VD), the majority of soil samples (31 samples) with a percent of 62% were measured as dense soil (D) at only this level of depth (Fig. 8, Table 5). The other remarkable observation is that this zone is the only zone that has the widest range of relative density (medium dense to very dense soil) where all the three identified soil types (SP, SP-SM, and SM) have significantly occurred within this level of depths (Table 4; Figs. 7, 9)

iii- VD-Soil Zone: This zone of density was encountered in the last two levels of depths of investigation (8m and 10m depths) where the observed N-values of soils fell between 31 and 85 with a relative density of dense (D) to very dense (VD). However, very dense soils represent 56% and 72% of the soils at 8 m and 10 m of depth, respectively. Accordingly, this zone is characterized by its high relative density (very dense soil) (Table 5, Fig.9). It should be noted that there is no medium-dense soil was detected at this level of depth (Table 5).

As aforementioned SP-SM soil and then SM soil were the most encountered soil types below the depth of 3m, and thus the increasing density within the other investigated levels of depths (5, 8, and 10 m) can be related to the increasing of fine particles (silt grain fraction) at those depths (Table 4; Fig. 7).

4.5 Shear strength of soil

As aforementioned 12 subsurface soil samples were collected from different 12 BH locations at only a depth of 3m to measure soil shear strength utilizing direct shear test (Fig. 6).

The results indicated that the shear strength of the soils mainly resulted from their internal friction angle (ϕ) since their cohesion values are all less than 1 kg/cm^2. All the examined soil samples have very low cohesion strength values not exceeding 0.24 kg/cm^2 (Table 6, Fig. 10). Friction angle (ϕ) values of these soils ranged between 23° and 32° with an average of 26.5°.

According to the created horizontal spatial variation map (2D model) of the measured internal friction angles as depicted in Fig. 11, it can be noticed that most parts of the soil had a friction angle that varies between 25° and 28° where SP soil is the dominant type of soils occupying the major part of the investigated study area but at the depth of 3 m as illustrated in Fig. 7 as well.

Table 6. Soil shear strength measurements conducted for soils at 3 m of depth.

BH No. (St. No.)	Soil type	Friction angle (ϕ in degrees)	Cohesion (kg/cm^2)	BH No. (St. No.)	Soil type	Friction angle (ϕ in degrees)	Cohesion (c, kg/cm^2)
1	SP	29	0.06	**28**	SP-SM	24	0.14
6	SP-SM	23	0.15	**36**	SP	28	0.17
8	SP	26	0.09	**41**	SP	28	0.20
9	SP-SM	26	0.23	**44**	SP-SM	26	0.21
10	SP-SM	25	0.18	**47**	SP	24	0.24
22	SP	27	0.14	**50**	SM	32	0.05

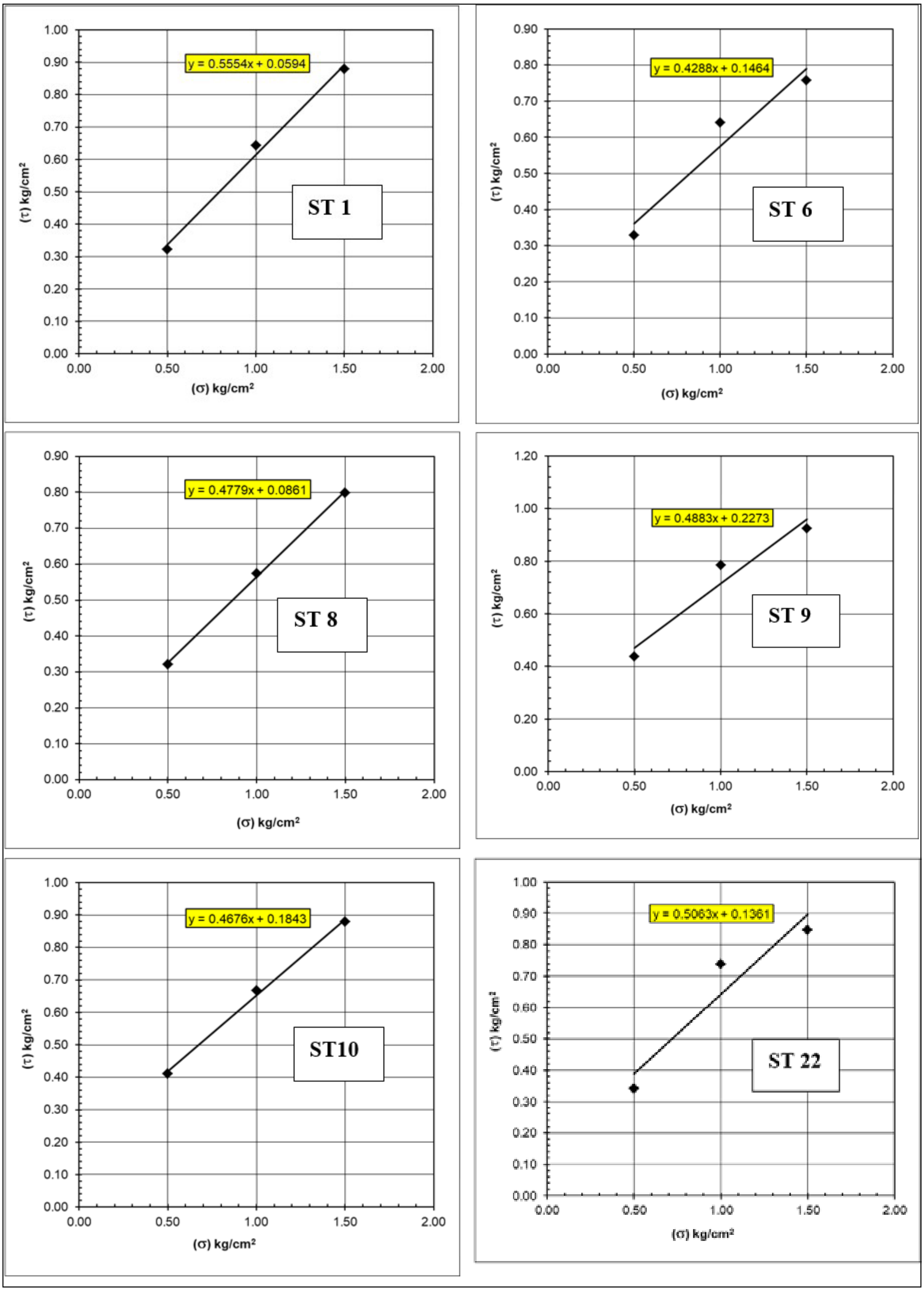

Figure 10. Shear strength curves of the 12 BH soil samples collected at 3 m depth.

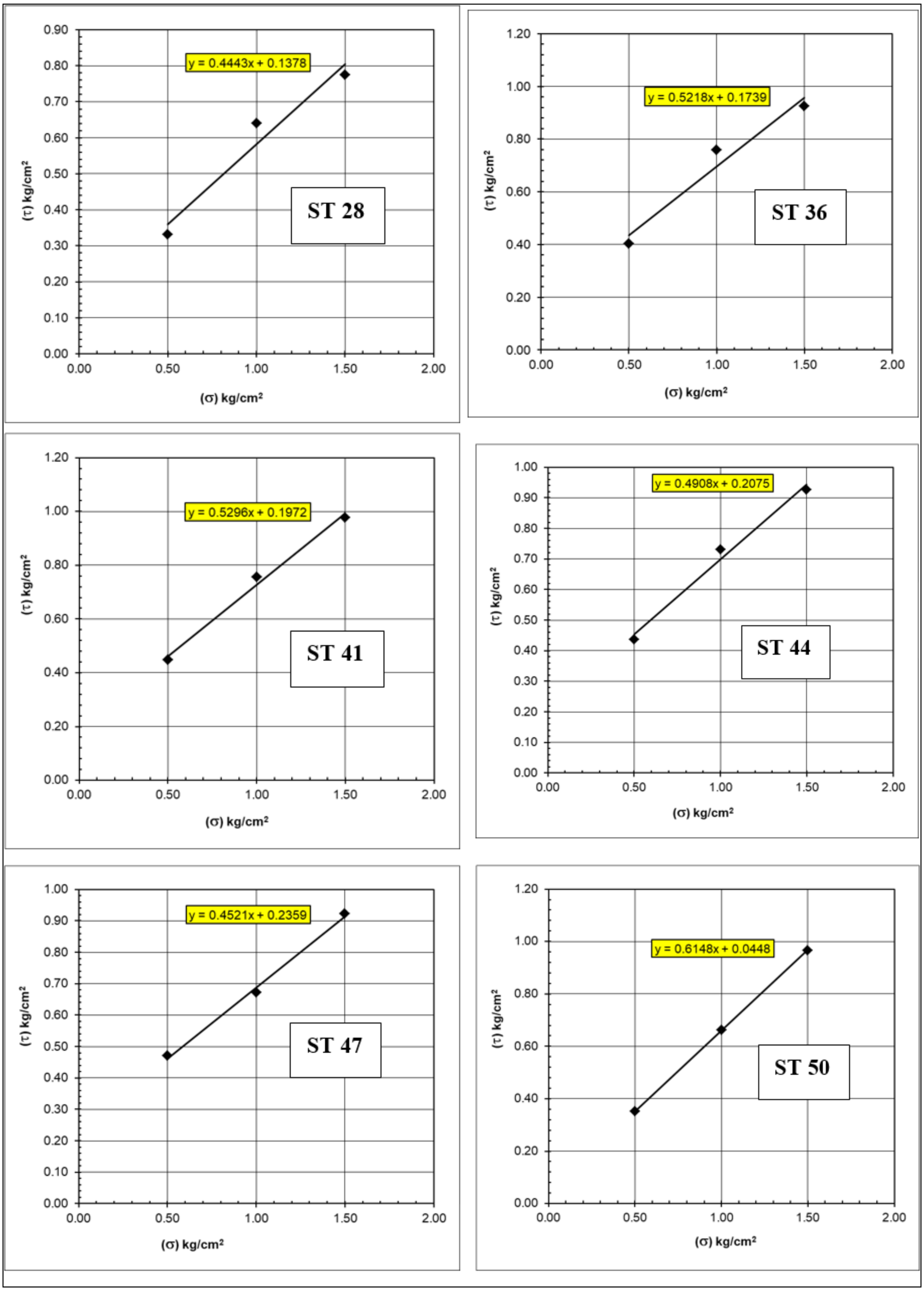

Figure 10. (continued) Shear strength curves of the 12 BH soil samples collected at 3 m depth.

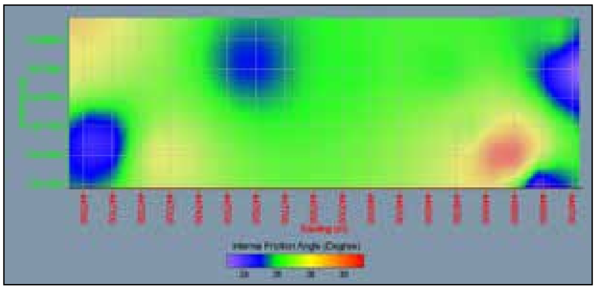

Figure 11. 2D slice of horizontal distribution of strength of soil (internal friction angle) at the 3 m depth of the investigated area.

4.6 Soil compaction parameters (Maximum dry density and OMC)

The results of the modified proctor compaction test, which was conducted on the collected 15 TP soil samples, showed that the maximum dry density (ρ_{dry}) ranged between 2.01 and 2.19 g/cm^3 with an average of 2.12 g/cm^3 while their corresponding range of optimum moisture content (OMC) was 7.0 - 9.7% with an average of 7.83% (Table 3).

As shown in Fig. 12, the produced 2D geotechnical models of soil compaction parameters, it can be concluded that the best range of OMC to obtain the possible highest range of maximum dry density (2.10 to 2.20 g/cm^3) is 7.0 to 8.0 % of moisture content. Furthermore, when checking the horizontal distribution of soil types at this depth as shown in Fig.7, it can be concluded that SP soil and then SP-SM soil are those soils on which maximum dry density can be achieved (Figs 7 and 12).

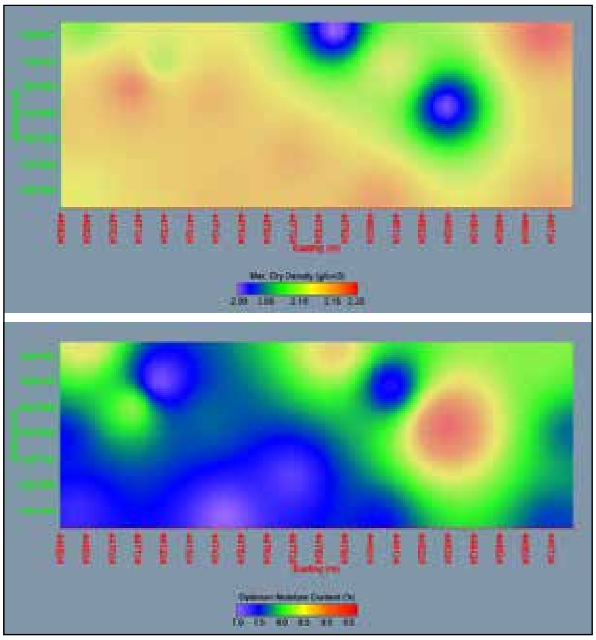

Figure 12. 2D spatial distributions of maximum dry density (above) and corresponding OMC percents (below) at the depth of 3 m of the investigated area.

5. Conclusions

According to the grain size analysis results of the 265 collected subsurface soils at different depths (1, 3, 5, 8, and 10 m), only sand, silt, and gravel particles have been identified with the absence of clay particles. As a result, the soils were classified into: SP, SP-SM, and SM soils.

Based on the created geotechnical models, SP soil was the dominant soil type that occurs within the first three meters of depth where most soils are medium dense (MD zone). It was also found that within this depth of investigation, most soils have friction angles that vary between 25° and 28°; and SP soil and SP-SM soils are those types of soils on which maximum dry density can be achieved but within a range of OMC of 7.0 – 9.7%.

At depths below 3 m, SP-SM soil type has significantly occurred but with a considerable amount of SM soil particularly at 8 m of depth. Furthermore, it was observed most soil samples at 5 m of depth have dense density (D zone) while the majority of soil samples below 5 m of depth reflected very dense density (VD zone). Moreover, the produced geotechnical models depicted significant vertical variation of water content at depths below 3 m where SP-SM and, then, SM soil types are the dominant types.

In sum, the created 2D and 3D geotechnical models were effective and valuable in the visualization of spatial variations in the geological properties of the subsurface soil of the study area. Using such models has made correlating and interpreting geotechnical properties with each other, and even within each property itself, an easy and effective task to track spatial variations in any direction; therefore, the geotechnical behavior of subsurface soil can be predicated in a time manner geoengineering purposes.

Acknowledgment

The authors would like to acknowledge Al-Jazzar Consulting Engineers Company for their technical support and providing some raw geotechnical data. In addition, the authors would also like to thank those unknown reviewers of the JJEES for their valuable remarks.

References

Abd El Aal AK, Kamel M, Al-Homidy A (2019) Using Remote Sensing and GIS Techniques in Monitoring and Mitigation of Geohazards in Najran Region, Saudi Arabia. Geotech Geol Eng 37: 3673–3700. https://doi.org/10.1007/s10706-019-00861-w.

Abd El Aal AK, Rouaiguia A (2020) Determination of the Geotechnical Parameters of Soils Behavior for Safe Future Urban Development, Najran Area, Saudi Arabia: Implications for Settlements Mitigation. Geotech Geol Eng 38:695-712. https://doi.org/10.1007/s10706-019-01058-x.

Abd El Aal AK, Nabawy BS, Aqeel A, Abidi A (2020) Geohazards assessment of the karstified limestone cliffs for safe urban constructions, Sohag, West Nile Valley, Egypt. Journal of African Earth Sciences 161. https://doi.org/10.1016/j.jafrearsci.2019.103671.

Aqeel A, Zaman H, Abd El Aal A (2019) Slope Stability Analysis of a Rock Cut in a Residential Area, Madinah, Saudi Arabia: A Case Study. Geotech Geol Eng 37:1765–1778. https://doi.org/10.1007/s10706-018-0720-7.

Ayodele O S, Ajigo I O (2020) Geological Mapping and Gemstones prospecting in Deformed Precambrian Rocks, East of Okemesi Fold Belt, Southwestern Nigeria. The Jordan Journal of Earth and Environmental Sciences (JJEES) 11 (4): 290-301

Aghamolaie I, Lashkaripour GR, Ghafoori M, Moghaddas NH (2019) 3D geotechnical modeling of subsurface soils in Kerman city, southeast Iran. Bull. Eng Geol Environ 78: 1385. https://doi.org/10.1007/s10064-018-1240-7.

Bell FG (2007) Engineering Geology, 2nd ed. Elsevier, Oxford.

Breysse D, Niandou H, Elachachi SM, Houy L (2005) A generic approach to soil structure interaction considering the effects of soil heterogeneity. Géotechnique 55(2):143–150. https://doi.org/10.1680/geot.2005.55.2.143.

Dong M, Neukum C, Hu H, Azzam R (2015) Real 3D geotechnical modeling in engineering geology: a case study from the inner city of Aachen, Germany. Bull Eng Geol Environ 74(2):281-300. https://doi.org/10.1007/s10064-014-0640-6.

Donghee K, Kyu-Sun K, Seongkwon K, et al (2012) Assessment of geotechnical variability of Songdo silty clay. Eng Geol 133–134:1–8. https://doi.org/10.1016/j.enggeo.2012.02.009.

Ford J, Burke H, Royse K, Mathers S (2008) The 3D geology of London and the Thames Gateway: a modern approach to geological surveying and its relevance in the urban environment, In the 2nd European Conference of International Association for Engineering Geology, Madrid, Spain, 15–20 Sept 2008.

Hack R, Orlic B, Ozmutlu S, Zhu S, Rengers N (2006) Three and more dimensional modelling in geoengineering. Bull Eng Geol Environ 65:143-153. https://doi.org/10.1007/s10064-005-0021-2.

Kanu M O,Meludu O C,Oniku S A (2013) A Preliminary Assessment of Soil Pollution in Some Parts of Jalingo Metropolis, Nigeria Using Magnetic Susceptibility Method. The Jordan Journal of Earth and Environmental Sciences (JJEES) 5 (2): 53-61

Khallouf A, AlHinawi S, AlMesber W et al (2020) Digital Mapping of Soil Properties in the Western-Facing Slope of Jabal Al-Arab at Suwaydaa Governorate, Syria. The Jordan Journal of Earth and Environmental Sciences (JJEES) 11 (3): 193-201

Kolat Ç, Doyuran V, Ayday C, LütfiSüzen M (2006) Preparation of a geotechnical microzonation model using geographical information systems based on multicriteria decision analysis. Eng Geol 87(3–4):241–255. https://doi.org/10.1016/j.enggeo.2006.07.005.

Kolat Ç, Ulusay R, LütfiSüzen M (2012) Development of geotechnical micro zonation model for Yenisehir (Bursa, Turkey) located at a seismically active region. Eng Geol 127:36–53. https://doi.org/10.1016/j.enggeo.2011.12.014.

Massoud A (2016) Geotechnical site suitability mapping for urban land management in Tanta District, Egypt. Arab J Geosci 9:340. https://doi.org/10.1007/s12517-016-2363-4.

Mendes RM, Lorandi R (2008) Analysis of spatial variability of SPT penetration resistance in collapsible soils considering water table depth. Eng Geol 101:218–225. https://doi.org/10.1016/j.enggeo.2008.06.001.

Parsons RL, Frost JD (2002) Evaluating Site Investigation Quality using GIS and Geostatistics. Journal of Geotechnical and Geoenvironmental Engineering 128(6):451-461. https://doi.org/10.1061/(ASCE)1090-0241(2002)128:6(451).

Rogers JD (2006) Subsurface Exploration Using the Standard Penetration Test and the Cone Penetrometer Test. Environmental and Engineering Geosciences 12 (2):161-179. https://doi.org/10.2113/12.2.161.

Royse KR, Rutter H, Entwisle D (2009) Property attribution of 3D geological models in the Thames Gateway, London: new ways of visualizing geoscientific information. Bull Eng Geol Environ 68:1–16. https://doi.org/10.1007/s10064-008-0171-0.

Saudi General Authority for Statistics (2018) "Saudi Arabia Regions and Major Cities: Population Statistics, Maps, Charts, and Weather." http://www.citypopulation.de/en/saudiarabia/cities/ (Oct. 12, 2022).

Shanti AM (1993) Geology of the Arabian Shield. King Abdulaziz University Press, Jeddah, Saudi Arabia

Stern R, Johnson P (2010) Continental lithosphere of the Arabian plate: a geologic, petrologic and geophysical synthesis. Earth Sci Rev 101:29–67. https://doi.org/10.1016/j.earscirev.2010.01.002.

Tang C, Xu Q (2009) Approach on geohazards risk management for urban in a strong seismic zone. Journal of Engineering Geology 17(1):56–61.

Thierry P, Prunier-Leparmentier A, Lembezat C, et al (2009) 3D geological modeling at urban scale and mapping of ground movement susceptibility from gypsum dissolution: the Paris example (France). Eng Geol 105:51–64. https://doi.org/10.1016/j.enggeo.2008.12.010.

Tobore A, Senjobi B, Oyerinde G, Bamidele (2023) Geospatial Soil Suitability Assessment for Maize (Zea mays) Production in Derived Savanna of Agricultural Research and Training, OYO STATE, Nigeria. The Jordan Journal of Earth and Environmental Sciences (JJEES) 14 (1): 9-18

Vincent P (2008) Saudi Arabia: an environmental overview. Taylor and Francis, Netherlands.

JJEES

JJEES (2023) 14 (3): 195-202
ISSN 1995-6681

Jordan Journal of Earth and Environmental Sciences

Surficial Survey of Unstressed Aquifers for Saltwater-freshwater Interaction using 2D Inverse Resistivity Model and Saltwater Markers in the Coastal Area of Ogheye in the Niger Delta Basin, Nigeria

Oghenero Ohwoghere-Asuma*, Kizito Ejiro Aweto, Glory Ovwamuedo, Daniel Ugbome

Department of Geology, Delta State University, Abraka, Nigeria

Received 9th August 2022; Accepted 18 February 2023

Abstract

The flow and interaction of freshwater and saltwater have a significant impact on how much freshwater is available in coastal aquifers. For effective management of groundwater resources in aquifers adjacent to the sea, identification of the saltwater-freshwater interface position is necessary. The objective of the study is to define the salinity of aquifers by integrating a 2D resistivity model of the subsurface with total dissolved solids (TDS), electrical conductivity (EC), molar ratios of Na^+/Cl^- and Mg^{2+}/Ca^{2+}. The geologic models created from the resistivity data revealed a gradual increase in resistivity both laterally and vertically as the distance from the sea increases. The saltwater-freshwater interaction zone is located between 415 and 485m and also at 735 and 885m from the coast. Near the sea, saltwater extends to a depth of 24 meters, below which there is likely an uninvaded zone. Geochemical indicators of groundwater from 37m and 69m depths indicated no significant evidence of saltwater incursion. Interaction between freshwater and saltwater is evident in aquifers between 2.3 and 4.3m depths with TDS and EC exceeding 3000 mg/l and 5000μS/cm, as well as ratios of Na^+/Cl^- between 0.54 and 0.64 and Mg^{2+}/Ca^{2+} between 4.1 and 4.5. Without extensive active pumping, geogenic factors are probably responsible for the salinization of aquifers in the areas. The backwater influx of saltwater into shallow aquifers during the dry season is attributed to the intrusion of aquifers. The existence of a clay layer of considerable thickness under the saltwater zones provides adequate protection against groundwater from 38 to 69m depths, respectively.

Keywords: *Coastal aquifers; Resistivity imaging; Ionic ratios; Saltwater intrusion; Saltwater/freshwater interface, Benin Formation*

1. Introduction

The Benin Formation beneath the Niger Delta coastal region is characterized by an abundance of groundwater resources. The salinization and proximity of aquifers to the seashore hinder the availability of freshwater in the coastal regions. The groundwater in most estuary environments, where continental groundwater mixes with saltwater from the sea are under serious threat from intrusion. The threat may emanate from geogenic factors and overstressing of coastal aquifers (Abam 2001; Post 2005). As a result, coastal aquifers are frequently contaminated by saltwater and the attendant effect is groundwater quality degradations (Batayneh 2006) and also, reduction in freshwater quantity. The salinization of coastal aquifers in the Niger Delta has been a cause of concern, but decision-makers and groundwater resource managers have not taken it seriously. Boreholes in these regions are frequently abandoned few months after drilling, owing to seawater intrusion (Ohwoghere-Asuma et al. 2017) and lack of proper geophysical investigation.

Fresh groundwater supply for home and industrial use is dwindling and increasingly becoming more expensive to harness as a result of intrusion. The impact of intrusion extends not only to groundwater but also to soil fertility. Excessive pumping, geologic formation, hydraulic conductivity, and recharge influence the degree to which salinization impacts coastal aquifers (Abd-Elaty and Zelenakova 2022; Urish and Frohlich, 1990; Frohlich et al. 1994; Freeze and Cherry, 1979; Choudhury et al. 2001). The influx of saltwater into freshwater aquifers leads to a significant reduction in the resistivity of groundwater. The presence of discernible contrast between the resistivity of freshwater and saltwater is utilized to delineate one from the other (Griffith and Barker, 1993). Electrical resistivity techniques have gained enormous interest globally and have been successfully utilized to detect the freshwater/saltwater interface in coastal aquifers (Barker, 1980) and delineation of potential aquifers in both basement complexes and sedimentary environments (Okogbue and Ukpai, 2013; Al-Amoush et al., 2017). Various researchers have used electrical resistivity surveys to analyze saltwater intrusion in various coastal places across the world (Yang et al. 1999; Batayneh, 2006; Bauer et al. 2006; Choudhury et al. 2001; Kruse et al. 1998; Nowroozi et al. 1999; Ohwoghere-Asuma et al. 2017; Ohwoghere-Asuma and Essi, 2017; Ohwoghere-Asuma, 2017a and b).

Furthermore, geochemical characteristics of groundwater have been employed as saltwater indicators in addition

* Corresponding author e-mail: ohwonero@gmail.com

to electrical resistivity in the delineation of intruded from non-intruded aquifers. Saltwater substantially has higher concentrations of Na^+, Cl^-, total dissolved solids (TDS), and electrical conductivity (EC) than freshwater. Since seawater is characterized by high concentrations of Na^+, Cl^-, and TDS, it is generally denser than freshwater in the same aquifer. The core driving force behind intrusion is the density contrast between freshwater and saltwater. When an aquifer is pumped intensively, intrusion frequently begins by either migrating laterally from the sea or an underlying aquifer (upconning). In upconning, freshwater occurs floating on top of saltwater in the aquifer (Ohwoghere-Asuma (2017a, b). The molar ratio of Na^+ to Cl^- concentrations in seawater is 0.86, indicating that the Cl^- is considerably in excess of Na^+ and hence the fraction is less than unity (1). Furthermore, the Mg^{2+} to Ca^{2+} ratio ranges from 4.5 to 5.2 (Jones et al. 1999), indicating that Mg^{2+} concentration in seawater is substantially greater than Ca^{2+} concentration. Freshwater aquifer experiencing interaction is often characterized by TDS in excess of 200mg/l, Cl^- in excess of 100mg/l, and EC in excess of 3000S/cm (Karahanoglu, 1997). These critical criteria have necessitated their use as a proxy for delineating freshwater from intruded aquifers, especially the interface between them.

The accurate prediction and monitoring of freshwater/saltwater interface movement in response to both natural and anthropogenic forcing, including aquifer over-pumping, is required for the successful management of coastal groundwater resources. The study area is thinly populated and therefore lacks adequate conditions consequential for the over-pumping of shallow aquifers. In this context, the objective of this study is to use 2D electrical resistivity tomography and validated by lithology and geochemical indicators, to determine the intrusion saltwater and the relative position of the freshwater/saltwater interface in the subsurface aquifers adjacent to the sea.

1.2 Location, Geology, and Geomorphology

The area under investigation consists of three communities of Ogheye-Eghoroke, Ogheye-Orere, and Ogheye- Dimigu, they are situated on both sides of the Benin River and facing the Ocean, the Gulf of Guinea. This area is the region of the western Niger Delta where the Benin River discharges into the Gulf of Guinea. The location of the area under investigation on the Niger Delta region coordinate can be found on the latitude that ranges from 05°46′21.1″ to 05°46′48.5"and longitude that ranges from 05°04′2.2″ to 05°04′15.6″ (Figure 1). It is bounded in the west and east by the ocean and networks of tidal inlets and distributaries of the Benin River respectively. In terms of topography, annual rainfall, and temperature, the area is not distinctive from other parts of the coastal Niger Delta. It consists dominantly of the saltwater mangrove swamps of the four geomorphologic units of the Niger Delta.

The Niger Delta was formed as the result of the building up of fine-grained sediments eroded and transported by the River Niger and its tributaries which began in early Paleocene times. The Niger Delta is composed of three subsurface lithostratigraphic units; Akata, Agbada, and Benin Formations (Reyment, 1965; Short and Stauble, 1967). The basal Akata Formation was deposited in the marine environment during low stands. It consists of thick shales with minor clays, silts, and occasionally turbidite sand lenses.

The Formation which has a relative thickness of 20,000ft (5882m) is rich in organic matter and is the source of oil in the Niger Delta basin. The Agbada Formation which overlies the Akata Formation was deposited under a transitional environment, with a composition of alternating parallic sequences of sands and shales. The upper portion is predominantly sand with clays increasing with depth. The Benin Formation (2100m thick), which caps the sequence in the region and comprises over ninety percent (90%) fine–coarse-grained sands with intercalations of clay/shale interbeds.

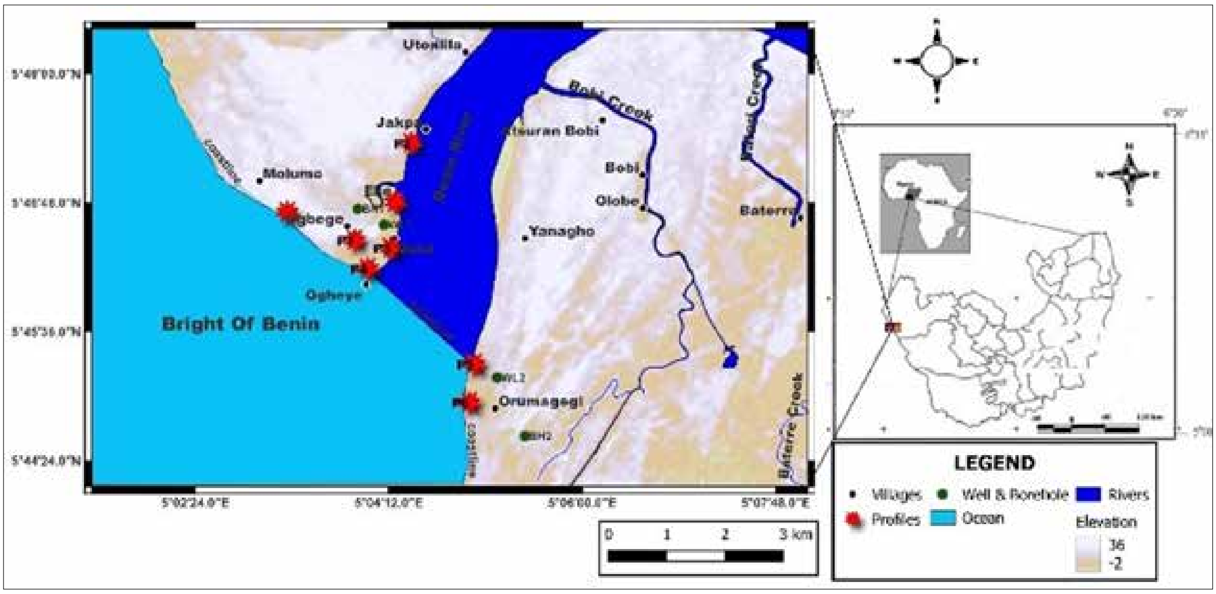

Figure 1. Map of the study area showing profiles and groundwater samples locations.

The Niger Delta is characterized by four (4) major intergradational geomorphological units (Etu–Efeotor and Akpokodje, 1990). These units occur from sea to land as abandoned and active coastal islands; beaches; saltwater mangrove swamps, estuaries, creeks, and lagoons; extensive freshwater swamps and meander belts, dry deltaic plains with rare freshwater swamps.

2. Materials and methods

Using the ABEM SAS 4000 Tarrameter in the Wenner setup with a current electrode separation of 5m, eight (8) electrical resistivity tomographies (ERT) were acquired. The roll-along approach was used manually to acquire 2D resistivity data. RES2DINV, an iterative forward modeling tool, was used to invert the measured apparent resistivity data (Loke, 2000; Loke and Barker, 1996). The program generates a two-dimensional resistivity model of the subsurface based on the measured resistivity data provided. The first stage of processing involves the creation of pseudosections, which are preliminary images of the subsurface, while the second stage involves the transformation of measured apparent resistivity values into computed resistivity values using a quick inversion method (Loke, 2000). The subsurface geology is divided into rectangular blocks using an inversion routine based on the smoothness-constrained least-squares optimization method. The model block resistivity is adjusted to minimize the discrepancy between the measured apparent resistivity and the computed values. The RMS (root mean square) error quantifies this disparity (Loke and Barker, 1996; Sasaki, 1992). Tying lithologic logs from BH1 and BH2 (Figure 2) that are close to profile locations aided in the delineation of geologic information from resistivity models.

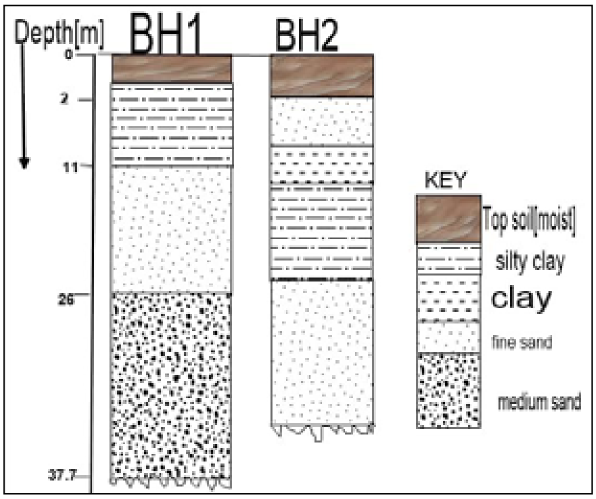

Figure 2. lithology logs depicted the subsurface geology of Ogheye-Eghoroke and Ogheye-Orere.

2.1 Groundwater collection and laboratory analysis

Four groundwater samples were collected from 2 hand-dug wells and two boreholes, as well as river samples. Groundwater data are insufficient and restricted to only four samples due to the logistic transportation of drilling equipment to the coastal region of the Niger Delta. The boreholes were logged, and depths and lithologies were tied to and aided the interpretation of 2D resistivity data. The water samples were collected from Ogheye-Eghoroke and Orere. They were collected with one-liter plastic containers, and except for those for anions analysis, a specified volume of HNO_3^- was added to samples for major cation analysis. At the time of collection, samples were stored in the field with an ice cooler box and refrigerated at 4^0 degrees Celsius before being transported to the laboratory for analysis.

Unstable parameters of TDS, pH, and electrical conductivity (EC) were measured in situ with a Hanna hand-held H19831 model and pH meter. Others, such as Ca^{2+}, Na^+, Mg^{2+}, and Cl^-, were determined in the laboratory. These ions were chosen because they contain saltwater intrusion markers such as Cl^-, Ca^{2+}, Na^+, TDS, and EC. The major cation was examined in the laboratory using Inductively Coupled Plasma Optical Emission Spectrometry (ICP-OES), whereas the anion was analyzed with Ion Chromatography. The results of the laboratory analysis were subsequently compared with national and WHO drinking standards (NSDQW 2007; WHO 2017).

3. Results and discussion

Table (1) and Figures (3and4) show the summarized interpretations of 2D resistivity structures and pseudo sections for the eight profiles. In general, all profiles demonstrated lateral and vertical variation in resistivity. Lower electrical resistivity values were found on the profile's western (sea) sides. This could be attributed to saltwater-saturated underlying strata intruding the aquifers from the sea. Resistivity increases immediately to the east, which is typical of freshwater aquifers located further inland from the coast.

The low and gradational resistivity zones revealed by the geologic models of the subsurface seen in models 2,3, and 5-7 in Figure 3 above strongly suggest groundwater undergoing marine incursion into inland freshwater aquifers. Due to intrusion, the groundwater in the area is evolving from freshwater to saltwater type. The trend of resistivity values laterally and vertically reflects the different groundwater types identified. This evolution can also be explained by the interplay of the freshwater/saltwater interface with the nearby aquifer (Walraevens and Van Camp, 2004). The end outcome is a degradation of groundwater quality due to intrusion, which has been shown to diminish with distance from the land. The vertical thickness of salt water appears to be thicker than 24m near the sea and reduces significantly to around 12m landward (Figure 3), which illustrates the geometry of the aquifer adjoining the sea that is experiencing intrusion. Laterally, saltwater is about 100m away, while freshwater is around 600m away. Geogenic processes and artificial abstraction are both known to contribute to the salinization of the aquifers next to the sea (Basack et al. 2022; Aladejana et al. 2020; Post, 2005; Urish and Frohlich, 1990). The most known important factor causing the saltwater intrusion is overstressing of coastal aquifers through severe pumping (Nowroozi et al. 1999; Post, 2005). The low resistivity zones seen in the area are most likely caused by geogenic processes rather than aquifer overstressing. This assertion is supported by evidence revealed from the groundwater flow and simulation of saltwater intrusion into aquifers (Ohwoghere–Asuma et al. 2021).

Table 1. Summary of interpretation of 2D pseduesections and geological inferences of profiles 1 to 8.

Location	Profile No.	Resistivity (Ωm)	Lateral distance	Depth (m)	Inference
Ogheye-Eghoroke	1	2.13-3.05	5-50	1.2-24	Saline water
		3.05-6.69	75-105	7-24	Saline water
		76-125	185-585.8	1.25-24	Saline water
		3.21-5.29	5-85	1.2-24	Saline water
	2	5.29-18.9	85-245	1.2-24	Saline water
		81-111	325- 725	1.2 – 14	Freshwater
		4.21-7.17	5-165	1.25-14	Saline water
	3	12.2-20	85-325	12.4 -24	Saline water
		75-126	45-725	1.25-24	Freshwater
		0.72- 3.67	5-325	1.2-12.4	Saline water
Ogheye -Orere	4	8.26-18.6	85-415	12.4-15.6	Saline water
		94-212	85-485	12.4- 24	Freshwater
		0.32- 4.47	5- 405	1.3 – 10.2	Saline water
	5	5- 23.1	5-485	1.25-19.5	Saline water
		0.85-5.57	5-165	1.25-19.5	Saline water
	6	10-36.4	645-735	15.9-19.8	Saline water
		78-119	485-885	20-24	Freshwater
Ogheye-Dimigu		0.89-5.24	5-245	1.25-10.5	Saltwater
	7	9.81-34.3	245-385	1.25-9.37	Saline water
		70-108	485-895	9.25-24	Freshwater
		1.13-2.78	5-165	1.15-9.25	Freshwater
	8	6.92-23.2	65-405	1.15-24	Saline water
		77-100	405-485	1.25-24	Freshwater

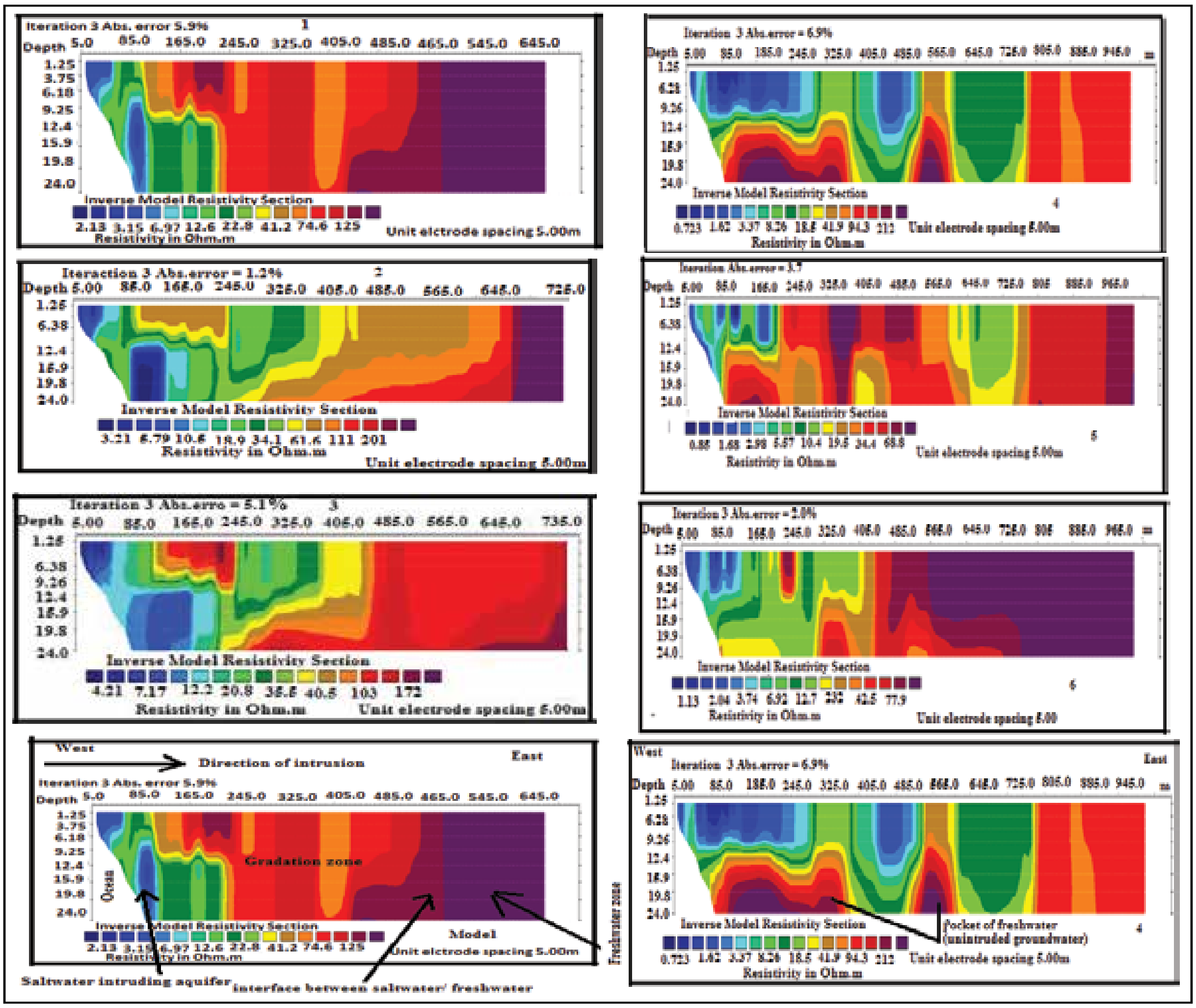

Figure 3. 2D electrical resistivity models of profiles 1-4 and 4-6 and subsurface geologic models for Ogheye–Eghoroke (right) and Ogheye- Orere (left).

Using various scenarios that reflected realistic and unrealistic water demand in most settlements along the Niger Delta coast revealed that groundwater demand is on a small scale. Pumping groundwater from these locations is not sufficient to drive intrusion. The reason is that the population in these areas is thinly populated as compared to the landed regions of the Niger Delta, which are profoundly populated. The effects of sea level rise and ocean tides on saltwater intrusion into coastal aquifers are also well documented (Panthi et al. 2022) may be responsible for the intrusion observed in the area. During transgression, marine water normally migrates towards the continent, resulting in seawater contamination of aquifers.

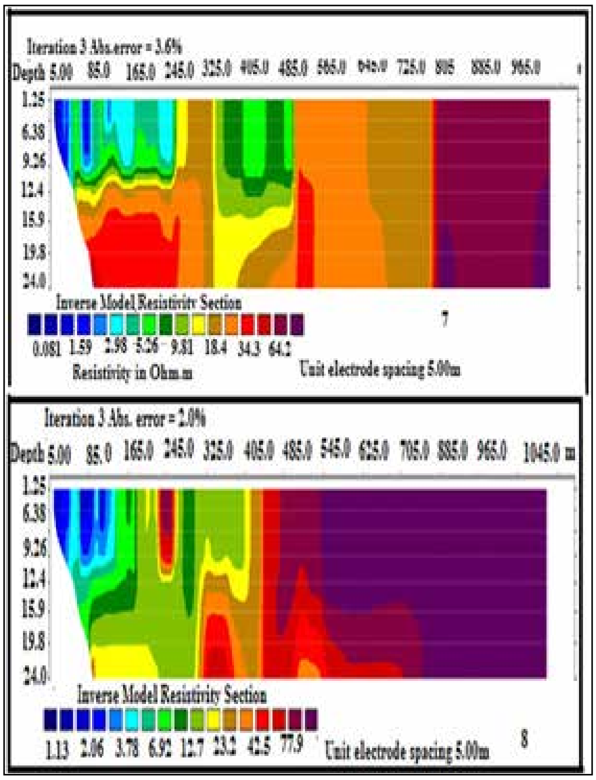

Figure 4. 2D electrical resistivity models of profiles 7-8 and subsurface geologic models for Ogheye–Dimigu.

A cursory analysis of Figures 3 and 4 reveals zones of low resistivity, which are most likely saltwater leftovers from the last time transgression. Similar low resistivity groundwater has previously been observed at shallow depths near the Lagos coastal area (Oyedele, 2001) and the Escravos area of the western Niger Delta (Ohwoghere-Asuma, 2017a), both were assumed to have been caused by marine transgression. The aquifer directly adjacent to the ocean was primarily affected by tide-induced intrusion, particularly at the high tide mark of the beach. In such cases, the high tide mark (upper shoreface) is flooded with a significant amount of seawater intermittently during high tide, which then infiltrates into the subsurface to contaminate groundwater. As demonstrated by Ohwoghere-Asuma (2017a) for the Escravos area, this is common in most upper seashores of the basin. Aside from flooding at the high tide mark, saltwater seepage from the Benin River into the underneath aquifer is possible. This is further demonstrated by the change in water quality inside the tidal reach that is dependent on the makeup of the original river water and the seawater. A zone of mixing and diffusion migrates up and down the river, generating a cyclic diurnal change in water quality, with the most saline contamination occurring during high tide and the least contamination occurring during low tide. During the dry season, when river levels are at their lowest ebbs owing to a lack of rain, rivers in estuaries are salinized by tides induced by an influx of seawater upstream (Abam, 1999). The water quality appears saline and further inland in the lower region of the estuary than in primary freshwater. The distances salinized upstream typically range from less than 1km to tens of kilometers, so saltwater is confined to the riverbank. When aquifers in coastal areas are hydraulically connected to rivers within the estuarine reach of the stream, saltwater may encroach into the underlying freshwater aquifers depending on the relative positions of the water table and the river stage; this is most likely reflected in the subsurface geologic models depicted in Figures 3 and 4. Because of the huge discharge of freshwater that dilutes intruded aquifers during the rainy season, the influence of tides on water quality is negligible during the rainy season. As a result, it is assumed that the saltwater seen near the river bank is caused by tidal influences.

3.1 Geochemical markers

Ambiguity is frequently encountered while inferring geologic information from subsurface resistivity investigations, highlighting the importance of subsurface lithology for effective resistivity data interpretation. Subsurface geology is frequently used to evaluate 2D resistivity interpretations to avoid ambiguity with an adequate depiction of the subsurface. To correlate the salinity of groundwater with depths explored with 2D resistivity data, groundwater geochemical facie was used to determine whether or not aquifers have been intruded with saltwater from the neighboring marine environment. As a result, four groundwater samples from two boreholes and two dug wells were tested for intrusion markers. The pH values shown varied from 6.3 to 7.4 (Table 2), indicating that the groundwater is moderately acidic and slightly neutral. This is typical of most aquifers in the Niger Delta basin, as groundwater from these locations is typically fresh, somewhat acidic, and has a high dissolved Fe^{2+} concentration.

Table 2. Physiochemical composition of the groundwater and Benin River of the study areas.

Sample	pH	EC (µS/cm)	TDS (mg/l)	Ca^{2+} (mg/l)	Na^{+} (mg/l)	Mg^{2+} (mg/l)	Fe^{2+} (mg/l)	Cl^{-} (mg/l)	Depth (m)
HDW1	7.4	8100	4000	34.42	102.68	93.96	0.02	264.	2.30
BH1	6.3	267	135	13.41	15.6	12.20	0.01	12.18	37. 18
HDW2	6.7	8000	4000	31.88	88.92	79.29	0.02	234.90	4.60
BH2	6.5	1432	715	16.68	98.64	18.21	0.03	67.82	68.78
Benin River	7.4	84000	4000	69.74	246.67	89.45	0.03	456.89	

The parameters of EC, TDS, and Cl^-, which are commonly utilized as proxies for saltwater intrusion are defined by concentrations that are more than the Nigerian and WHO standards for drinking water (NSDQW, 2007; WHO, 2017). Kim et al. (2003) discovered that aquifers that have been intruded by saltwater typically exhibit ECs above 5000S/cm. Furthermore, the mixing of freshwater and saltwater in the aquifer can be deduced from EC values greater than 3000μS/cm (Karahanoglu, 1997). Table 2 exhibited EC values ranging from 267 to 8400μS/cm. Those above 5000μS/cm are from dug wells with ECs of 8100 and 8000S/cm, respectively. This could indicate that these shallow-dug wells have been subjected to intrusion. Backwaters with direct access to the sea may be a source of intrusion, especially during the dry season. This backwater influx is confirmed in October 2021, when the levels of EC and TDS of HDW1 measured were observed to decrease from 81000S/cm and 4000mg/l to 2217S/cm and 1093mg/l, respectively. The decrease in values is caused by a large input of freshwater from the landward side, which forces saltwater inward into the sea during the wet season. Elango and Manickam (1987) and UNDP (1987) provided a similar argument for the Bay of Bengal and the Buckingham Canal.

TDS levels greater than 2000mg/l indicate that saltwater has intruded the freshwater aquifer. The TDS values shown in Table 2 for dug wells are significantly greater than those for boreholes, ranging from 235 to 4000mg/l. HDW1 and HDW2 are with values that exceeded this, except BH1 and BH2, respectively. The ionic ratios of Na^+/Cl^- and Mg^{2+}/Ca^{2+} have been used to distinguish between freshwater and saltwater aquifers. A non-intruded freshwater aquifer is characterized by having $Na^+/Cl^- > 1$ and an intruded aquifer is 0.86 (Vengosh and Rosenthal, 1994). The Na^+/Cl^- for HDW1 and HDW2 are 0.64 and 0.58, respectively, and those for the BH1 and BH2 are 1.97 and 2.24, respectively. The ratios of Na^+/Cl^- of groundwater from HDW1 and HDW2 are lesser than 0.86 required for aquifer experiencing intrusion. The low ratio values that are lesser than 0.68 is suggestive of the initiation of salinization of groundwater from HDW1 and HDW2. The Na^+/Cl^- of groundwater from BH1 and BH2 exceeded one (1) required for a coastal aquifer to be regarded as freshwater. Again, this indicates that BH1 and BH2 with depths of 37m and 69m, respectively, are freshwaters and therefore have not experienced intrusion.

Mg^{2+}/Ca^{2+}ratio in freshwater aquifers intruded by saltwater ranges between 4.3 and 5.2 (Jones et al., 1999). The Mg^{2+}/Ca^{2+}ratios of BH1 and BH2 are 1.5 and 1.8, respectively, while HDW1 and HDW2 are 4.5 and 4.1, respectively. These values are consistent with the Na^+/Cl^- ratios as well as the TDS and EC values; however, the high TDS, EC, and ratios of Na^+/Cl^- and Mg^{2+}/Ca^{2+}values show that the quality of water in the dug wells have been compromised by intrusion whereas the boreholes were not. These indicators appear to have verified the subsurface geology model in that intrusion is significantly limited to shallow aquifers with depths ranging from 2.3 to 4.3m. Although the depth inferred from the 2D resistivity model is 24m, it is shallower than the depths of 37m and 69 meters for the borehole whose water is fresh. These depths are comparable to those found in Ohwoghere-Asuma's (2019) previous investigation using vertical electrical sounding. This aquifer could have been protected by a thick layer of clay, which could have served as a barrier to intrusion. Since the geochemical markers of the groundwater from these boreholes are below allowable limits, the intrusion does not affect aquifers in these communities located 400 to 500 meters from the sea.

4. Conclusions

The underlying geology revealed by borehole lithologic logs and interpreted 2D resistivity data indicates a lithostratigraphy of silty clay, clay, fine sand, medium, and coarse sand. Saline water is restricted to depths ranging from 2.3 to 4.6 meters due to silty clay. Groundwater geochemical markers from these depths strongly indicated intrusion. At depths near the upper shoreface, saline water can be found at 24m, although it decreases to 12m as the distance from the coast increases towards land, whilst water at this depth is fresh further inland.

The current study was successful in displaying electrical resistivity tomographies of the subsurface geology, which aided in the establishment of saltwater-freshwater interaction and delineation of the interface, which is located between 415 and 485m, and 735 and 885m from the sea at Eghoroke and Orere, respectively. The resistivity model displays a strong trend of increasing resistivity landward from the ocean, indicating that groundwater salinity is decreasing. Groundwater in the studied area was classified into three types and three distinct zones based on resistivity image values: very low resistivity zones suspected to be areas affected by intrusion located near the ocean, mixing (transition) zones of salt water with fresh water, and a zone of only freshwater.

The validation of the 2D electrical resistivity data with lithologic logs and total dissolved solids (TDS), electrical conductivity (EC), and molar ratios of Na^+/Cl^- and Mg^{2+}/Ca^{2+} of groundwater from boreholes in the study has significantly increased the likelihood that intrusion is on a very small scale and limited to shallow aquifers. In this study, the small scale of intrusion discovered is substantially adduced to the lack of intensive pumping, which could lead to a drop in the hydraulic heads of aquifers on the landward side of the ocean. However, the intrusion is caused and controlled by the influx of backwater from the sea into the freshwater aquifers during the dry season, when the Benin River discharge is relatively low.

Based on the information presented in the paper, we recommend that groundwater development for optimal freshwater abstraction be located at least 450m away from the ocean, and monitoring wells be drilled to depths of 38 to 70m deep to monitor intrusion. Groundwater from these proposed drilled wells should be tested for physicochemical characteristics to determine water quality frequently.

References

Abam, T. K. S. (1999). Dynamics and quality of water resources in the Niger Delta. In: Ellis, J. B. (Ed) Impacts of Urban Growth on Surface Water and Groundwater Quality. Proceedings of IUGG Symposium HS5, Birmingham, 429 –437.

Abam, T. K. S. (2001). Regional hydrological research perspectives in the Niger Delta, Hydrological Sciences,46(1):13 – 25.

Abd-Elaty, I. and Zelenakova, M. (2022). Saltwater intrusion management in shallow and deep coastal aquifers for high aridity regions, Journal of hydrology; regional studies. 40, 2-17.

Aladejana, J.A., Kalin, R.M., Sentenac, P, and Hassan, I. (2020). Hydrostratigraphic Characterization of Shallow Coastal Aquifers of Eastern Dahomey Basin, S/W Nigeria, Using Integrated Hydrogeophysical Approach; Implication for Saltwater Intrusion. Geosciences, 10, 65. https://doi.org/10.3390/geosciences10020065

Al-Amoush1, H., Rajab, J. A., Al-Tarazi, E., Al-Shabeeb, A. R.,, Al-Adamat, R., and Al-Fugara, A.(2017). Electrical Resistivity Tomography Modeling of Vertical Lithological Contact using Different Electrode Configurations.Jordan journal of earth and environmental science, 8(1): 27-34.

Barker R.D. (1980). Application of Geophysics in groundwater investigations. Water Survey, 84: 489 – 492.

Basack, S., Loganathan, M.K., Goswami, G.and Khabbaz, H. (2022). Saltwater intrusion into coaster aquifers and associated risk management; critical review and research directive. Journal of coastal research, 38(3),654-672.

Batayneh, A.T. (2006). Use of electrical resistivity methods for detecting subsurface fresh and saline water and delineating their interfacial configuration: a case study of the eastern Dead Sea coastal aquifers, Jordan, Hydrogeology Journal, 14: 1277 –1283.

Bauer, P., Supper, R., Zimmermann, S. and Kinzelbach, W. (2006). Geoelectrical imaging of groundwater salinization in the Okavango Delta, Botswana, Journal of Applied Geophysics, 60(2): 126–141.

Choudhury, K., Saha, D.K., and Chakraborty, P. (2001). Geophysical study for saline water intrusion in coastal alluvial terrain. Journal of Applied Geophysics, 46:189 –200.

Elango, L., and Manickam, S. (1987). Hydrogeochemistry of the Madras aquifer, India - Spatial and temporal variation in chemical quality of groundwater. Geological Society of Hong Kong Bulletin., 3, 525-534.

Freeze, R. A. and Cherry, J. A. (1979). Groundwater. Englewood Cliffs, NJ: Prentice Hall, Inc. pg. 450

Frohlich, R.K., Urish, D.W., Fuller, J.and Reilly, M.O. (1994). Use of geoelectrical method in groundwater pollution surveys in a coastal environment. Journal of Applied Geophysics, 32: 139–154.

Karahanoglu, N. (1997). Assessment of sea-water intrusion in a coastal aquifer by using correlation, principal component, and factor analyses, Water Environmental. Resource, 69(3), 331–341.

Kim, J. H., Kim, R. H. and Chang, H. W. (2003). Hydrogeochemical Characterization of major factors affecting the quality of shallow groundwater in the coastal area at Kimje in South Korea. Environmental geology, 478- 489

Kruse, S.E., Brudzinski, M.R. and Geib, T.L., (1998). Use of electrical and electromagnetic techniques to map seawater intrusion near the Cross-Florida Barge Canal. Environmental and Engineering Geoscience, 4: 331 – 340.

Jones, B. F.; Vengosh, A.; Rosenthal, E. and Yechieli, Y. (1999). Geochemical investigation of groundwater quality. Seawater intrusion in coastal aquifers- concepts, methods, and practices,

51–71.

Loke, M. H. (2000). RES2DINV Version 3.44 for Windows 95/98 and NT: Rapid 2D Resistivity and IP Inversion Using the Least-Squares Method. Advanced Geoscience Inc., Austin, TX., USA.

Loke, M.H. and Barker, R.D., (1996). Rapid least-squares inversion of apparent resistivity pseudo sections by a quasi-Newton method, Geophysical Prospecting, 44(1):131 – 152.

NSDQW (2007). Nigerian standard for drinking water quality approved by the standard organization of Nigeria; Nigeria industrial standard NIS 554; 2007.

Ohwoghere-Asuma, O., Chinyem, I.F, and Essi, O. E. (2017). Saltwater Intrusion Appraisal of Shallow Aquifer in Burutu Area of the Western Niger Delta with 2D Electrical Resistivity Tomography. Journal of Applied. Science and. Environmental Management, 21 (2): 372-377. https://dx.doi.org/10.4314/jasem.v21i2.19.

Ohwoghere-Asuma, O. and Essi, O. E. (2017). Investigation of Seawater Intrusion into Coastal Groundwater Aquifers of Escravos, Western Niger Delta, Nigeria Journal of Applied. Science and. Environmental Management, 21 (2): 362-369. ttps://dx.doi.org/10.4314/jasem.v21i2.18.

Ohwoghere-Asuma, O. (2017a). 2D Electrical Resistivity Imaging of the Effect of Tide on Groundwater Quality in Ogulagha Estuary, Western Niger Delta, Nigeria. Scientia Africana,1 6(1): 122- 225.

Ohwoghere-Asuma, O., (2017b). Delineation of Saltwater Zones around the Coastal area of Ogidigben in the Western Niger Delta from 2D Electrical Resistivity Tomography. Scientia Africana, 16(2):245-267.

Ohwoghere-Asuma, O., (2019). Mapping Shallow Aquifers Intruded by Saltwater in the Coastal Area of Benin River in Western Niger Delta from Dar-Zarrouk Parameters. Nigerian Journal of Technological Research, 14(3)12-17.

Ohwoghere-Asuma, O., Oteng, F.M.and Ophori, D. (2021). Simulation of Saltwater Intrusion into Coastal Aquifer of the Western Niger Delta. Proceeding of the Mediterranean Geosciences Union (Medgu) annual meeting, Istanbul, Turkey 25-28th November 2021.

Okogbue, C. O. and Ukpai, S.N (2013). Geochemical evaluation of groundwater quality in Abakaliki area, Southeast Nigeria. Jordan Journal of Earth and Environmental Sciences, 5(1): 1-8

Oyedele, K.F. (2001). Hydrogeophysical and Hydrogeochemical Investigation of Groundwater Quality in some parts of Lagos, Nigeria. African Journal of Environmental Studies. 2(1): 31- 37.

Nowroozi, A.A., Horrocks, S.B. and Henderson, P. (1999). Saltwater intrusion into the freshwater aquifer in the eastern shore of Virginia: a reconnaissance electrical resistivity survey, Journal of Applied Geophysics, 42(1): 1–22.

Panthi, J. S., Pradhanang, M., Nolte, A, and Boving, T. (2022). Saltwater intrusion into coastal aquifers in the contiguous United States - A systematic review of investigation approaches and monitoring networks.

Science of total environment, 836, 245-267. https://doi.org/10.1016/j.scitotenv.2022.155641.

Post, V.E.A. (2005). Fresh and saline groundwater interaction in coastal aquifers: is our technology ready for the problems ahead, Hydrogeology Journal, 13(1): 20–123

Reyment, R. A. (1965). Aspect of the Geology of Nigeria. Ibadan University Press, Nigeria.135pp.

Sasaki, Y. (1992). Resolution of resistivity tomography inferred from numerical simulation, Geophysical Prospecting, 40: 453 – 464.

Short, K. C. and Stauble, A. J. (1967). Outline of Geology of Niger Delta. American Association of Petroleum Geologists Bulletin, 51:761–799.

UNDP (1987). Hydrogeological and artificial recharge studies, Madras Technical report. United Nations Department of Technical co-operation for Development, New York

Urish, D.W. and Frohlich, R.K. (1990). Surface electrical resistivity in coastal groundwater exploration, Geoexploration, 26: 267–289.

Vengosh, A. and Rosenthal, A. (1994). Saline groundwater in Israel: It is bearing on the water crisis in the country. Journal of. Hydrology, 156, 389–430.

Walraevens, K. and Van Camp, M. (2004). Advances in understanding natural groundwater quality controls in coastal aquifers. 18 SWIM. Cartagena 2004, Spain. (Ed. Araguás, Custodio and Manzano). IGME. 1-15.

WHO (2017). Guidelines for drinking-water quality 3rd ed. World health organization Geneva pp.564.

Yang, C., Tong, L. and Huang, C. (1999). Combined application of DC and TEM to seawater intrusion mapping. Geophysics, 64(2): 417 – 425.

JJEES

JJEES (2023) 14 (3): 203-209
ISSN 1995-6681

Jordan Journal of Earth and Environmental Sciences

Evaluation of Groundwater Quality and its Suitability for Drinking and Agricultural Use in F'kirina Plain, Northern Algeria

Salima Djoudi[1*], Séverin Pistre[2], Belgacem Houha[3]

[1] *Faculty of Natural and Life Sciences. Department of Ecology and Environment. Laboratory Water. Environment and Renewable Energy. The University of Abbes Laghrour. Khenchela. Algeria.*

[2] *Laboratoire HSM. Université Montpellier. CNRS. IRD – Montpellier. France severin.*

[3] *Laboratory Water. Environment and Renewable Energy. The University of Abbes Laghrour. Khenchela. BP 40000. Algeria.*

Received 12th April 2022; Accepted 1st March 2023

Abstract

The purpose of this study is to determine the parameters that control the quality of groundwater in an aquifer located between carbonated rocks and a Salt Lake (Garâat ET Tarf) that is commonly used for agriculture. Forty-Five groundwater samples have been collected from F'kirina Plain which covers an area of approximately 350 km^2. To assess groundwater quality and suitability for irrigation and domestic use, various physicochemical parameters such as pH, electrical conductivity, total dissolved solids, total hardness, calcium, magnesium, sodium, potassium, bicarbonate, sulfate, and chloride were examined. The suitability of the water for agricultural use was tested using Sodium adsorption ratio (SAR), and sodium percent, The results illustrate that all samples are suitable for irrigation purposes except a few locations. which values beyond the permissible limits. The groundwater of the investigated area presents three types of water Ca-HCO_3 in carbonate outcrops evolving towards Ca-SO_4 and Ca-Cl type in the Plio-Quaternary filling in the direction of the Sebkha. The mapping of concentrations shows the effects of aquifer exploitation and practices on human and natural contamination of groundwater.

Keywords: *Groundwater quality, Hydrochemical facies, SAR, Sodium percent.*

1. Introduction

Groundwater is a major element of total water resources in arid and semi-arid areas. and it has major implications for economic growth (Subyani and Al Ahmadi, 2010). Due to fast population growth. industrialization. urbanization. and agricultural use of fertilizers and pesticides. groundwater quality has become a major water resource issue (Joarder et al., 2008). Natural factors such as lithology. groundwater velocity. recharge water quality. rock–water interaction. and contact with various types of aquifers all play a significant role in groundwater quality (Helena et al., 2000, Khan et al., 2015). Several contaminants produced by a variety of sources contaminate groundwater (Okogbue et Ukpai, 2013). In an endorheic basin, the presence of a salt lake hydraulically connected to groundwater could also change the water salinity by reversing the natural groundwater flow due to overexploitation of the latter (Ghodbane et al., 2016). Salinity and sodium hazard indicators can be used as a criterion to find the suitability of irrigation waters (Nishanthiny et al., 2010; Al-Hadithi et al., 2019). The most widely accepted method is that of the United States Department of Agriculture (USDA). and the sodium absorption ratio (SAR) is an effective evaluation index for most irrigation fluids (Al-Bassam and Al-Rumikhani, 2003; Al-Paruany, 2018). The study area is located in Algeria's semi-arid zones. It is marked by scarcity and unequal distribution of water resources. with groundwater serving as the primary source for domestic. industrial. and agricultural needs. The focus of this research is to decipher the chemical differences in groundwater caused by natural and anthropogenic factors. as well as to determine its suitability for agricultural and home usage. It also seeks to assess the many hydrogeochemical mechanisms that influence groundwater quality. To examine the groundwater quality and classify the groundwater in the area into separate hydrochemical groups. typical graphical representations and statistical analysis were used.

2. Study area

The study area is located in the North of Algeria between 35° 39′ 50″ N and 7° 17′ 55″ E. This region includes the F'kirina Plain covers an area of approximately 540 km². It is limited to the North by the line of water formed by Djebel El Galaa Kebira (1246 m) and Djebel Amamat El Kebir (1203 m), on the South by the line of water formed by Djebel Boutekhma (1291 m) and Djebel Ahmar (1259 m), to the East by the watershed line formed by Djebel Fedjidjet (1291 m) and to the West by a large flat that corresponds to high "constant noises" Plains and by the Garaat Tarf (Fig. 1). The Sabkha of Garâat at Tarf. For the period 1960-2015, the mean annual rainfall in the study area ranges between 20 to 34 mm.

* Corresponding author e-mail: djoudi.ecologie@gmail.com

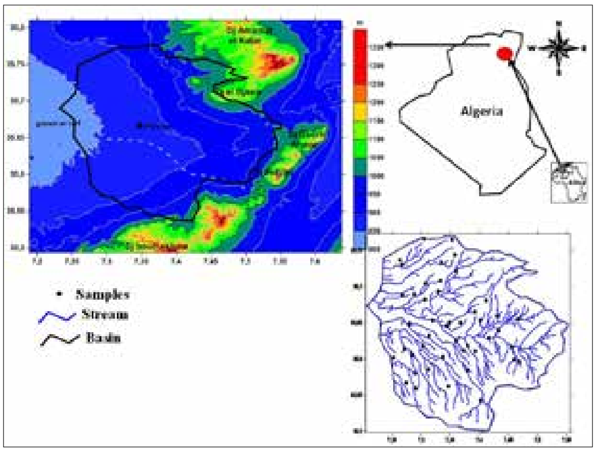

Figure 1. Localization of study area.

3. Geology of the studied area

The lithostratigraphy of the study area extends from Triassic to the Quaternary series and could be briefly presented in the following way (Figure 2):

In the study area, the Triassic Outcrop was observed in the Northeast and South West of Ain Delâa and F'kirina. Cretaceous Formations are represented by marl-limestone with platelet limestone at the base. It also appears on the surface in the northern margin of Ain Beïda where it is highly fractured. The Eocene Formations show a marly and a carbonate sequence separated by slightly sandstone facies. Outcrops of the Miocene present small dimensions and are only distributed in the southern part of the plain. It's a series composed of a set of marls limestones at the top, and a set of thick limestone layers at the center of the series (Salima and Belgacem, 2017).

The Pliocene is made up of sandy continental detrital deposits, conglomerates, marls, and reddish clays. Quaternary deposits have covered most of the plains. These deposits are very varied however the sedimentation is essentially clay and marly

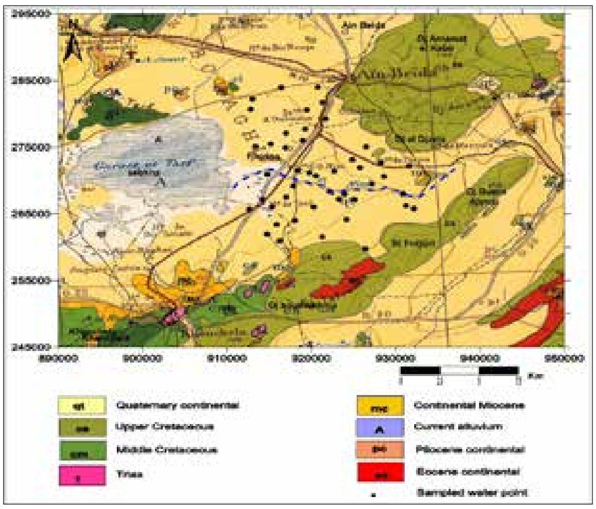

Figure 2. Geological map of the study area. (ANRH, 2012).

4. Method of Sampling and Analysis

Forty-five (45) groundwater samples were collected and analyzed in LACILAP Laboratory (Ain M'lila.) Algeria during Mai 2015. These sampling points were chosen on accessibility, integrity, and spatial distribution criteria. The procedure was carried out after a brief pumping time in polyethylene bottles. The physical parameters temperature, electrical conductivity, and pH were recorded on-site using a Multi–parameters. Analyses of the elements HCO_3- (bicarbonate), Na^+ (sodium), Cl- (chloride), SO_4^{2}- (sulfate), Ca^{2+} (calcium), Mg^{2+} (magnesium), Na^+ (sodium), K^+ (potassium), and NO_3- (nitrate) were performed by flame spectrophotometry, volumetry, and UV-visible spectrometry.

The global positioning system (GPS) was used to record the geographic location of each sampling point. All the geographic coordinates of the sampling location were imported in SURFER software v 12 for geospatial analysis and in the DIAGRAM v 6.4 program for the chemical facies.

5. Results and Discussion

The quality standards for drinking water have been specified by the World Health Organization (WHO) in 2017. The range of the physicochemical parameters (pH, EC, TDS, TH) and the major ions (Ca^{2+}, HCO^-_3, SO_4^{2-}, Mg^{2+}, Na^+, Cl^-, K^+, NO_3^{-}) and their comparison with WHO 2017 standards are presented in Table1.

Table 1. Statistical parameters of the chemical elements in groundwater. Min: minimum; Max: maximum; SD: standard deviation.

	Units	Min	Max	Mean	SD	WHO standard 2017
pH		6.700	8.000	7.323	0.302	6.5 -8.5
EC	µS/cm	437.000	6710.000	1106.356	965.560	500-1500
TDS	mg/L	451	6100	1047.38	884.460	500-1000
TH	°f	5	71 .6	11	8.96	100-500
Ca^{++}	mg/L	37.000	705.000	119.533	108.931	75-200
Mg^{++}	mg/L	2.000	412.000	41.600	59.298	50-150
Na^+	mg/L	1.000	665.000	85.644	108.036	200
K^+	mg/L	1.000	20.000	2.756	4.872	12
HCO_3^{--}	mg/L	101.000	1046.000	229.578	138.760	300-500
SO_4^{--}	mg/L	3.000	2645.000	278.711	412.770	250-400
Cl^-	mg/L	10.000	1085.000	157.111	172.586	250-400
NO_3^-	mg/L	0.000	124.000	35.222	30.956	45

The number and the good distribution at the basin scale allow interpolating the concentrations or chemical parameters values

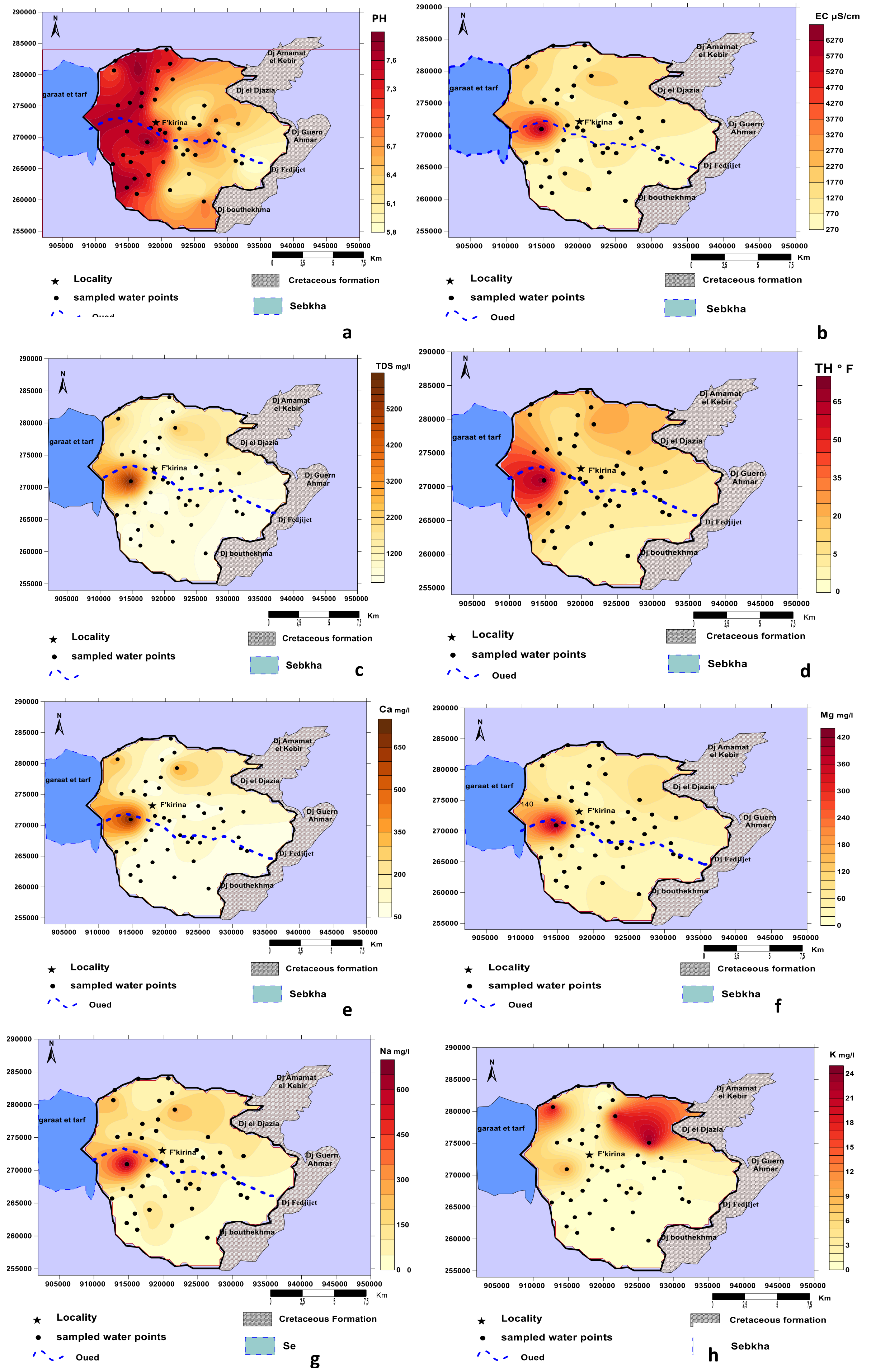
PH
EC µS/cm
TDS mg/l
TH ° F
Ca mg/l
Mg mg/l
Na mg/l
K mg/l
garaat et tarf
F'kirina
Dj Amamat el Kebir
Dj el Djazia
Dj Guern Ahmar
Dj Fedjijet
Dj bouthekhma
Km
Locality
sampled water points
Oued
Cretaceous formation
Sebkha
a
b
c
d
e
f
g
h

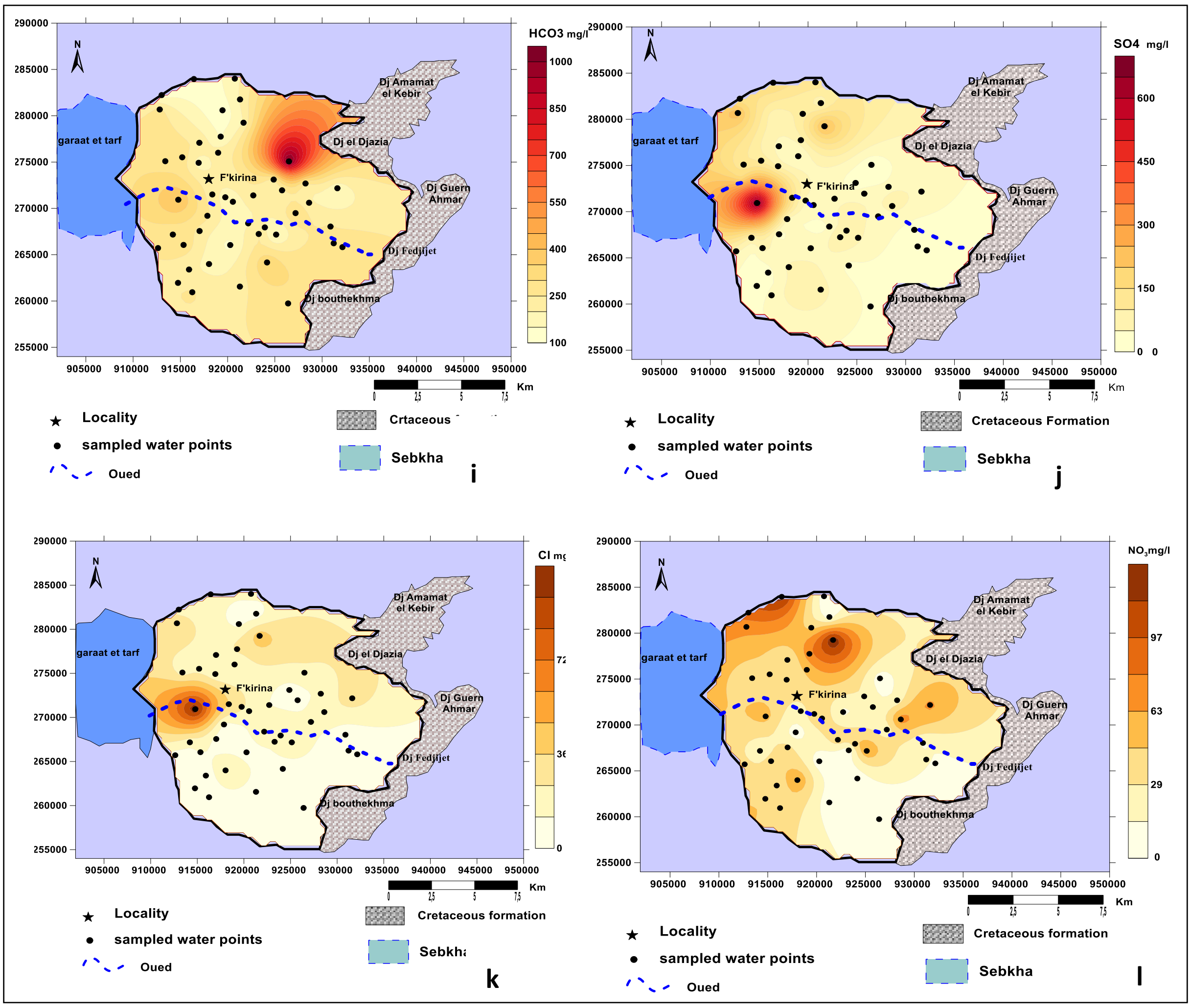

Figure 3. Map of F'kirina plain groundwaters for iso values of pH (a), EC (b), TDS (c), TH (d), Ca (e), Mg (f), Na (g), K (h), HCO_3 (i), SO_4 (j), Cl (k), NO_3(l).

5.1. pH

The measured pH values in all of the groundwater samples are uniform and close to neutral. It ranges from 6.7 to 8, with a mean of 7.30. The lowest values are found near carbonate deposits, while the highest values are found in the middle of the plain westward direction (Fig. 3a). This rise is very clear in the west part of the aquifer. It would be due to the water facies evolving (central zone). Natural phenomena such as the intrusion of sebkha waters (Garâat at Tarf) into the aquifers provide the highest pH values.

5.2. Electrical Conductivity (EC)

Electrical conductivity can be used as an approximate indicator of the total amount of dissolved material in water (Sarath Prasanth et al., 2012). Temperature, concentration, and the types of ions present all have a role (Hem, 1985). The study area's conductivity values range from 437 to 6710 µS/cm, with an average of 1106 µS/cm (Fig. 3b). A higher conductivity value indicates salt concentration in the groundwater. It rises towards Salt Lake (Garâat at Tarf), indicating that the salinity of the water rises in the flow direction. One point is distinguished by a higher value probably due to local anthropic or natural contamination.

5.3. Total Dissolved Solids (TDS)

TDS levels range from 451 to 6100 mg/L across the entire research area (Table 1). The use of agricultural fertilizer is responsible for higher total dissolved solids value. Nonetheless, only a few locations exceed the 1000-1500 mg/L drinking water standard. The TDS map logically shows the same tendencies as the EC map with the same high salinity point.

5.4. Total Hardness (TH)

The water hardness varies between (5 and 71°f), characterizing soft to moderately soft water from south to north and from east to west. In the west, the water becomes very hard (Fig. 3d). The previous point is also distinguished but the rise concerns other points close to the sebkha whose intrusions seems to have a major effect on water hardness rise. In the northern part, water is harder due to cretaceous carbonate aquifer as in the karstic spring Aïn Beïda.

5.5. Calcium and Magnesium (Ca^{+2} and Mg^{2+})

Calcium concentrations range from 37 and 705 mg/L (Table 4; Fig. 3e). The increased Ca^{+2} concentration (705 mg/L) was found substantially above the acceptable range for drinking water. Magnesium concentrations range between 2 and 412 mg/L (Table 1; Fig. 3f). The maximum Mg^{+2} concentration in drinking water that can be tolerated is 150 mg/L (WHO, 2017). Except in the western section of the image, the magnesium map shows that the Mg^{+2} level is rather low throughout practically all of the plain. In the northern part, Ca and Mg are separately more elevated but their addition explains the water hardness.

5.6. Sodium and Potassium (Na and K)

Sodium is always present in water from the leaching of geological formations rich in NaCl and the dissolution of clay and marl formations(WHO, 1984). The concentration of Na^+ in the study area varied from 1 to 665 mg/L. (Table 4; Fig. 3g). The maximum permissible limit of sodium is 200 mg/L.

The greater concentration of Na^+ seen around Garâat at Tarf could be the result of evaporation from the water table. In the rest of the study area, the lowest levels are found.

The concentration of K^+ is varying from 1 to 20 mg/l (Fig. 3h). The maximum permissible limit of potassium in the drinking water is 12 mg/l and it was found four water samples are above the permissible limit of WHO (Table 1). Three points in the northern part have elevated concentrations of K. Two of these seem correlated with moderate concentrations of K. The origin can be fertilizers or aquifer lithology.

5.7. Bicarbonate (HCO_3)

Bicarbonate is often the dominant ion in groundwaters but in the case of F'kirina plain, the values of HCO_3^- range from 101 to 1046 mg/L (Table 1). The repartition is quite homogeneous with low values but one point shows a very high concentration (Fig. 3i). The increased concentration of HCO_3^- in the groundwater source indicates that mineral dissolution is the dominant process (Stumm and Morgan, 2012).

5.8. Sulfate (SO_4^{-2})

Sulfate concentration in the study area ranges between 3 and 2645 mg/L. The average value of sulfate concentration is recorded as 278 mg/L. The spatial distribution of sulfate ion concentration in groundwater is illustrated in Fig. (3j). The results showed that the maximum concentration of sulfate is observed in the western part, on one isolated point close to the salt lake. This may be linked to a dissolution of formations rich in sulfate minerals, or contamination of the water table by the waters of Oued Nini or Garaat at Tarf, while the low concentration is observed in the eastern part of the study area.

5.9. Chloride (Cl)

The concentration of chloride in the study area ranges from 10 to 1085 mg/L (Fig. 3k). The acceptable chloride limit for drinking water is set at 250 mg/L (Table 1). The chloride concentrations are higher in the western and northwestern parts of the study area. The presence of too much chlorine in the water is commonly used as a pollution indicator and is referred to as tracer groundwater contamination (Loizidou and Kapetanios, 1993). A relative correlation appears with the Na map (Fig. 3g) which could indicate an origin from halite dissolution. The Pliocene continental detrital deposits are a heterogenous formation that contains evaporite deposits including halite.

5.9. Nitrate (NO3)

In the studied region, the sources of nitrate in groundwater are anthropogenic; It could be domestic wastewater, artificial fertilizers, or animal farms (Haycock and Burt, 1990)

The maximum permissible limit of NO_3^- is 45 mg/l (WHO, 2017), but several points are close to or exceed this value. There is no real tendency in the repartition but the map (Fig. 3l) revealed that significant nitrate concentrations were found in the north and northwest of the plain. The value is particularly elevated at point P10 (124 mg/l), this higher concentration is due to domestic wastewater from the agglomeration of F'kirina. On the other points, contamination is associated with agricultural practices.

6. Hydrochemical Facies

The term "hydrochemical facies" is used to describe the bodies of groundwater in an aquifer that are different from their chemical composition because of interaction with the surrounding rock and soil as water flows through an aquifer and assumes a characteristic chemical composition because of interaction with the surrounding rock and soil (Ravikumar and Somashekar, 2013).

The idea of hydrochemical facies is based on the assumption that, given current conditions, the chemical composition of groundwater at any point approaches chemical equilibrium with the matrix rocks. Hydrochemical facies interpretations can help determine mass flow patterns, origins, and chemical histories (Sarikhani et al., 2015). The concentration of major cations and anions in the Piper trilinear diagram can be used to understand the evolution of hydrochemical parameters in groundwater (Piper, 1944).

The representation of the results of chemical analyses on the Piper diagram defines three families of water globally distributed according to evolution from East to West. Out of limestone outcrops the water is Ca-HCO_3 type. The carbonate and Triassic formations can be the origin of these facies (Baali, 2007). whereas in the Plio-Quaternary fill; it becomes Ca-SO_4 type to finish towards a Ca-Cl water type near the Sebkha which can be explained by the influence of this latter and the presence of salt formations of Mio-Plio-Quaternary age (Gouaidia, 2008). (Fig. 4).

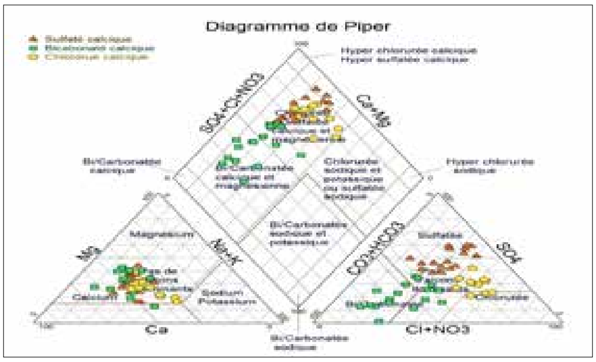

Figure 4. Piper diagram of the groundwater samples.

7. Irrigation Suitability

The suitability of groundwater for irrigation is evaluated using electrical conductivity (EC), percent of sodium (Na^{2+} %), and sodium adsorption ratio (SAR). Wilcox diagram (Na^{+}% vs EC plot) and USSL diagram (SAR vs EC plot) (El-Naqa et Al Adas, 2019).

7.1. Sodium Percent (Na%)

Percent sodium (Na%) is also commonly used to assess the suitability of water for irrigation (Wilcox, 1955). High sodium concentrations in groundwater have negative consequences because sodium reacts with soil to limit permeability and promote little or no plant development (Janardhana Raju et al., 2009, Vasanthavigar et al., 2010). The sodium percent (Na %) values were obtained by using the following equation: Na%= (Na/(Ca+Mg+Na+K))*100% where all ionic concentrations are expressed in meq/L. The water quality classification for irrigation purposes performed using the Wilcox diagram showed that 43% of the groundwater samples fall in the field of very good to good quality. 51 % fall in the field of good to permissible. 4 % fall in the field of doubtful for irrigation and 2 % fall in the unsuitable category (Fig. 5).

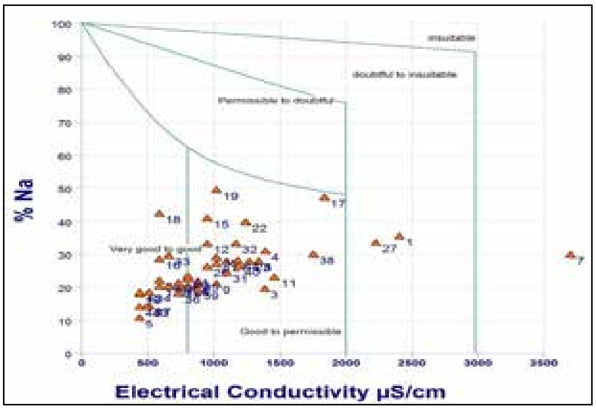

Figure 5. Wilcox diagram irrigation samples for groundwater quality.

7.2. Sodium Adsorption Ratio (SAR)

Because sodium concentration can decrease soil permeability and soil structure, the sodium adsorption ratio (SAR) is a measure of the suitability of water for use in agricultural irrigation (Todd and Mays, 2004). The sodium adsorption ration (SAR) is calculated using the following formula:

$$SAR = (Na/[(Ca+Mg)/2])^{1/2}$$

Where sodium, calcium, and magnesium concentrations are in meq/L.

The abundance of sodium in irrigation water can also cause dispersion and destruction of the soil structure if the sodium content is at least three times that of calcium. Under such conditions, it can become extremely difficult to meet the crop's water requirements. The risk of salinity is determined from the absorbable sodium value: "Sodium Absorption Ratio" (S.A.R). For the same conductivity, the risk is greater as the S.A.R. is higher (Al-Hadithi et al., 2019).

Examination of the diagram of the SAR (Fig. 6), from the USSL method shows that the danger of alkalization is low but the danger of salinity is high. In detail, (most of the samples are in S1-C3 class), Figure (6) indicates that the water is not suitable to irrigate crops under normal conditions and can be used if the cultivated species have a good tolerance to salinity and the soil is particularly well drained. The evolution of the salinity must however be controlled.

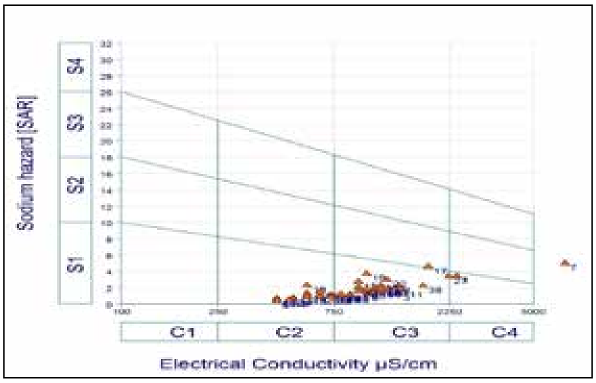

Figure 6. Classification of irrigation water quality. concerning salinity hazards and sodium hazards.

8. Conclusions

The present study is conducted to evaluate the hydrochemical properties of groundwater in the semi-arid region of F'kirina Plain. Most of the groundwater samples are acceptable (permissible limits) for the irrigational and drinking purpose recommended by the WHO standard.

The hydrochemical classification of water from the Piper diagram showed that the water falls into three types of facies. Which are the Ca-HCO_3. Ca-SO_4 and Ca-Cl water types. The spatial distribution maps of groundwater quality parameters showed that the water is moderate to highly mineralized as conductivity is generally high and oscillates between 320 µS/cm and 6500 µS/cm. The low values of mineralization are located near the limestone massifs, and the strong values are observed in the North East part and especially near the Garaet.

Nitrate distribution remains moderate and does not exceed the set established by the World Health Organization (WHO) standards. However, there are certain areas where the concentration of nitrate is higher than 50 mg/L. These variations and distributions depend mainly on the type of irrigation: The low values were observed in places where drip irrigation is used, while high concentrations were measured in areas using gravity irrigation. The application of water quality in this study has been found useful in assessing the overall quality of water. It is also helpful for the public to understand that water quality is a useful tool in many ways in the field of water quality management.

References

Al-Bassam, A. M., and Al-Rumikhani, Y. A. (2003). Integrated hydrochemical method of water quality assessment for irrigation in arid areas: application to the Jilh aquifer, Saudi Arabia. Journal of African Earth Sciences, 36(4), 345–356.

Al-Hadidhi, M., Hasan, K., Algburi, A., and Al-Paruany, K. (2019). Groundwater quality assessment using water quality index and GIS in Baghdad, Iraq. Jordan Journal of Earth and Environmental sciences, 10 (1), 15-20

Al-Paruany, K.B. (2018). Creating a drinking water quality index (WQI) map using the geographic information system (GIS) technique for Karbala city, Iraq. Jordan Journal of Earth and Environmental sciences, 9 (3), 153-166

ANRH (2012). Agence National des Resources Hydrique Canstantine.

Baali, F. (2007) Contribution à l'étude hydrogéologique, hydrochimique et Vulnérabilité d'un système aquifère karstique en zone semi-aride. Cas du plateau de Chéria, N.E.Algérien. Thèse de Doctorat, Université d'Annaba, Algérie 152 p.

El-Naqa, A., and Al Adas, A.A. (2019). Development of Irrigation Water Quality Index for Wadi Araba Basin, Southern Jordan. Jordan Journal of Earth and Environmental sciences, 10 (2), 118-126

Ghodbane, M., Boudoukha, A., and Benaabidate, L. (2016). Hydrochemical and statistical characterization of groundwater in the Chemora area, Northeastern Algeria. Desalination and Water Treatment, 57(32), 14858–14868.

Gouaidia, L. (2008). Influence de la lithologie et des conditions climatiques sur la variation des paramètres physico-chimiques des eaux d'une nappe en zone semi-aride. Cas de la nappe de Meskiana. Nord-Est Algérien. Thèse de Doctorat, Université d'Annaba, Algérie, 199p

Haycock, N., and Burt, T. (1990). Handling excess nitrates. Nature, 348(6299), 291.

Helena, B., Pardo, R., Vega, M., Barrado, E., Fernandez, J. M., and Fernandez, L. (2000). Temporal evolution of groundwater composition in an alluvial aquifer (Pisuerga River, Spain) by principal component analysis. Water Research, 34(3), 807–816.

Hem, J. D. (1985). Study and interpretation of the chemical characteristics of natural water (Vol. 2254). Department of the Interior, US Geological Survey.

Joarder, M. A. M., Raihan, F., Alam, J. B., and Hasanuzzaman, S. (2008). Regression analysis of groundwater quality data of Sunamganj District, Bangladesh.

Khan, A., Umar, R., and Khan, H. H. (2015). Hydrochemical characterization of groundwater in lower Kali watershed, Western Uttar Pradesh. Journal of the Geological Society of India, 86(2), 195–210.

Loizidou, M., and Kapetanios, E. G. (1993). Effect of leachate from landfills on underground water quality. Science of the Total Environment, 128(1), 69–81.

Nishanthiny, S. C., Thushyanthy, M., Barathithasan, T., and Saravanan, S. (2010). Irrigation water quality based on hydrochemical analysis, Jaffna, Sri Lanka.

Okogbue, C.0., and Ukpai, S.N. (2013). Geochemical evaluation of groundwater quality in Abakaliki area, Southeast Nigeria . Jordan Journal of Earth and Environmental sciences, 5 (1), 1-8

Piper, A. M. (1944). A graphic procedure in the geochemical interpretation of water analyses. Eos, Transactions American Geophysical Union, 25(6), 914–928.

Ravikumar, P., and Somashekar, R. K. (2013). A geochemical assessment of coastal groundwater quality in the Varahi river basin, Udupi District, Karnataka State, India. Arabian Journal of Geosciences, 6(6), 1855–1870.

Salimaa, D., and Belgacemb, H. (2017). The hydrochemical characterization of the upper plains aquifers: case of the plain of F'kirina Ain-Beïda, Northeastern Algeria. Desalination and Water Treatment, 92, 90–97.

Sarath Prasanth, S. V, Magesh, N. S., Jitheshlal, K. V, Chandrasekar, N., and Gangadhar, K. (2012). Evaluation of groundwater quality and its suitability for drinking and agricultural use in the coastal stretch of Alappuzha District, Kerala, India. Applied Water Science, 2(3), 165–175.

Sarikhani, R., Ghassemi Dehnavi, A., Ahmadnejad, Z., and Kalantari, N. (2015). Hydrochemical characteristics and groundwater quality assessment in Bushehr Province, SW Iran. Environmental Earth Sciences, 74(7), 6265–6281.

Stumm, W., and Morgan, J. J. (2012). Aquatic chemistry: chemical equilibria and rates in natural waters. John Wiley and Sons.

Subyani, A. M., and Al Ahmadi, M. E. (2010). Multivariate statistical analysis of groundwater quality in Wadi Ranyah, Saudi Arabia. JAKU Earth Sci, 21(2), 29–46.

Todd, D. K., and Mays, L. W. (2004). Groundwater hydrology. John Wiley and Sons.

WHO, G. (1984). Guidelines for drinking-water quality. v. 1: Recommendations.-v. 2: Health criteria and other supporting information. v3: Drinking-water quality control in small-community supplies.

WHO, 2017. World health statistics 2017. Monitoring health for the SDGs, sustainable development goals. Geneva: World Health Organization; 2017. License: CC BY-NC-SA 3.0 IGO.

Wilcox, Lv. (1955). Classification and use of irrigation waters (Issue 969). US Department of Agriculture.

JJEES

JJEES (2023) 14 (3): 210-216
ISSN 1995-6681

Jordan Journal of Earth and Environmental Sciences

IoT Enabled Model for Improving Responses of Water, Sanitation, and Hygiene Programs to Urgent Community Needs During COVID-19

Zeyad Alshboul[1], Mohammad Malkawi [2], Kamel Alzboon[3*]

1 Faculty of Engineering, Civil Engineering Department, Ajloun National University, Jordan
2 Faculty of Engineering, Jordan University of Science and Technology, Jordan,
3 Faculty of Engineering, Al-Balqa Applied University, Jordan

Received 10th October 2022; Accepted 1st May 2023

Abstract

Communities worldwide have suffered from the COVID-19 pandemic in terms of services provided that meet their daily needs and encounter challenges associated with problems in food and hygiene supply chains. Many initiatives have responded to vulnerable communities' essential needs during the pandemic for instance delivering basic hygiene and food packages. These initiatives came as a response to rapid need assessment to prevent the transmission of COVID-19 and provide basic needs for children and women and people with special needs. However, there have been several problems and drawbacks in service-providing mechanisms resulting in significant delays in delivery time, errors in targeting, uncertainty in the selection, and factors impacting the response programs in general. This study aims to identify the right categories of people and their urgent needs as well as the efficient distribution mechanisms during lockdowns to accelerate the response plans and meet the urgent needs of targeted groups during emergencies. We have developed a Community Needs Response Model integrated with IoT concepts to reduce errors, delays, and incomplete response plans and strategies. The model has shown its ability to help governments, NGOs, and other involved agencies in needs assessment and response programs by remotely identifying urgent needs, beneficiaries, and people info including geo-location, delivery time, and improving complaints and feedback mechanisms. The results showed an improvement in the selection mechanisms through a multi-layer filter, which enables response plans to prioritize responses based on vulnerability or needs. However, further improvements are needed to integrate the model with national emergency response platforms.

Keywords: *WASH, Community Need, Response Plans, COVID-19, IoT*

1. Introduction

COVID-19 has impacted all services and business sectors within countries in the world starting from small to large businesses(Bartik et al. 2020, Shrestha et al. 2020). Further impacts of COVID-19 included the management of social and daily services presented by local utilities for the communities like water supply and social financial support for vulnerable people (Balamurugan et al. 2021, Renukappa, Kamunda and Suresh 2021, Abu-Bakar, Williams and Hallett 2021, Al Gharaibeh 2020, Ashcroft et al. 2021, Sharif 2021, Sura Al-Harahsheh et al. 2020). This has been caused by lockdowns adopted by governments to prevent virus outbreaks that impacted personal practices in terms of hygienic practices, water consumption, and social interactions (Donde et al. 2021, Lalander et al. 2013, Dwipayanti, Lubis and Harjana 2021, Long et al. 2022, Calbi et al. 2021, Kim and Florack 2021, Campos et al. 2021, Abu-Bakar et al. 2021, Alshboul, Al-Zboon and Alzoubi 2022). During the lockdowns, people were having fear disruptions in their essential needs supply chain like food and protective materials(Aday and Aday 2020, Boudesseul et al. 2021). Despite COVID-19 was not the first pandemic and the realization of the importance of protective materials in limiting virus spread, lessons learned seem to have been limited(Sawada et al. 2017). However, demands on personal protective equipment and hygienic materials exceeded the supply rate of these materials during lockdowns resulting in inflation in prices. This led to a shortage of materials available in the market and difficulties in obtaining them (Best and Williams 2021). This shortage in personal protective and hygienic materials was also observed during the SARS outbreak, 2003 revealing the importance of providing essential needs during emergencies(Eyre, Hick and Thorne 2016). Protective materials and any other essential needs might not be accessible and available for vulnerable people during emergencies. This will increase risk factors for children, young people, women, and the elderly in low-income communities(Patel et al. 2020).

Since the first confirmed case of COVID-19 in Jordan, on 2nd March 2020, there are 1.7 M cases up to date with a death rate of 0.08% based on global statistics provided by WHO in April 2022(Alshboul et al. 2022). Therefore, Jordan has responded to the COVID-19 outbreak and implemented various control measures to mitigate the pandemic's impact on public health(Al-Tammemi 2020). The responses were operated and managed by a central and multi-disciplinary governmental team launched by the National Center for

* Corresponding author e-mail: kalzboon@yahoo.com

Security and Crises Management. All procedures followed the best evidence-based recommendations for implementation and were continuously updated and announced to the public through many communication channels including national e-platforms and social media. Strict measures were implemented banning all social gatherings of more than 10 persons, traveling among cities, social distancing, hygienic practices, and prevention measures, and also included strict rules during lockdowns such as closing all commercial centers on the 20th March 2020 and continued for 3 months(Al-Tammemi 2020). Governmental procedures and restrictions on communities' activities and movements were effective as there were reductions in individual mobility, retail and recreation centers, and numbers of employment at their workplaces in comparison to the baseline (April 2020) and to the recent updates as most of the restrictions are relaxed (Suleiman et al. 2020, Health , Health). Strengthening the cooperative linkage between government and society is essential to improve crisis management during emergencies and minimize the impacts of strict procedures to mitigate the pandemic impact. Such linkages will improve awareness and communication processes and direct technical and financial support to the right groups. This support includes community needs to combat COVID-19 spread such as protective materials or essential needs for individuals during curfews and lockdowns.

Governments and NGOs worldwide provided communities with essential food and hygiene kits for people in need as a response to economic and pandemic emergencies. Many countries have offered protective materials and hygiene kits to the public during pandemics as a part of social support and to encourage communities to practice infection-prevention behaviors(Song and Yoo 2020). Some of the recommendations specified contents in kits that should be sufficient to meet households' needs for one month of use and include mouth care tools(D'Mello-Guyett et al. 2020). However, the selection of hygiene items may vary according to the provider and typically consists of personal hygiene care tools. This variation in hygiene kit distribution is based on the nature that the distribution process is a complex intervention that interacts with several components as its impact varies among different beneficiaries, delivery mechanisms, and timelines (Freeman et al. 2014, Hutton and Chase 2016). Evaluating processes associated with kit distribution is similar to most public health interventions helping to observe the impacts and design intended outcomes(Moore et al. 2015). Such evaluations are essential for any other future contexts and conditions as well as modifying process implementation (Murdoch 2016, Bonell et al. 2006). To date, there have been no studies improving distribution mechanisms and selecting the contents of hygiene kits during lockdowns as has occurred during the COVID-19 pandemic.

In Jordan, there have been several responses to the community's need for protective materials for vulnerable people to control the COVID-19 outbreak and curfew conditions. These responses were implemented to deliver protective and hygienic materials to vulnerable people and came as a response to rapid need assessment reports. Kits were distributed to people according to pre-selection criteria and the distribution process was performed door-to-door. During project implementation conducted by NGOs and international agencies, there have been many challenges in delivering services and selecting beneficiaries. The pre-selected criteria may have ignored families in need due to a lack of information, inadequate budget, miscommunication, and uncertainties associated with available data. Further challenges were associated with distribution mechanisms and tracking systems as well as drawbacks in complaints and feedback channels. During the investigation of the processes associated with delivering protective and hygienic materials, there have been many suggestions for improving and establishing e-services and automated mechanisms that organize all processes and project details. The improvements should include developing a comprehensive and effective selection process to meet all community needs and priorities.

We developed a mechanism through which the quantity and types of items in hygiene kits can be selected based on community needs and the policy of providers. This mechanism provides stakeholders with communication channels during emergencies and lockdowns to analyze complaints and feedback data to increase response time. This mechanism sought to improve the delivery process by suggesting an e-tracking system and delivery best practices to speed, accurate, and direct processes, and financial and asset management. The study came up with recommendations to optimize future and similar public health interventions. This study evaluated the effectiveness of hygiene kit distribution during COVID-19 lockdowns in Jordan and discussed drawbacks and opportunities for improvements. Gap analysis has been performed to assess the selection process for the beneficiary and if the process of distributing the kits achieved its intended outcomes. The evaluation process included the feasibility and possibility of using e-services in future similar contexts with suggestions of major pillars of the e-service platform.

Quality assurance and quality control have been implemented during all stages of the study. This will outline procedures for handling the main activities of the study such as i) how samples were selected for QA/QC check, ii) availability of records, performed analysis, mitigation and corrective actions taken, and subsequent modifications done to the processes, ii) service interruptions how communicated with the public.

2. Research Significance

Responses to the community's needs during emergencies are subject to delay and incomplete processes and inefficient selection and delivery mechanisms. Most of the needs assessment mechanisms are performed manually through voluntary processes, which are mostly more expensive and time-consuming. This study is improving a Community Needs Response Model integrated with its concepts to reduce costs associated with identifying beneficiaries and essentials. This model will accelerate the delivery rate and improve communications between all stockholders e.g. Local NGOs, representatives, delivery service providers, and monitoring agencies.

3. Methodology and Approaches

In this study, processes associated with projects aimed at delivering hygiene kits to vulnerable people have been investigated as these projects aimed at preventing transmission of COVID-19 and reflect on the performance of COVID-19-related responses under the water sanitation and hygiene program in general. One of the implemented projects in many municipalities in Jordan has been selected, and the project came as a response to a rapid need assessment report carried out in May 2020 and was implemented in 2020. The study addressed the most essential considerations that can be used as a model in any future e-services during emergencies. However, the project has been designed to distribute more than three thousand hygiene kits to about two thousand households alongside information cards for awareness purposes. Sixteen items were packed in each distributed kit and were selected based on the community's needs for protection purposes and sanitization. Previous experiences implemented by service utilities have been reviewed to develop a recommended action in parallel with focused group discussions (FGDs) performed in the municipalities. We have prepared learning questions for addressing the outcomes achieved and adoption as well as the whole distribution process during project implementation. Key Informative Interviews (KII) with representative persons were also performed to ensure that the implemented project achieved the intended outcomes and that the main assumptions made during the design phase remained valid during the actual response. The selection criteria for beneficiaries and registration processes have been discussed during FGDs and KII until we have identified targeted groups, feedback, and complaint mechanisms. Quality, adequacy, and preferences have been discussed and linked with awareness of the targeted community. The study dealt with various discussions such as improving the registration techniques for receiving services, the possibility of adopting reusable or recyclable items, and the possibility of creating self-employment opportunities.

The study included two FGDs and each of FGD event had two split groups, the first two groups consisted of 19 persons split into a 10-women group and a 9-men group. The second two groups consisted of 17 persons distributed among 10 women group and 8 men group. The groups were a mix of Jordanian and Syrian participants as the selected areas hosted refugees from Syria and each FGD was designed for 1 hour. The 4 FGDs are designed to ensure that the project reaches the right group of people, selection criterion validity, efficient coverage, and suitable timeliness of the response. Key informant interviews have been performed with 2 persons from 2 Community-Based Organizations to verify whether the project achieved the intended outcomes and whether the main assumptions made during the project designation remained valid during the actual responses. The interviews have been performed with the host community project managers in both areas. The interviews were essential to formulate key lessons and whether the project has minimized the negative effects of COVID-19. The study checked for any change in the original plan and corresponding causes and evaluated the feedback and complaints handling mechanism. The study assesses any improvement made by the project. It has addressed the beneficiaries' feedback and compliments. Furthermore, we checked the efficiency and reliability criteria in selecting beneficiaries and the role of IoT usage in response plans during emergencies. Alternatives that can be used instead of a direct hygiene kit distribution have been evaluated by directing questions to all beneficiaries and involved stakeholders.

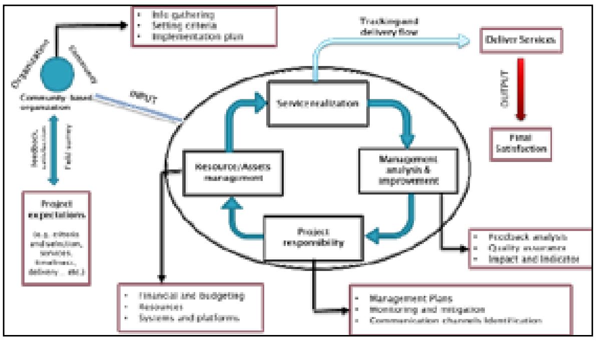

Figure 1. Different stages of the system are used to assess the processes for continuous service improvement and learning securing. The obtained expectations and needs from the benefited people during all feedback mechanisms and data collection methods, are entered as inputs to a direct Community-based organizations-community-organization channel to create a database, sitting criteria, and implementation plan. The information is entered through a coordinator to the project lead and cycled to the resource management and logistics, service realization, and goes to analysis for further action by the project lead. The process cycle ends with satisfaction and outcomes achievement.

4. Results and Discussion

4.1 Outcome achievement and adoption

The project of delivering essential needs during COVID-19 to vulnerable people including hygiene kits has been designed to access vulnerable people directly to provide them with hygiene kits during COVID-19 based on pre-selection criteria. The project has mostly achieved its designed outcomes as the estimated percentage of vulnerable people who received items formed from 70% to 85%. The FGDs indicated that the covered group of people by the services have matched the intended outcomes. Investigating the impact of distributed hygiene items on the rate of spreading the pandemic was a suggestion to improve the outcomes of water, sanitation, and hygiene programs by establishing pre-defined indicators for tracking the spreading rate of COVID-19.

The majority of people involved in the KIIs expected to benefit from the implemented water, sanitation, and hygiene Projects, although there was no pre-knowledge about the details of implementation. There has been a recommended action to improve processes of delivering assistance or delivering needs to communities during emergencies to establish a mechanism able to announce processes to all beneficiaries to inform them about the desired outcomes of the projects. In addition, the project could have been designed to provide psychological support; for instance, the vulnerable should not have felt that he/she was not left alone during the pandemic and there was external support to them to cope with emergencies. Continuous support during this critical time should have been provided to enhance the confidence level of water, sanitation and hygiene programs to support the vulnerable. There have been many changes in the assumptions made during project implementations. These changes have affected the cost associated with packing, distribution, ordering items, and problems with the supply chain. For instance, projects have assumed that the distribution process will be implemented by external suppliers with packaging items but this assumption has been changed. The unexpected cost associated with the distribution process requested by the external service provider has changed the assumption made before the distribution. Delays during ordering kits and time loss have been noticed because of the coordination process with external service suppliers. Changes in processes and timelines revealed the importance of establishing a communication platform where data are regularly updated and processes can be tracked online and in real-time.

4.2 Benifitied people and timelines

Response believed that about 80% of vulnerable people received the services during the emergency and indicated that the percentage may increase to cover the whole vulnerable. These can be performed by providing the services of the same budget by providing only essential items and lowering the number/count of items in kits to cover a large group of people. Some of the families were excluded because of low budget, inaccurate address, high-income value or not selected by accident. The selection process excluded registered people from the selection due to a) residency situation as families are living in the same place, b) not being reached during the contact time c) because of social ethics as they can afford items or they see that many people are much more in need. Further causes are identified by about 40% of responses that there were families not selected even if they were in need because of the low family members, unemployed people, orphans, and divorced women. The criteria of services are unknown for the serviced people and the responses indicated that these criteria and response stages and timelines may be improved and announced in dynamic mechanisms by using e-services.

The majority of beneficiaries have not encountered any challenges during the services, but still the minority had a few challenges associated with the distribution process for instance no exact delivery time, inaccurate locations of targeted people, and service speed Around 60% of surveyed entities have not observed an excluded group from the registration/distribution, while 41% of the group think the information provided and the selection criteria are unknown. The selection criteria should have been discussed with the beneficiaries and announced during the registration process. In a few cases, some people have received a call that they will receive a kit but they never did. Such cases need to be verified based on the database of the originating project. During the FGDs events, there was a major recommendation to use the most public places to announce the project, as well as use social media. We believe that a digital platform, with an appropriate user interface could have solved many of the challenges faced during the project implementation.

There were suggestions to minimize the implementation time of the door-to-door mechanisms through subgrouping beneficiaries or center-based distribution mechanisms. These suggestions were not compatible with the lockdown rules associated with COVID-19. Many families had to carry their kits for long distances which was costly and not practical action for the most. All responses were satisfied with the implementing time and Some of these suggested that the responses were shortly before the lockdown period of the pandemic. This suggestion referred to their urgent needs for the items during the lockdown due to the limited availability and cost considerations. Most of the responses revealed the important items provided in boosting the virus spread and these responses were satisfied with assistance time and they believed that items came at the right time. 84% of the benefited people assure that the distribution was done within the designed period for the distribution and the rest have noticed the delay in the delivery time. The importance of using automated and e-mechanisms in delivery services is in urgent need. Sich e-mechanisms may identify benefited people before any distribution process with a clear geographic-based delivery plan.

4.3 Targeting and multi-layer selection filter

All responses revealed that there was no idea about the selection criteria used for identifying and prioritizing beneficiaries. Furthermore, the community has not been involved in setting the selection criteria and most respondents show the importance of selecting services based on the community's feedback to maximize the benefits. The interviewed people thought that the distribution has been performed based on the number of family members or income rate. These criteria have shown many drawbacks due to the complexities associated with social and economic situations. For instance, some families have higher income rates but it is eroded due to rents, health care, loans…etc. There was a consensus that field visits or communications with beneficiaries before any further distribution is essential to investigate if families meet eligibility as many beneficiaries theoretically met the selection criteria but were not vulnerable as they have other income sources. Community-based organizations have been advised to improve the selection process and they are required to participate in determining beneficiaries and setting selection criteria. This has also been shown during assessment reports where participating with the community for setting the selection criteria seems to be essential as the people can know the category group that they belong to. The respondents and focused groups have denoted that the single layer selection filter was not efficient as many partially vulnerable were discarded from the response plans although their needs for specific needs have been approved. The single-layer selection filter applies criteria to all individuals and families and discarded groups if they do not meet the criteria or for financial causes. However, the respondents have recommended adopting weigh-criteria mechanisms where groups are classified based on their need magnitude for each type of provided item. This mechanism will maximize the benefited groups and accelerate the distribution processes

Disabled people and people suffering from chronic diseases (Heart diseases, Diabetes, high Blood pressure, Spine diseases… etc..), loans, number of family members who are still in school or university have to be covered in the selection criteria as well as people live in rented houses or tents may include for further consideration as a minor indicator. Family net income may have been considered instead of total income as many families have high-income rates but with high rates of expenses. The FGDs emphasize the importance of discussing the social status of the selected vulnerable with Community-based organizations or representative people from the society before the distribution and setting of selection criteria. Each category of the selection criteria has a specific weight based on the type of the project and intended outcome. The weight should be in cooperation with the community and associated community-based organizations with more focus on the vulnerability to the pandemic rather than vulnerability itself in this project for example. The filter used in selecting beneficiaries can be either a selection filter "single-layer" (benefited, non-benefited) or a classification filter "multi-layer" (classify people based on their needs and importance). The multi-layer filter is a selection mechanism that can classify input data (candidates, community, targeted groups, or beneficiaries) into different categories based on their needs and/or priorities. Each category has its criteria that all people who meet these criteria will be sorted and the rest will pass to further layer for filtration. The selection criteria in each layer are either designed based on expectations, satisfaction, or project outcomes or based on criteria weight (e.g. the first layer for people who owned their houses, the second for rented houses, and the third for tents. Note that each layer may have multiple different criteria or the same criteria with different weights). The rejected people at the end process are people who are out of the project scope. The filtration using a multi-layer selection mechanism will guarantee that the budget reaches the maximum group of people and beneficiaries will have treated equity. Single-layer filtration is s selection mechanism that sorts input data based on their weight of importance and the number of beneficiaries is selected based on the available budget. The rest will have been excluded from the service as the input data were treated equally (Fig.2).

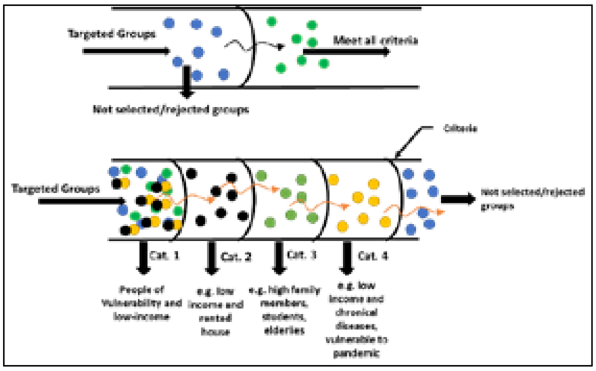

Figure 2. Comparison between two different selection mechanisms i) selection/single-layer filter (up) and ii) multi-layer filter (down). The single-layer filter applies all criteria to all candidates on an equality basis and rejects samples according to priority/weight and the rejected candidates. The selection mechanism and criteria-based filtration on up classifies targeted groups based on their needs and importance. The multi-layer selection filter has multi-filtration steps that can categorize beneficiaries based on their significant needs and the rest is passed to the next for further classification of less priority. This filter will not exclude eligible people due to the budget limitation rather than distribute resources on an equity basis and the rejected people are those who are out of the project scope.

The distribution mechanism was in person at their residencies during the response implementation at the study area, and all respondents were satisfied with this mechanism. This mechanism needs further improvements like mapping beneficiaries' locations to accelerate the process and gather detailed information about the most urgent needs based on the weights. Many complaints have been recorded during the distribution such as delivery time, duplications, and delivery loss due to the availability. However, a communication channel between the community and the delivery team has not existed and most of the respondents have indicated the importance of employing IoT concepts in creating communication channels and delivery tracking during emergencies.

4.4 Targeted groups and vulnerability

Most of the beneficiaries were satisfied with services provided during the pandemic and items are well-instructed for usage purposes. There were suggestions for improving electronic services specifically the number of provided items, user's manual, rejection, replacement, and feedback portal. The study revealed the importance of creating portals for user's profiles to update users with upcoming activities and services. The services extend to allow users to determine the number of items in each provided kit based on use rates. Furthermore, focused groups have emerged on the importance of using sustainable materials for extending lifetime instead of single-use items, for instance, washable masks. There has been a significant role in capacity building of manufacturing the provided items during emergencies in self-employment and its sustainability contribution. There has been significant approval by the respondents regarding the significant role of these capacity building particularly the use of recyclable sanitizers and face masks

Samples selected by previous reports indicated the existence of a large portion of the benefited people about information provided with the provided items or during e-channels. Distributed instructions and information have not existed in a minor ratio of about 30% and this information has consisted of detailed and helpful instructions in an understandable, visible, and feasible manner. However, the majority revealed that items in the kits were enough to help people disinfect a) tools and furniture, b) home facilities, c) adding young and children, and d) permanent sterilization. There was a consensus that the community did not receive any awareness or clarification on how the provided items in the kits can help to confront and prevent the spreading of COVID-19. There have been recommended actions provided by targeted groups including increasing the awareness level about the pandemic and the awareness campaign may be more direct with detailed explanations to boost the efficiency of responses during emergencies. IoT can be used as a tool for performing these processes with feedback service for identifying the response quality.

Responses indicated that the feedback mechanisms may be identified in an obvious manner and the provided contact numbers were not sufficient. All of the FGDs emphasize that hotlines, social media, and community-based organizations are excellent alternatives or e-services for feedback and complaints. Results indicated that are familiar with using social media and mobile services and don't have a problem dealing with future services through any other e-portals. online systems. Further studies are needed to explore the portion of people who need training in using e-portals and other technologies in delivering services during emergencies.

Studying the level of skills in smart technologies and associated apps is essential for improving strategies in providing emergency response plans and improving services. Such studies will improve mechanisms in involving different stakeholders in processes and services provided to the communities during emergencies such as communications, delivery, and access to vulnerable people. Responses revealed that people have not experienced the existing communication channels during the pandemic and have not performed or needed feedback on their satisfaction. The information regarding any response plans during emergencies needs to be identified and informed to the communities as the responses were not aware of the existence of responses without pre-identified mechanisms. The distribution process has been announced for people who are involved or registered by community-based organizations or social utilities or through field inspection during the distribution.

5. Conclusion

There has been an urgent need to improve the response plans to the communities' needs during emergencies. The improving processes should include the delivery and selection process as well as communication channels between providers and targeted groups. Field inspection should be part of the selection process and chronic diseases may have a high weight in the selection. Update/customize the selection criteria based on the type of project and objectives, and the weight of each criterion should be justified based on the project outcomes and expectations (Perhaps according to the area, and degree of spread of COVID-19) as well as feedback from Community-based organizations. Contemplate the sustainability of the kit. Using sustainable items, such as washable items, make hand sanitizers in their home to lower the budget and establish self-support. Examining efficiency & and effectiveness through contemplating the value for money; would increase the amount of money per kit and highly increase the benefit. Establishing an online system for implementing similar services in the future. The system should be able to link the organization, community-based organizations, and community to interchange information and enhance the community and Community-based organizations' engagement in setting criteria, needs, and distribution. The system has to provide an online registration system, awareness channel, key information, feedback/ complaints option, delivery track service, and geographical database.

Acknowledgments

The authors would like to express great gratitude to the Ajloun National University for support, funding, and cooperation throughout the project duration.

Conflict of interest: The authors declare no conflict of interest

Funding: This study was supported by Ajloun National University.

Authors' Contribution: The authors have equally contributed and improved the manuscript. All authors reviewed and agreed to publish the final version of the manuscript.

References

Abu-Bakar, H., L. Williams & S. H. Hallett (2021) Quantifying the impact of the COVID-19 lockdown on household water consumption patterns in England. npj Clean Water, 4, 13.

Aday, S. & M. S. Aday (2020) Impact of COVID-19 on the food supply chain. Food Quality and Safety, 4, 167-180.

Al-Tammemi, A. a. B. (2020) The Battle Against COVID-19 in Jordan: An Early Overview of the Jordanian Experience. Frontiers in Public Health, 8.

Al Gharaibeh, F. (2020) The response of Jordanian society and social workers to the COVID-19 crisis. International Social Work, 63, 811-814.

Alshboul, Z. A., K. Al-Zboon & A. A. Alzoubi (2022) Temporary and Permanent Impacts of COVID-19 on Water Consumption Patterns and Solid Waste Generation. 2022, 10.

Ashcroft, R., D. Sur, A. Greenblatt & P. Donahue (2021) The Impact of the COVID-19 Pandemic on Social Workers at the Frontline: A Survey of Canadian Social Workers. The British Journal of Social Work, 52, 1724-1746.

Balamurugan, M., K. S. Kasiviswanathan, I. Ilampooranan & B.-S. Soundharajan (2021) COVID-19 Lockdown Disruptions on Water Resources, Wastewater, and Agriculture in India. Frontiers in Water, 3.

Bartik, A. W., M. Bertrand, Z. Cullen, E. L. Glaeser, M. Luca & C. Stanton (2020) The impact of COVID-19 on small business outcomes and expectations. Proceedings of the National Academy of Sciences, 117, 17656-17666.

Best, S. & S. J. Williams (2021) What Have We Learnt About the Sourcing of Personal Protective Equipment During Pandemics? Leadership and Management in Healthcare Supply Chain Management: A Scoping Review. Frontiers in Public Health, 9.

Bonell, C., A. Oakley, J. Hargreaves, V. Strange & R. Rees (2006) Assessment of generalisability in trials of health interventions: suggested framework and systematic review. Bmj, 333, 346-9.

Boudesseul, J., O. Zerhouni, A. Harbert & C. Rubinos (2021) Keeping Meta-Analyses Hygienic During the COVID-19 Pandemic. Frontiers in Public Health, 9.

Calbi, M., N. Langiulli, F. Ferroni, M. Montalti, A. Kolesnikov, V. Gallese & M. A. Umiltà (2021) The consequences of COVID-19 on social interactions: an online study on face covering. Scientific Reports, 11, 2601.

Campos, M. A. S., S. L. Carvalho, S. K. Melo, G. B. F. R. Gonçalves, J. R. dos Santos, R. L. Barros, U. T. M. A. Morgado, E. da Silva Lopes & R. P. Abreu Reis (2021) Impact of the COVID-19 pandemic on water consumption behaviour. Water Supply.

D'Mello-Guyett, L., K. Greenland, S. Bonneville, R. D'hondt, M. Mashako, A. Gorski, D. Verheyen, R. Van den Bergh, P. Maes, F. Checchi & O. Cumming (2020) Distribution of hygiene kits during a cholera outbreak in Kasaï-Oriental, Democratic Republic of Congo: a process evaluation. Conflict and Health, 14, 51.

Donde, O. O., E. Atoni, A. W. Muia & P. T. Yillia (2021) COVID-19 pandemic: Water, sanitation and hygiene (WASH) as a critical control measure remains a major challenge in low-income countries. Water Research, 191, 116793.

Dwipayanti, N. M. U., D. S. Lubis & N. P. A. Harjana (2021) Public Perception and Hand Hygiene Behavior During COVID-19 Pandemic in Indonesia. Frontiers in Public Health, 9.

Eyre, A. J., J. L. Hick & C. D. Thorne (2016) Personal Protective Equipment. Ciottone's Disaster Medicine, 294-301.

Freeman, M. C., M. E. Stocks, O. Cumming, A. Jeandron, J. P. T. Higgins, J. Wolf, A. Prüss-Ustün, S. Bonjour, P. R. Hunter, L. Fewtrell & V. Curtis (2014) Systematic review: Hygiene and health: systematic review of handwashing practices worldwide and update of health effects. Tropical Medicine & International Health, 19, 906-916.

Health, G. COVID-19 Community Mobility Report Jordan. (2020) Available online at: https://www.gstatic.com/covid19/mobility/2020-04-11_JO_Mobility_Report_en.pdf. (accessed April 18, 2020).

--- COVID-19 Community Mobility Report Jordan. (2020) Available online at: https://www.gstatic.com/covid19/mobility/2022-04-30_JO_Mobility_Report_en.pdf (accessed May 4, 2022).

Hutton, G. & C. Chase (2016) The Knowledge Base for Achieving the Sustainable Development Goal Targets on Water Supply, Sanitation and Hygiene. Int J Environ Res Public Health, 13.

Kim, H. & A. Florack (2021) When Social Interaction Backfires: Frequent Social Interaction During the COVID-19 Pandemic Is Associated With Decreased Well-Being and Higher Panic Buying. Frontiers in Psychology, 12.

Lalander, C., S. Dalahmeh, H. Jönsson & B. Vinnerås (2013) Hygienic quality of artificial greywater subjected to aerobic treatment: a comparison of three filter media at increasing organic loading rates. Environmental Technology, 34, 2657-2662.

Long, E., S. Patterson, K. Maxwell, C. Blake, R. Bosó Pérez, R. Lewis, M. McCann, J. Riddell, K. Skivington, R. Wilson-Lowe & K. R. Mitchell (2022) COVID-19 pandemic and its impact on social relationships and health. Journal of Epidemiology and Community Health, 76, 128.

Moore, G. F., S. Audrey, M. Barker, L. Bond, C. Bonell, W. Hardeman, L. Moore, A. O'Cathain, T. Tinati, D. Wight & J. Baird (2015) Process evaluation of complex interventions: Medical Research Council guidance. BMJ : British Medical Journal, 350, h1258.

Murdoch, J. (2016) Process evaluation for complex interventions in health services research: analysing context, text trajectories and disruptions. BMC Health Serv Res, 16, 407.

Patel, J. A., F. B. H. Nielsen, A. A. Badiani, S. Assi, V. A. Unadkat, B. Patel, R. Ravindrane & H. Wardle (2020) Poverty, inequality and COVID-19: the forgotten vulnerable. Public health, 183, 110-111.

Renukappa, S., A. Kamunda & S. Suresh (2021) Impact of COVID-19 on water sector projects and practices. Utilities policy, 70, 101194-101194.

Sawada, S. I., K. Kuklane, K. Wakatsuki & H. Morikawa (2017) New development of research on personal protective equipment (PPE) for occupational safety and health. Ind Health, 55, 471-472.

Sharif, O. A.-Q. a. M. A. (2021) Water Audits of Academic Institutions in Water Stressed Countries; the Case of the Jordan University. Jordan Journal of Earth and Environmental Sciences (JJEES), 13, 54-59.

Shrestha, N., M. Y. Shad, O. Ulvi, M. H. Khan, A. Karamehic-Muratovic, U.-S. D. T. Nguyen, M. Baghbanzadeh, R. Wardrup, N. Aghamohammadi, D. Cervantes, K. M. Nahiduzzaman, R. A. Zaki & U. Haque (2020) The impact of COVID-19 on globalization. One Health, 11, 100180.

Song, E. & H. J. Yoo (2020) Impact of Social Support and Social Trust on Public Viral Risk Response: A COVID-19 Survey Study. International Journal of Environmental Research and Public Health, 17, 6589.

Suleiman, A., I. Bsisu, H. Guzu, A. Santarisi, M. Alsatari, A. Abbad, A. Jaber, T. a. Harb, A. Abuhejleh, N. Nadi, A. Aloweidi & M. Almustafa (2020) Preparedness of Frontline Doctors in Jordan Healthcare Facilities to COVID-19 Outbreak. International Journal of Environmental Research and Public Health, 17, 3181.

Sura Al-Harahsheh, Ahmed A. Al-Taani, Hani Al-Amoush, Akram Shdeifat, Atef Al-Mashagbah, Marwan Al-Raggad, Raya Al- Omoush, Hassan Al-Kazalah, Maher Hraishat, Refaat Bani-Khalaf & K. Almasaeid (2020) Assessing the Impact of Zaatari Syrian Refugee Campin Central North Jordan on the Groundwater Quality. Jordan Journal of Earth and Environmental Sciences (JJEES), 11, 260-271.

JJEES

JJEES (2023) 14 (3): 217-221
ISSN 1995-6681

Jordan Journal of Earth and Environmental Sciences

The Effect of Hydrothermal Curing on the Efflorescence of Micro/ Nanometric Size Jordanian Aluminosilicate Inorganic Polymers

Islam Aldabsheh[1*], Maite Garcia-Valles[2], Salvador Martinez[2]

[1]Dpt. of Applied Earth and Environmental Sciences, Faculty of Earth and Environmental Sciences, Al Al-Bayt University, Al-Mafraq, Jordan
[2]Dpt. Mineralogia, Petrologia i Geologia Aplicada, Facultat de Ciències de la Terra, Universitat de Barcelona, c/Martí i Franquès, s/n, 08028 Barcelona, Spain

Received 30th November 2022; Accepted 6th May 2023

Abstract

This study investigates the possibility of reducing the efflorescence (excess or non-reactive salts) effect of inorganic polymers based on aluminosilicate materials from Jordan. This was achieved by minimizing the particle size of the raw materials, and using hydrothermal curing at 80º C, 120º C and 150º C, then comparing the results with other different curing conditions; ambient and humid. Kaolinite (K), volcanic tuff (Vt), and silica sand (Ss) raw materials were used. The raw materials were ground to the average particle sizes (d_{50}) of: <10µm, <200nm, and <100nm. Three different mixing ratios of Vt, K, and Ss were used to study their dissolution behavior and to prepare inorganic polymers. X-ray diffraction (XRD), X-ray fluorescence (XRF), and inductively coupled plasma (ICP) techniques were used to identify the mineralogical and chemical composition of the raw and processed materials. The samples of <10µm were successful to be molded and analyzed for compressive strength. The average compressive strength was about 65 Mpa under hydrothermal condition cured at 150ºC. The samples of nanometric size failed because the material in this range of size behaves and exhibits one or more nanoscale phenomena. Qualitative and quantitative measurements of efflorescence formation were also determined. The average alkali leaching was reduced from 3.14% of ambient cured samples to 0.83% of hydrothermally cured ones. This highest strength result indicates that the alkaline solution has reacted with the majority of Al^{3+} and Si^{4+} of silicates raw material.

Keywords: *Inorganic polymers; Hydrothermal curing; Compressive strength, Efflorescence*

1. Introduction

Inorganic polymers technology has been the focus of several studies for two decades and has shown potential to transform the building products industry (Cong and Cheng, 2021; Aliques-Granero et al., 2019; Al-Slaty, 2018; Lahoti et al., 2018; Lemougna et al., 2014; Duxson et al., 2007; Rowels and O'Connor, 2003; Van Jaarsveld et al., 2002; Davidovits, 1994). Some works were carried out by a Geo-Materials Research Project at the University of Jordan, which represents an international scientific collaboration between the University of Jordan, and Vrije Universiteit Brussel, to support the project entitled "Chemical Stabilization of Natural Geomaterials for Construction and Industrial Applications". The goal from this project was to produce low cost construction materials for green housing (Aldabsheh et al., 2015; Esaifan et al., 2015 and 2016; Slaty et. al., 2015; Slaty et al., 2013; Alshaaer, 2013; Rahier et al., 2011a, 2011b; Aldabsheh, 2011; Slaty, 2010). In terms of costs, the inorganic polymers-based building material has similar cost to the replaced material, in addition to their greater environmental benefits. They are characterized by a comparable compressive strength, chemical stability, and hardness. However, during the production of such material, less energy is used and fewer greenhouse gases are released. For example, for every one ton of manufactured cement, one ton of carbon dioxide is produced (Krausmann et al., 2009; Horvath, 2004; Van Oss and Padovani, 2003; Aïtcin, 2000; Ames et al., 1994). Inorganic polymer technology has the potential to reduce emissions by 80 percent since high-Atemperature calcination is not required (Steveson and Crentsil, 2005). Aluminosilicate could be used as raw materials in the geopolymerization process (Rovnaník, 2010).

Efflorescence refers to the deposition of unreacted chemical additives on specimen surfaces after curing. It is difficult to quantify. Most of the standard methods for estimating efflorescence end up with a qualitative description of its extent on the sample. These unreacted chemicals are transported by water through the voids in partially immersed specimen. The soluble material is transported from the immersed zone to the upper dry zone and precipitates at the specimen's surface after evaporation. Overtime, this process causes degradation of the specimen's structure (Al-Slaty, 2018; Esaifan et al., 2015 and 2016; Slaty et al., 2015; Alshaaer, 2013). Efflorescence indicates an incomplete curing reaction. The present work aims on keeping the water in the reaction mixture as long as possible during the curing process to complete the setting reactions. The production of geopolymeric materials is expected to improve the mechanical and chemical properties of the products.

* Corresponding author e-mail: i_aldabsheh@aabu.edu.jo

2. Materials and Methods

Two reactive Jordanian aluminosilicate materials (kaolinite; K, volcanic tuff; Vt) and filler material (silica sand, Ss) from Jordan were used. Kaolinite belongs to Ordovician-Silurian Hiswa Deposit, 280-300 km south of Amman. A volcanic tuff sample was taken from Pleistocene Harrat Ash-Shaam, Tell Hassan NE-Jordan (between Azraq and Safawi area). The silica sand sample was collected from the Late Cambrian-Early Ordovician Disi Sandstone Formation, Ram Group SW-Jordan (70 km north of Aqaba) (Barjous, 1995; Ala'li, 2001 and 2004).

A sequential X-ray spectrometer Phillips PW2400 housed at Faculty of Earth Sciences, University of Barcelona was used to determine the chemical composition of raw materials. X-ray diffraction (XRD) analysis was used to identify the crystalline phases of the representative portions of the raw material as well as the activated samples by using Bragg-Brentano PANAnalytical X'Pert Diffractometer system (Cu Kα1 radiation, using 45 kV and 40 mA).

Starting raw materials are ground using different ball mills to the average particle sizes (d_{50}) of: <10μm, <200nm, and <100nm. The particle size distribution was measured by Beckman Coulter LS230 Laser Diffraction Particle Size Analyzer and Laser Particle ANALYSETTE 22 Nano Tec plus for micro and nano-sized particles, respectively.

To determine the optimal ratio in terms of the leached Al and Si, the dissolution properties of the dry binder made from three mixed raw materials in different ratios; (100:75:25), (100:50:50) and (100:25:75) of (K:Vt:Ss) were studied. This was accomplished by mixing 5g of starting raw materials with 200 ml of 10M NaOH solution for 168 h. The liquid portion was collected by centrifuging at 10000 rpm for 10 min, and the extent of leaching Al^{3+} and Si^{4+} was measured using inductively coupled plasma optical emission spectroscopy (ICP-OES)

Three raw materials, alkali solution (NaOH) and reaction media (H_2O) were used for the fabrication of the inorganic polymers specimens. Sodium hydroxide (NaOH (98 %)) was used as an alkali activator. Three mixing ratios are used to fabricate inorganic polymers pastes and molds as shown in Table (1). The dimensions of the used mold are 3cm*0.5cm*5cm.

Table 1. Mixing ratios of the prepared inorganic polymers.

Ratio	Kaolin	Volcanic tuff	Silica sand	NaOH	H_2O
R1	100	75	25	16	22
R2	100	50	50	16	22
R3	100	25	75	16	22

Compressive strength and efflorescence formation of inorganic polymer samples were examined after curing under different conditions (ambient, humid, hydrothermal at (80ºC, 120ºC and 150ºC)). Quantitative (extent of alkali leaching) and qualitative measurements were used to describe the efflorescence effect.

Mechanical tests were performed using a universal testing machine tension-compression-fatigue model MTS Bionix 358 (MTS, USA). A 25kN load cell equipped with a PC connection and a software package Test Star II model control. 1mm/sec is used. Most of the standard methods for estimating efflorescence (extent of alkali leaching) end up with a qualitative description of its extent. In this study, a simple "percentage coverage" quantitative method was used to estimate any efflorescence. It was calculated by measuring the weight of empty can before and after drying.

3. Results and Discussion

The chemical and mineralogical composition are illustrated in Table (2). XRF results show that SiO_2 and Al_2O_3 are the main components of kaolinite and volcanic tuff raw materials; SiO_2 content represents s about 51.38% and 45.85% respectively. SiO_2 is the only oxide in the silica sand sample (99.13%). Al_2O_3 content is 25.68 % in kaolinite and is about 14.23% in volcanic tuff.

The X-ray diffractogram of an unreacted sample of representative kaolinite sample confirmed the presence of kaolinite and quartz. The identified minerals in kaolinite sample are the same that obtained by Awwad et al. (2009). Muscovite and hematite are present as traces. The volcanic tuff sample consists essentially of plagioclase and diopside. Forsterite is also detected. The identified minerals in volcanic tuff sample are the same that obtained by Sarireh et al. (2021). The main dominant mineral in the silica sand sample is quartz.

Table 2. Mineralogical and chemical composition of raw material (Aldabsheh et al., 2018) and activated inorganic polymers.

Identified minerals (using XRD)			Chemical composition (XRF)	
Raw material		Activated Inorganic polymers	SiO_2%	Al_2O_3%
Kaolinite	Kaolinite, quartz, muscovite, hematite	Thermonatrite, natrite, sodalite, Na-Al-silicate hydrates phases (SAS)	51.38	25.68
Volcanic tuff	Plagioclase, diopside, forsterite		45.85	14.23
Silica sand	Quartz		99.13	-

The particle size distributions of the three raw materials are illustrated in Figure (1a) for d_{50}<10μm and Figure (1b) for d_{50} 100-200 nm.

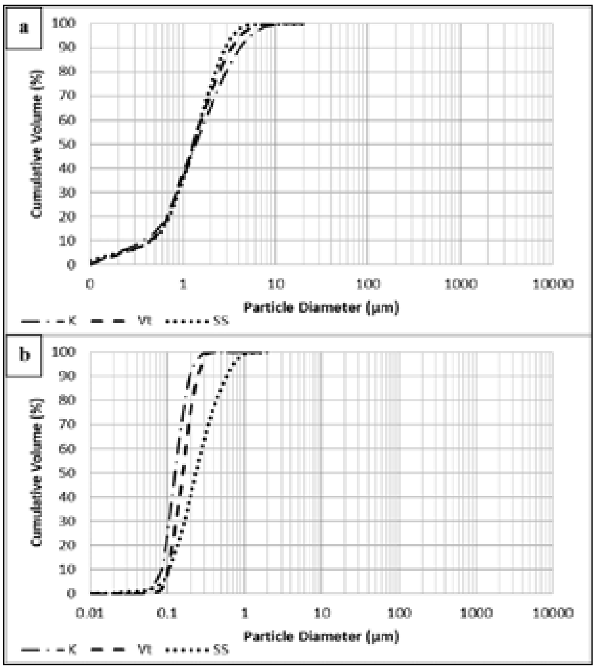

Figure 1. The particle size distributions of kaolinite (K), volcanic tuff (Vt), and silica sand (Ss). a: d_{50}<10 µm, b: d_{50}100-200 nm.

Figure (2) shows the leached Al^{3+} and Si^{4+} (w/w %) of treated mixed materials at different ratios with different particle sizes in 10 M NaOH for 168 h. In general, the leaching of Si^{4+} and Al^{3+} has significantly increased when particle size has decreased to less than 100 nm. This is because smaller particle sizes have stronger electrostatic attractive forces and a larger surface area, which can speed up a reaction (Ginebra et al., 2004). This finding consistent with the results obtained from a previous study done by Aldabsheh et. al. (2018) that investigated the dissolution of each raw material alone. As shown in Figures (2a and b), R3 of (100:25:75) of (K:Vt:Ss) is the best mixing ratio in terms of leached Si^{4+} (51.79%) and Al^{4+} (86.28%) for the particle size <100nm

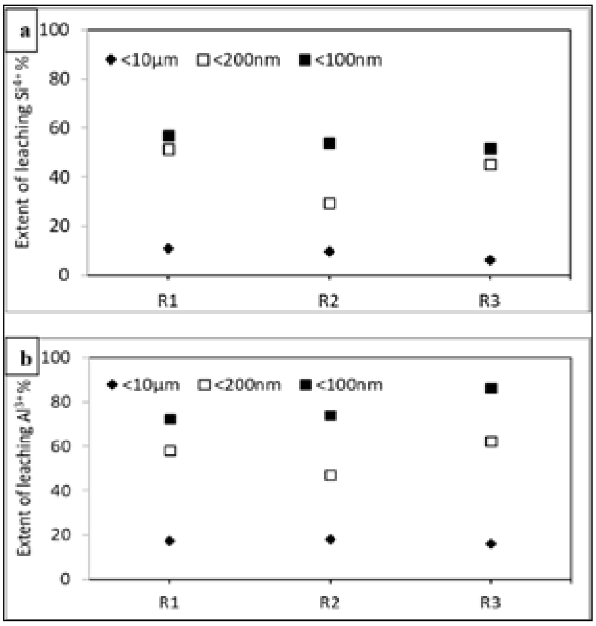

Figure 2. Extent of leached Si^{4+} and Al^{4+} (w/w %) of three-mixed dry binder of raw materials at different ratios. a: Si^{4+}, b: Al^{3+}. R: ratio.

Mineralogical characterization by XRD of solid residues of activated inorganic polymer confirms the formation of new sodium-aluminum-silicate hydrates phases (SAS), thermonatrite, natrite and sodalite because of alkaline activation of the raw materials (Figure 3).

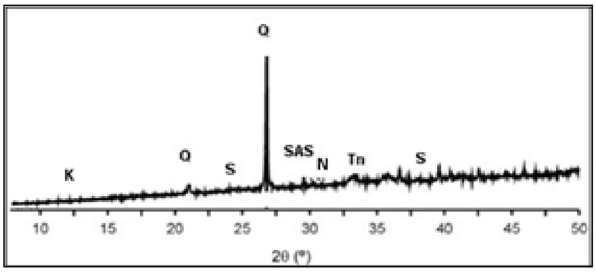

Figure 3. The XRD spectrum of the activated inorganic polymer specimens. (Q: Quartz, K: Kaolinite, S: Sodalite, SAS: Na-Al-silicate hydrate phases, Tn: Thermonatrite, N: Natrite).

The samples less than 10 µm were successful in molding and measuring their mechanical strength and efflorescence. The samples smaller than 200 nm and 100 nm fail because the material behaves and demonstrates one or more nanoscale phenomena/properties in this size range.

The compressive strength values (MPa) of samples (d_{50}<10 µm) prepared from the three ratios (R1, R2, and R3), cured at ambient (Figure 4a) and humid conditions (Figure 4b) are plotted vs. extent of alkali leaching (%). The Highest compressive strength (37.0 MPa) under ambient conditions is for samples prepared by using mixing ratio R2 of (100:50:50) of (K:Vt:Ss) (Figure 4b). In addition, these samples have the lowest efflorescence (3.14%), suggesting that the alkaline solution reacted with most the Al^{3+} and Si^{4+} in the samples. A compressive strength of 32 MPa is obtained from a previous study of the same raw material (kaolinite and silica sand) for a mixture cured at 80 °C for 24 h (Slaty et al., 2010). The authors did not use volcanic tuff in preparing the inorganic polymer samples. The particle size of the starting powder raw material had a particle size distribution between 90 and 250µm.

The results plotted in Figure (4b) indicate that under the humid conditions; the samples with highest compressive strength- (26.19 MPa) have the lowest efflorescence (4.59%)

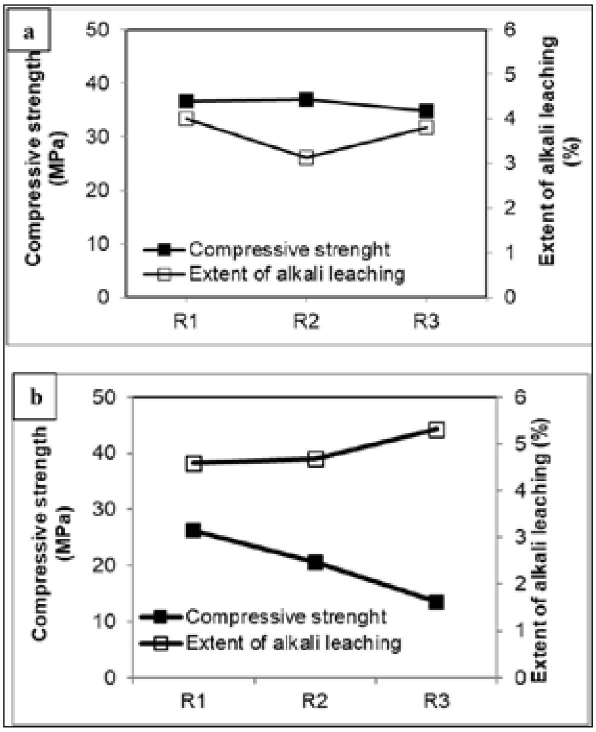

Figure 4. Compressive strength and extent of alkali leaching of samples cured at (a) ambient, (b) humid. R: ratio.

The average compressive strength of samples prepared by using R2 and cured under hydrothermal conditions at 80ºC, 120ºC and 150ºC are 52.1, 59.5, 65.2MPa, respectively are shown in Figure (5). A significant aspect here is keeping the water inside the materials to enable the reaction process to continue. The extent of alkali leaching measurements matches with the compressive strength values. The measurements decrease with the increase of compressive strength values. A low quantity of efflorescent material is observed on the sample surfaces represented by a thin layer of efflorescent material covering an external surface of inorganic polymer specimens (Figure 6). No signs of change in length or weight are noted in the hand specimens and no erosion and cracks are observed (Figure 6).

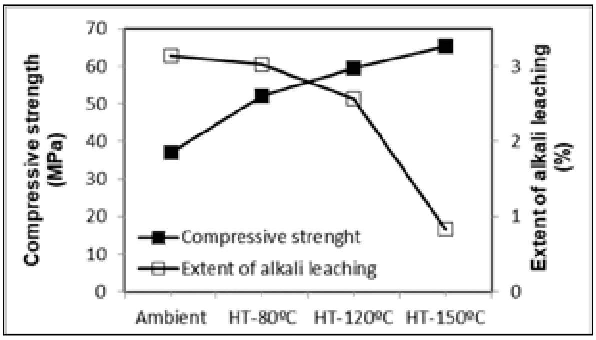

Figure 5. Compressive strength and extent of alkali leaching of samples cured under hydrothermal (HT) conditions at 80˚C, 120˚C and 150˚C.

Figure 6. Extent of alkali leaching (efflorescence) observed in the samples.

4. Conclusions

The ability to produce reliable inorganic polymers binder is achieved with enhanced properties by minimizing the particle size, adding a suitable amount of volcanic tuff, or by using different curing conditions to drive the alkaline reaction with more Al^{3+} and Si^{4+} from the aluminosilicate phases. The results also confirm the effectiveness of reducing particle size and using hydrothermal curing on the extent of leaching (efflorescence effect). Samples of nanometric particle size (<200nm, and <100nm) failed to exhibit one or more nanoscale phenomena/property.

Acknowledgment

The authors would like to thank the Consolidate Group 2017 SGR 1687 and the Erasmus Mundus (AVEMPACE II) Post Doc Mobility Scholarship for supporting this work. The authors further acknowledge the technical assistance provided by the Centres Científics i Tecnològics de la Universitat de Barcelona (CCiTUB) staff.

References

Aïtcin, P. (2000). Cements of yesterday and today concrete of tomorrow. Cement and Concrete Research 30: 1349-1359.

Ala'li, J. (2001). Evaluation and beneficiation of silica sand and kaolinitic sandstone in south of Jordan, PhD Dissertation, University of Nottingham, U.K.

Aldabsheh, I. (2011). Dissolution of Jordanian raw materials in alkaline solutions and their stabilization for construction purposes, PhD Dissertation. The University of Jordan

Aldabsheh, I., Khoury, H., Wastiels, J., Rahier, H. (2015). Dissolution behavior of Jordanian clay-rich materials in alkaline solutions for alkali activation purpose. Part I. Applied Clay Science 115: 238-247.

Aldabsheh, I., Garcia-Valles, M., Martinez, S. (2018). Interaction of micro/nano-metric size of Jordanian aluminosilicate raw materials with high pH solution. Materials Letters 229: 57-59.

Aliques-Granero, J., Tognonvi, M. T., Tagnit-Hamou, A. (2019). Durability study of AAMs: Sulfate attack resistance. Construction and Building Materials, 229, 117100.

Alshaaer, M. (2013). Two-phase geopolymerization of kaolinite-based geopolymers. Applied Clay Science 86: 162-168.

Al-Slaty, F. (2018). Index Properties of Alkali-Activated Cement Mortar Affected by the Addition of Phosphatic Clay. Jordan Journal of Earth and Environmental Sciences 9(1): 63-66.

Ames, J. Cutcliffe, W., MacFadyen, J. (1994). Cement and cement raw materials. DD Carr (S. ed.), Industrial minerals and rocks, 295-316

Awwad, A. M., Ahmad, R., and Alsyouri, H. (2009). Associated minerals and their influence on the optical properties of Jordanian kaolin. Jordan Journal of Earth and Environmental Sciences, 2(1), 66-71.

Barjous, M. (1995). Mineralogy and processing of industrial minerals from Jordan, PhD Dissertation, University of Wales, Cardiff-U.K.

Cong, P., and Cheng, Y. (2021). Advances in geopolymer materials: A comprehensive review. Journal of Traffic and Transportation Engineering (English Edition) 8(3): 283-314.

Davidovits, J. (1994). Geopolymers, Inorganic polymeric new materials. Journal of Materials Education 16: 91-139.

Esaifan, M., Rahier, H., Barhoum, A., Khoury, H., Hourani, M., Wastiels, J., (2015). Development

of inorganic polymer by alkali-activation of untrated kaolinitic clay: reaction stoichiometry, strength and dimensional stability. Construction and Building Materials 91: 251–259.

Esaifan, M., Khoury, H., Aldabsheh, I., Rahier, H., Hourani, M., and Wastiels, J. (2016). Hydrated lime/potassium carbonate as alkaline activating mixture to produce kaolinitic clay based inorganic polymer. Applied Clay Science 126: 278-286.

Duxson, P., Fernández-Jiménez, A., Provis, J. L., Lukey, G. C., Palomo, A., van Deventer, J. S. (2007). Geopolymer technology: the current state of the art. Journal of Materials Science 42: 2917-2933.

Ginebra, M. P., Driessens, F. C. M., Planell, J. A. (2004). Effect of the particle size on the micro and nanostructural features of a calcium phosphate cement: a kinetic analysis. Biomaterials 25(17): 3453-3462.

Horvath, A. (2004). Construction materials and the environment. Annual Review of Environment and Resources 29: 181-204.

Krausmann, F. Gingrich, S. Eisenmenger, N. Erb, K. Haberl, H., Kowalski, M. (2009). Growth in global materials use, GDP and population during the 20th century. Ecological Economics, 68: 2696-2705.

Lahoti, M., Wong, K. K., Tan, K. H., Yang, E. H. (2018). Effect of alkali cation type on strength endurance of fly ash geopolymers subject to high temperature exposure. Materials and Design 154: 8-19.

Lemougna, P. N., Melo, U. C., Delplancke, M. P., Rahier, H. (2014). Influence of the chemical and mineralogical composition on the reactivity of volcanic ashes during alkali activation. Ceramics international 40(1): 811-820.

Rahier, H., Esaifan, M., Wastiels, J., Slatyi, F., Aldabsheh, I., Khoury, H. (2011a). Alkali activation of kaolinite for production of bricks and tiles. In Proceedings of the 4th International Conference, Non-Traditional Cement and Concrete Conference (NTCC), Brno, Czech Republic, pp. 19-22.

Rahier, H., Slaty, F., Aldabsheh, I., Alshaaer, M., Khoury, H., Esaifan, M., Wastiels, J. (2011b). Use of local raw materials for construction purposes. Advances in Science and Technology 69: 152–155.

Rovnaník, P. (2010). Effect of curing temperature on the development of hard structure of metakaolin-based geopolymer. Construction and Building Materials 24(7): 1176-1183.

Rowels, M., and O'Connor, B., (2003). Chemical optimization of the compressive strength of aluminosilicate geopolymers synthesized by sodium silicate activation of metakaolinite. Journal of Materials Chemistry 13: 1161–1165.

Sarireh, M., Ghrair, A. M., Alsaqoor, S., Alahmer, A. (2021). Evaluation of the Use of Volcanic Tuff in concrete block production. Jordan Journal of Earth and Environmental Sciences 12 (4): 275-284

Slaty, F. (2010). Durability of geopolymers product from Jordanian Hiswa clay, PhD Dissertation, The University of Jordan.

Slaty, F., Khoury, H., Wastiels, J., Rahier, H., (2013). Characterization of alkali activated kaolinitic

clay. Applied Clay Science 75: 120-125.

Slaty, F., Khoury, H., Wastiels, Rahier, H., (2015). Durability of alkali activated cement produced from kaolinitic clay. Applied Clay Science 104: 229-237.

Steveson, M. and Sagoe-Crentsil, K.K. (2005). Relationships between composition, structure and strength of inorganic polymers: Part 2 - Fly Ash-Derived Inorganic Polymers, Journal of Materials Science 16: 4247-4259

Van Jaarsveld, J. G. S., Van Deventer, J. S., Lukey, G. C. (2002). The effect of composition and temperature on the properties of fly ash-and kaolinite-based geopolymers. Chemical Engineering Journal 89(1-3): 63-73.

Van Oss, H., and Padovani, A. (2003). Cement manufacture and the environment Part II, Environmental challenges and opportunities. Journal of Industrial Ecology 7(1): 93- 126

JJEES

JJEES (2023) 14 (3): 222-231
ISSN 1995-6681

Jordan Journal of Earth and Environmental Sciences

Transportation, Accumulation and Pollution by Lost Raw Phosphate Dust Particles from a Phosphate Loading Berth in Coastal Water of the Gulf of Aqaba-Red Sea

Rawajfh, M. M.[1], Rasheed, M. Y.[*2], Al-Rousan, S. A.[3], Manasrah, R. S.[4], Abu-Hilal A.H.[1]

[a] *Department of Earth and Environmental Science, Faculty of Science, Yarmouk University, Irbid 21163, Jordan*
[b] *School of Science, Department of Chemistry, University of Jordan, Amman,11942 Amman, Jordan*
[c] *School of Science, Department of Geology, University of Jordan, Amman,11942 Amman, Jordan*
[d] *Department of Coastal Environment, Faculty of Marine Sciences, The University of Jordan-Aqaba Branch, Jordan*

Received 23th March 2022; Accepted 10th May 2023

Abstract

The present study was carried out to investigate the accumulation pattern, magnitude and distribution of the phosphate rock dust particles that reach the coastal seawater of the Jordanian Gulf of Aqaba during ship-loading at the Phosphate Loading Berth (PLB). The concentration of phosphate- phosphorus was measured in water, sediment and trap-sediments. The speed and direction of currents in the area of the PLB were also measured to assess its effect on the transportation, sedimentation and distributions of phosphate dust particles within the study area. The analysis and examination of the results indicate that phosphate pollution is located mainly near the phosphate loading berth. The results show that the concentrations of phosphorus (total phosphorus (TP), inorganic (IP), and organic (OP) in trap-sediments were higher than their concentrations in sediments and IP was the major species of phosphorus in the study area. The statistical analysis showed that TP, IP, OP in trap-sediments and sediments of PLB differ significantly from those of all other sites. The concentration of TP, IP and OP were higher in the power station north (PSN) and central power station (PS) located to the south of PLB compared to the concentrations at stations located to the north of PLB and thus reflecting the effect of prevailing southward current. The increase in dissolved inorganic phosphorus (DIP) concentration in the water of the PLB area is not high to cause significant increase in the DIP in the water of the Gulf of Aqaba to abnormal or hazardous levels.

Keywords: *Phosphate, Pollution, Gulf of Aqaba, Sediments, Trap-sediments, Prevailing currents*

1. Introduction

Jordan has the fifth largest reserve and the second largest exporter of phosphate in the world (Jordan Phosphate Mines Company, 2020). The phosphate port in Aqaba is used for exporting phosphate powder. Phosphate dust generated during storage and loading is considered an important environmental problem in Aqaba because of the substantial quantities of the phosphate that is lost and settled to the water of the Gulf of Aqaba during the loading process (Abed, 2012; Abu-Hilal, 1999).

The concentrations of dissolved inorganic phosphate in the coastal water of the Gulf of Aqaba range between 0.02 to 0.2 μM (Rasheed et al., 2018). Phosphate-phosphorous and other nutrients concentration in the sediment pore water is higher than those in the water overlying these sediments, which under very calm condition resulted in fluxes of 0.1 and 0.01 μmol m^{-2} d^{-1} for dissolved inorganic nitrogen (DIN) and dissolved inorganic phosphorus (DIP), respectively (Al-Rousan, 1998; Rasheed et al., 2002; Al-Rousan et al., 2004). The bottom sediments of the Jordanian coast water contain 0.07 % total phosphorous and the phosphate concentration in the interstitial water is about 50 times higher than those of the overlying water (Al-Rousan, 1998; Al-Rousan et al., 2004). Other estimate for the total phosphorous concentration in the bottom sediments is in the range of 0.04 to 0.25% was recorded (Al-Rousan et al. 2006; MSS Report 2020). However, values up to 50 folds was recorded in sediments from the Phosphate Loading Terminal (Badran and Al Zibdeh, 2005; MSS Report, 2020). It has been reported that some of the raw phosphate (flouroapatite) does dissolve in the sea- water and therefore it contributes to the level of the inorganic phosphate nutrient in the ecosystem [10] (Abu-Hilal et al., 2008). It has been reported that phosphate levels in PLB area is nearly three to four times higher than that of the water in the adjacent areas (Abu-Hilal, 1985).

The environmental effects of the phosphate dust include increasing of suspended solids and water turbidity, reduction of water clarity and light penetration, and siltation on the coral reef and depression of coral growth. Other potential impact includes increasing the levels of dissolved phosphate nutrients and other toxic heavy metal such as Cd, As, and Zn (Abu-Hilal, 1999; Al-Rousan et al., 2016).

The physical characteristics of sea water of the Gulf of Aqaba that may affect phosphate dust distribution, abundance and dissolution in the environment of the Gulf of Aqaba have been investigated, particularly the effect of

* Corresponding author e-mail: m.rasheed@ju.edu.jo

the prevailing currents and the distance from the phosphate loading berth which has been considered the main source of sedimentary phosphorus in the Jordanian (northeastern) sector of the Gulf of Aqaba.

The main goal of the present study was to investigate the accumulation rate, magnitude and distribution of the phosphate rock dust particles that reach the coastal seawater of the Jordanian Gulf of Aqaba during ship loading at the Phosphate Loading Berth (PLB), which is located on the most northeastern side of the Gulf of Aqaba. The results of this work would help decision makers to estimate the necessity to remove the accumulated phosphate dust when rehabilitation is needed for the old phosphate Port area.

2. Materials and Methods

2.1 Study sites

The present study was carried out in the north and northeastern coasts (Fig. 1). The sampling sites covered the sector from the Hotel Area (HA) in the north to the Marine Science Station (MSS) in the south. Water, sediment, and trap-sediment samples were collected four times during the study period. Sample processing and pretreatment were carried out immediately after collection.

2.2 Sampling process

Water samples were collected from near surface and near bottom levels, then sorted in pre–labelled acid washed polyethylene bottles of one litre (1 L) capacity. Immediately after collection the bottles were put in an ice box and transported to the laboratories of Marine Science Station. Water samples were sorted in a deep Freezer at -20 ^{O}C until future analysis. The sediment and trap-sediment samples were collected at different depths from eleven selected sites (Fig. 1). Settling sediments particles were collected using bottom sediment traps that were placed 1m above sea bottom. Each trap was made of two cylindrical jars. Each jar was 9.9 cm in diameter, and 30 cm in height. The sedimentation jars were collected at regular time intervals of about four weeks and replaced again for another stage collection. Sedimentation rates were determined using sedimentation traps. The near-bottom water, sediment and trap-sediment samples were collected by SCUBA divers. Sediment samples from the top 5 cm of surface sediment were collected in pre-cleaned acid washed plastic bags from each site at the same time of traps collection.

2.3 Current measurements

Acoustic Doppler Current Profiler (ADCP) Workhorse 300 kHz (RD Instruments) was deployed at the seabed (35 m depth) of a shelf area in close vicinity of the Phosphate Loading Berth (PLB). Horizontal and vertical current components were measured. The time interval between ensembles was 10 minutes and the number of pings per ensemble was 300 at each 2-m bin length.

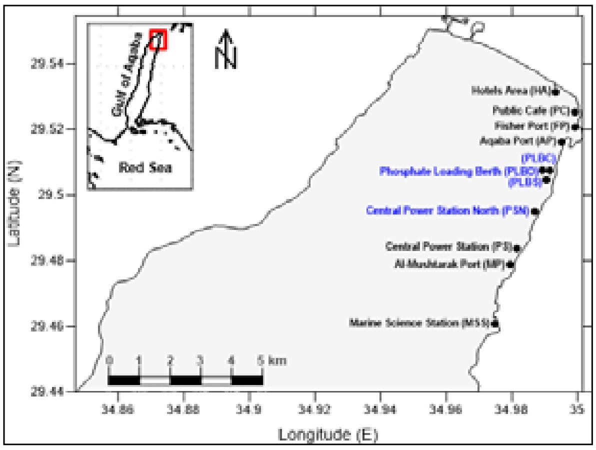

Figure 1. Map of the study area showing the locations of the sampling sites.

2.4 Laboratory work

The single solution method of Murphy and Riley (1962) for the determination of DIP in sea water as described by Grasshoff et al. (1999) with minor modification was used in the present work.

Aliquot of 0.1 g of the sediments was treated with concentrated HNO_3 and evaporated to near dryness. The residue was digested with 4 ml of concentrated $HClO_4$ until the white fumes of $HClO_4$ were not observed (APHA, 1971). The digested samples were dissolved in 2 ml of 6 M HCl and 10 ml of deionized water and filtered into a100 ml polypropylene volumetric flask through Whatman filter paper No 1. Filtrate in the flask was made up to 100 ml with deionized water. Aliquot of the digest was used for the determination of total phosphorus, as dissolved inorganic phosphorus (DIP) using the same method of determination of DIP in water.

Inorganic phosphorus (IP) was determined by the addition of 25 ml of 1 M HCl to an aliquot of 0.1 g of trap-sediment sample in a Teflon beaker. The samples were kept at room temperature for 24 hours. The samples were filtered through pre-weighed, pre-ignited 24 mm GF/C Whatman glass fibre filter into a 100 ml polypropylene vlometric flask. The filtrate in the flask was completed to the 100 ml mark by the addition distilled water. Inorganic phosphorus was determined as DIP using the same method of determination of DIP in water. Organic phosphorus was determined by the difference between total phosphorus (TP) and inorganic phosphorus (IP) of each sample (Aspila et al., 1976). Sediment samples were washed with deionized water and dried at 80 ^{O}C for at least 36 hours. The dried samples were physically freed from visible shells and coarse shell fragment. Samples were ground, powdered and homogenized by the use of an agate pestle and mortar. Phosphorus species (TP, IP, OP) were analysed by the use of the same methods that have been described under the trap-sediment samples. Total sedimentation rate was measured following the method of English et al . (1994).

In order to test the significance in differences between the different concentrations of phosphorus species at different sites of the study area, the "one-way ANOVA test" has been used to calculate the P-values while, significance has been tested using 95% confidence interval.

3. Results and discussions

3.1 Dissolved inorganic (reactive) phosphorus (DIP) in the water of the Gulf of Aqaba

The results of DIP in surface (Sw) and near-bottom (Bw) water from the eleven sites (Fig. 2a) show that the highest concentration was recorded at PLBS whereas the lowest was at HA in the north. DIP concentrations show a general increase in winter (November and January). It is obvious that the concentrations of DIP are slightly higher around PLB and tend to decrease with increasing distance from this site.

The statistical analysis for DIP in the surface and near-bottom water showed significant differences between the sites adjacent to the Phosphate Loading Berth (phosphate loading berth center (PLBC); phosphate loading berth offshore (PLBO); and phosphate loading berth south (PLBS) and the other seven sites (Aqaba port (AP); Fisher port (FP); Hotels Area (HA); Al-Mushtarak Port (MP); Marine Science Station (MSS); Central Power Station north (PSN); and Public cafés (PC)). In contrast, the differences between the three adjacent sites which are close to the Phosphate Loading Berth (PLB) were not significant. The slight increase in DIP concentration in the close vicinity of this area can be attributed to the dissolution of the lost raw phosphate particles in the water of this site (Hulings and Abu-Hilal, 1984; Al-Moghrabi and Horani, 1998). The available evidence indicate that the increase of DIP due to the partial dissolution of the raw phosphate reaching the water of the Gulf of Aqaba would not cause a substantial or significant increase in the prevailing levels of DIP in water (Abu-Hilal et al., 2008; Rasheed et al., 2005; Rasheed et al.2018).

3.2 Total phosphorus

The results of TP in the trap-sediment and sediments from the eleven sites (Fig. 2b) show that the highest concentration was obtained from the sediment traps which are located at the PLBS while the highest concentration in sediment was measured at PLBC. The lowest concentration was obtained from the trap- sediment and sediment which are located at the Hotel Area in the north and at Marine Science Station in the south. The concentrations of TP are higher around the Phosphate Loading Berth with TP concentrations are relatively high in the stations located to the south of PLB (PSN and PS) compared to the concentrations at stations located to the north of PLB (AP, PC and HA). The concentrations of TP and IP in the trap-sediments are higher than the concentrations in the sediments. The statistical analysis of the results for TP in trap-sediments showed significant differences between the sites located within the PLB area and other sites, while the differences between the sites located within the PLB were not significant. The statistical analysis for TP in sediments showed also the same result; significant differences between the three sites which are located within the PLB area and all other sites.

3.3 Inorganic phosphorus

The results (Fig. 2c) show that the highest mean concentrations of IP in the trap-sediments of PLBS, while the highest concentration in sediments was measured at the PLBC. The lowest IP concentrations in both sediment and trap-sediment were recorded at HA in the north. It is clear that the concentrations of IP are higher around the Phosphate Loading Berth and in the stations located to the south compared to those located to the north. The statistical analysis of the IP results in trap-sediments and sediments revealed significant differences between the sites that are located within or close to the PLB and all other sites, while the differences between the sites that are located within the PLB area are not significant.

3.4 Organic Phosphorus

The examination of the results of OP in trap-sediments from the eleven sites (Fig. 2d) shows that the highest concentration was measured at PLBC while the highest concentration in sediments was measured at PLBS while the lowest in trap-sediment and sediment were at MSS. This trend of OP in trap-sediments and sediments is similar to that of TP and IP in sediments and trap-sediments; the relatively higher concentration of all phosphorus species tends to decrease with increasing distance from the PLB area whether to the north or the south. The statistical analysis of OP in sediments and trap-sediments reveals significant difference between the sites that near PLB and all other sites, while the differences between the sites near PLB were not significant.

3.5 Sedimentation Rate

The total sedimentation rate (mg cm^{-2} d^{-1}) in the near-bottom sediment traps (Fig. 2f) was highest at the HA in the north, whereas the lowest was measured at the PLBO. The statistical analysis for the total sedimentation rate in the near-bottom sediment traps showed significant differences between the site of PLBC and the other sites in the south. Significant differences have been also found between the highest sedimentation rates at HA in the north and seven other sites in the south. Significant differences were observed also between the lowest sedimentation rate at PLBO and the sites HA, PLBC, PLBS, AP, FP, and PC. The high sedimentation rate at Hotel Area might be attributed to many factors that include but not restricted to the constructions and infrastructure work that take place in the northern tip of the Gulf. Similar results were also recorded by the MSS (MSS Report, 2020). The higher sedimentation rate at the PLB area is expected to be related to ship loading and due to the high rate of sedimentation from the air borne dust which has been reported at this site (Schuhmacher et al., 1982; Badran and Zibdah, 2005; Al-Rousan et al., 2016). The lowest sedimentation rate was recorded in the PLBO at a distance of about (200 m) to the west of the PLB site. This might be attributed to the depth of sedimentation trap at this site (nearly 20 m) and also due to relatively long distance (200m) between this site and the Phosphate Loading Berth (PLB) site which is receiving most of the lost raw phosphate particle. Al-Rousan (2016) has found that the sedimentation rate is decreasing with increasing depth of the water column due to the limited effect of the currents and waves factors in eroding the subsurface sediments at deep site. The higher sedimentation rates at the sites located within the PLB area are still much lower than the rates reported by other authors (Al-Rousan, 1998; Hamdan, 1999; Bani-Awwad, 2002; MSS report, 2020). These relatively low sedimentation rates (present study) can be attributed to the improved management of phosphate handling during trucks and trains unloading, storage, and ship loading processes that include the use of chalk feeders, better training and environmental awareness of the workers and operators working in the Phosphate Loading Berth sites (MSS Report, 2020).

3.6 Phosphate-phosphorus as phosphorus pentoxide (P_2O_5) and tricalcium phosphate (TCP) in trap-sediments and sediments

The results in table 1 indicate that IP is an important phosphorus species as it constitutes 82.50 - 97.54 % of the TP in trap-sediments, while OP constitutes 2.44 - 17.50 %. TP in the trap-sediments ranged between 0.32 - 23.45% when calculated as P_2O_5 and between 0.70 - 49.28% when calculated as TCP. By comparison, IP ranged between 0.26 - 22.23% when calculated as P_2O_5 and 1.08 - 45.93% when calculated as TCP.

The results of sediments analysis (Table 2) are similar to those of trap-sediments. IP is an important phosphorus species and represents 77.01-94.53 % of the TP concentrations in the sediments, while OP constitutes 5.4 - 23.11 %. The concentrations of TP in the sediments represent 0.16-21.74% as P_2O_5 and 0.34 - 47.50% as TCP, while those of IP represent 0.14-20.55% as P_2O_5 and 0.31-44.90 % as TCP. The higher percentage of TP and IP are caused mainly by the high apatite phosphorus fraction, which usually constitutes a major fraction of the inorganic form of phosphorus (Abu-Hilal, 1987). The concentrations of phosphorus species (TP, IP, and OP) are highest in the sites which are nearest to PLB and the concentrations tend to decrease with increasing distance from this site. The abnormally high concentrations of the total phosphorus at the sites PLBS, PLBC, and PLBO and dramatic decrease in these concentration with increasing distance (to the south and north) indicated that phosphate pollution is concentrated mainly in the close vicinity of the PLB due to the high specific gravity of the raw phosphate particle that, therefore, settle quickly and deposit onto the bottom causing the high sedimentation rate of phosphate dust around Phosphate Loading Berth. The higher concentrations of TP and IP in trap-sediments as compared to their concentrations in sediments can be attributed to the rapid dilution in the sediments and dissipation of the partially dissolved raw phosphate particles in the water of the Aqaba Gulf. Phosphorus as P_2O_5 constitutes 0.32-23.45 %, 0.16-21.74 % of the total phosphorus concentrations in trap-sediments and sediments respectively, compared to the phosphate rock which contain about 32% phosphorus as P_2O_5.

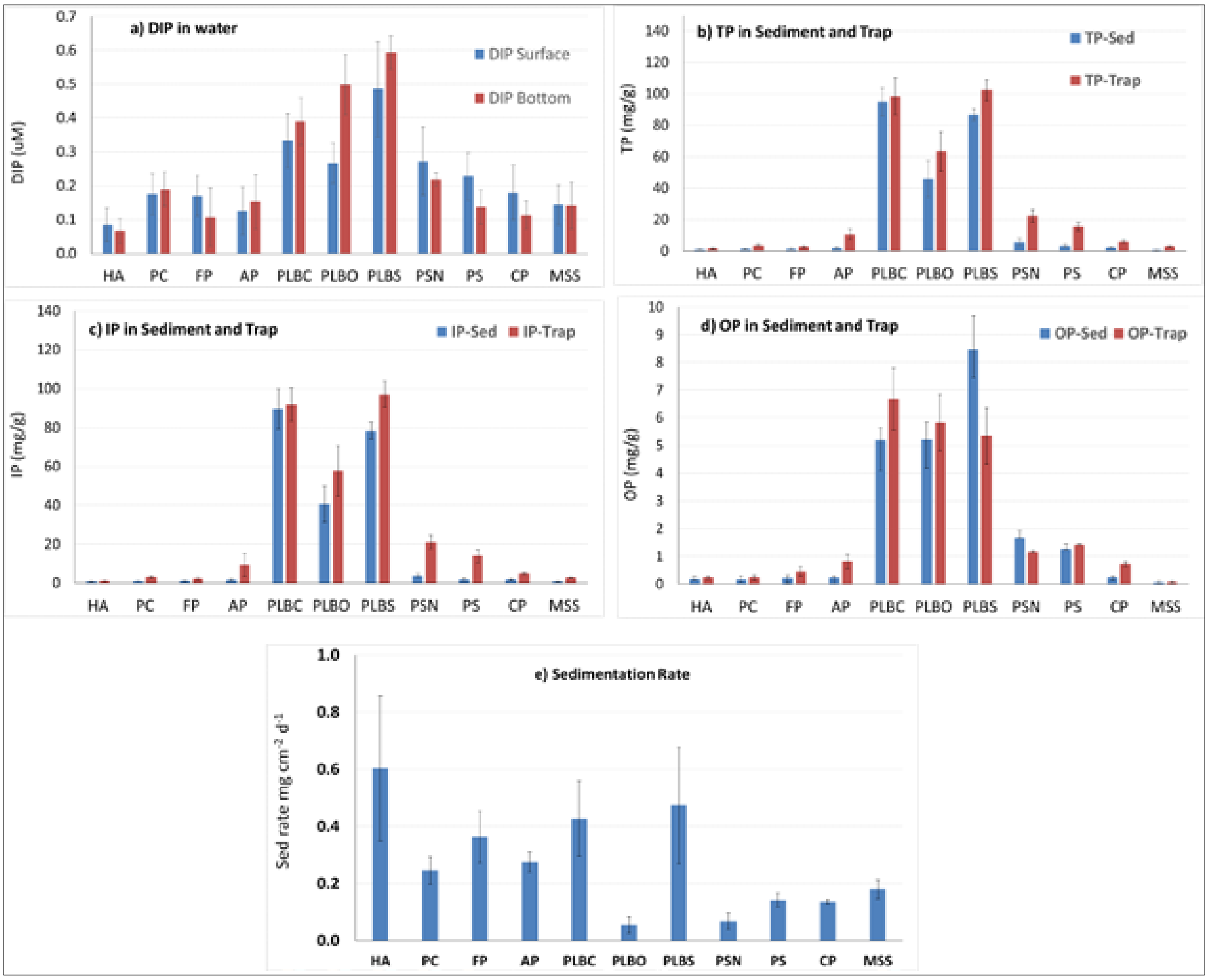

Figure 2. Sampling sites with (a): Mean dissolved inorganic phosphate (DIP) concentrations (µM) in surface and near-bottom water of the Gulf of Aqaba. b): Mean concentrations (mg g -1) of total phosphorus (TP) in trap-sediments and sediments (c): Mean concentrations (mg g-1) of inorganic phosphorus (IP) in trap-sediments and sediments. (d): Mean concentration (mg g -1) of organic phosphorus (OP) in trap-sediments and sediments. (f): Mean sedimentation rate (mg cm-2 d-1) in the near-bottom sediment traps along the Jordanian coast of the Gulf of Aqaba. Error bars in all figures represent the standard deviation of the measured parameter in all measured months. Sampling sites are demonstrated in figure 1 above.

Table 1. Percentage of TP and IP in trap-sediments were calculated as P_2O_5 and TCP.

Site	Mean concentration mg g $^{-1}$			IP/TP	OP/TP	TP as		IP as	
	(TP)	(IP)	(OP)	(%)	(%)	%P_2O_5	%TCP	% P_2O_5	%TCP
HA	1.39	1.15	0.24	82.97	17.03	0.32	0.70	0.26	0.58
PC	3.29	3.05	0.24	92.70	7.30	0.75	1.65	0.70	1.53
FP	2.61	2.15	0.46	82.50	17.50	0.60	1.31	0.49	1.08
AP	10.32	9.34	0.81	90.45	7.84	2.37	5.17	2.14	4.68
PLBC	98.43	91.73	6.70	93.20	6.80	22.56	49.28	21.02	45.93
PLBO	63.33	57.50	5.83	90.80	9.20	14.51	31.71	13.18	28.79
PLBS	102.33	96.99	5.34	94.78	5.22	23.45	51.24	22.23	48.56
PSN	22.21	21.02	1.18	94.67	5.33	5.09	11.12	4.82	10.53
PS	15.22	13.80	1.42	90.65	9.35	3.49	7.62	3.16	6.91
MP	5.69	5.01	0.73	88.08	12.79	1.30	2.85	1.15	2.51
MSS	2.77	2.70	0.07	97.54	2.44	0.64	1.39	0.62	1.35

Table 2. Percentage of TP and IP in sediments when calculated as P_2O_5 and TCP.

Site	Mean concentration mg g $^{-1}$			IP/TP	OP/TP	TP as		IP as	
	(TP)	(IP)	(OP)	(%)	(%)	%P_2O_5	%TCP	% P_2O_5	%TCP
HA	0.81	0.62	0.19	77.01	23.11	0.19	0.41	0.14	0.31
PC	1.18	1.02	0.16	86.00	13.93	0.27	0.59	0.23	0.51
FP	1.26	1.06	0.20	83.90	16.08	0.29	0.63	0.24	0.53
AP	1.79	1.57	0.22	87.76	12.29	0.41	0.90	0.36	0.79
PLBC	94.86	89.67	5.19	94.53	5.47	21.74	47.50	20.55	44.90
PLBO	45.74	40.53	5.21	88.61	11.39	10.48	22.90	9.29	20.29
PLBS	86.78	78.31	8.48	90.23	9.77	19.89	43.45	17.94	39.21
PSN	5.40	3.74	1.66	69.24	30.76	1.24	2.70	0.86	1.87
PS	3.04	1.77	1.26	58.41	41.63	0.70	1.52	0.41	0.89
MP	2.03	1.79	0.24	88.10	11.86	0.47	1.02	0.41	0.90
MSS	0.69	0.64	0.05	92.52	7.73	0.16	0.34	0.15	0.32

The low percentage of P_2O_5 in trap-sediments and sediments as compared with raw phosphate rock is attributed to the dissolution and dilution of phosphate dust in the Gulf of Aqaba before the phosphate dusts are deposited on the bottom. It is worthy to mention that these P_2O_5 percentages in sediments (0.16 - 21.74%) are in general agreement with the values (1.47-18.62%) reported by Abu-Hilal (1999). In the present study however, the average P_2O_5 in sediments (6.82%) is 16 times higher than the mean value (0.42%) reported by Mulqui (1978) and 11 times higher than the highest value (0.65 %) reported by Freemantle et al. (1976) who used 2M HCl at 80°C to extract phosphorus from sediment. The difference between their values and the present values can be attributed in part to the more rigorous perchloric acid method used for the extraction of sedimentary phosphorus in the present study. However, other factors may be also relevant, notably to the sampling sites PLBS, PLBC, and PLBO in this study which are closer to the phosphate loading berth than the corresponding sampling sites of Freemantle et al. (1978). In addition, there has been a major increase in the amount of phosphate exported over the past decade's period compared to the 1978 period. By 2008, more than 3.5 million tons (on average) are exported through Aqaba port each year (Abu-Hilal et al., 2008). The average annual export increased to 4.5 million tons between 2010 and 2018 (Jordan Phosphate Mines Company, 2020).

3.7 Currents

The current was measured in the study area at different depth levels between 3 and 27 m during the study period. The results show (Fig. 3) clearly that the current at 3 and 5m depth was southeastward (147° ± 18.8°) and (181° ± 32.9°) with mean speed of (14.6 ± 13.4 cm s^{-1}) and (7.3 ± 5.1 cm s^{-1}), respectively.

The current at 7 m depth was weak (3.1 ± 4.3 cm s^{-1}) with unstable direction. Below this depth, the current started to change its direction to the northeast, which assumes that the 7 m depth layer is a transition layer between two layers that have different directions. The currents between 9 and 25 m remained northeastward but with a tendency to decrease in magnitude from 4.5 ± 4.0 cm s^{-1} at 9 m to 2.7 ± 2.4 cm s^{-1} at 25 m. Because the sediment samples were collected at about 10 m depth, the current data above this depth has been used to examine the relation between the phosphate-phosphorus distribution (TP, IP, and OP). This suggests that the current which is assumed to affect the distribution of phosphorus concentration was mainly southeastward of the PLB which means that the effect of this prevailing current should be reflected on the distribution of phosphate-phosphorus, and one therefore should find more phosphorus to the south of PLB than to north. Almost all the results of TP, IP concentrations confirm postulation that there are higher concentrations of

TP and IP around PLB, and the concentrations of these two forms of phosphorus are higher in the stations located to the south of the PLB than those located to the north of it, despite the fact that the distances between the PLB and the north sites are less than the distances between the PLB and the south sites, as indicated by (Table 3).

3.8 Correlations between TP and (IP and OP) in trap-sediments and sediments

The results of this analysis (Fig. 4) show that the concentrations of TP in trap-sediments and sediments have high and significant correlation with IP (R^2=0.996) compared with moderate correlation with OP (R^2=0.579 for trap-sediments and 0.659 for sediments).

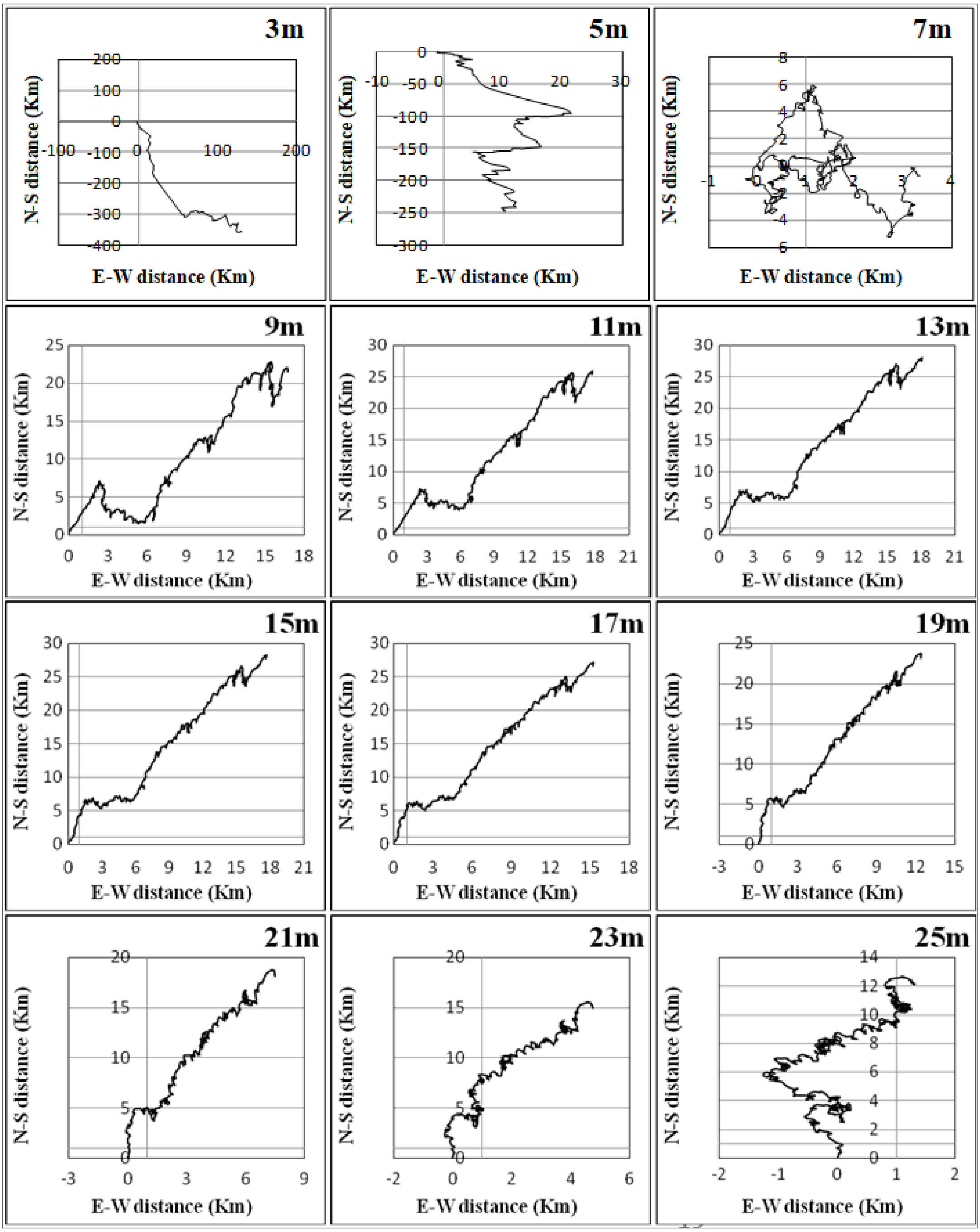

Figure 3. Progressive vector diagram of current at different depth levels in the study area during the study period.

Table 3. Effect of location and distance between the mean of sampling sites and Phosphate Loading Berth center (PLBC) on the distribution and concentration (mean values) of the measured parameter.

Site	Location relative to PLBC	Distance from PLBC (m)	TP mean	IP mean
HA	north	2974	0.81	0.62
PC	north	2515	1.18	1.02
FP	north	1407	1.26	1.06
AP	north	710	1.79	1.57
PLBC	-------	0	94.86	89.67
PLBO	west	50	45.74	40.53
PLBS	south	235	86.78	78.31
PSN	south	1516	5.40	3.74
PS	south	2904	3.04	1.77
MP	south	3537	2.03	1.79
MSS	south	5390	0.69	0.64

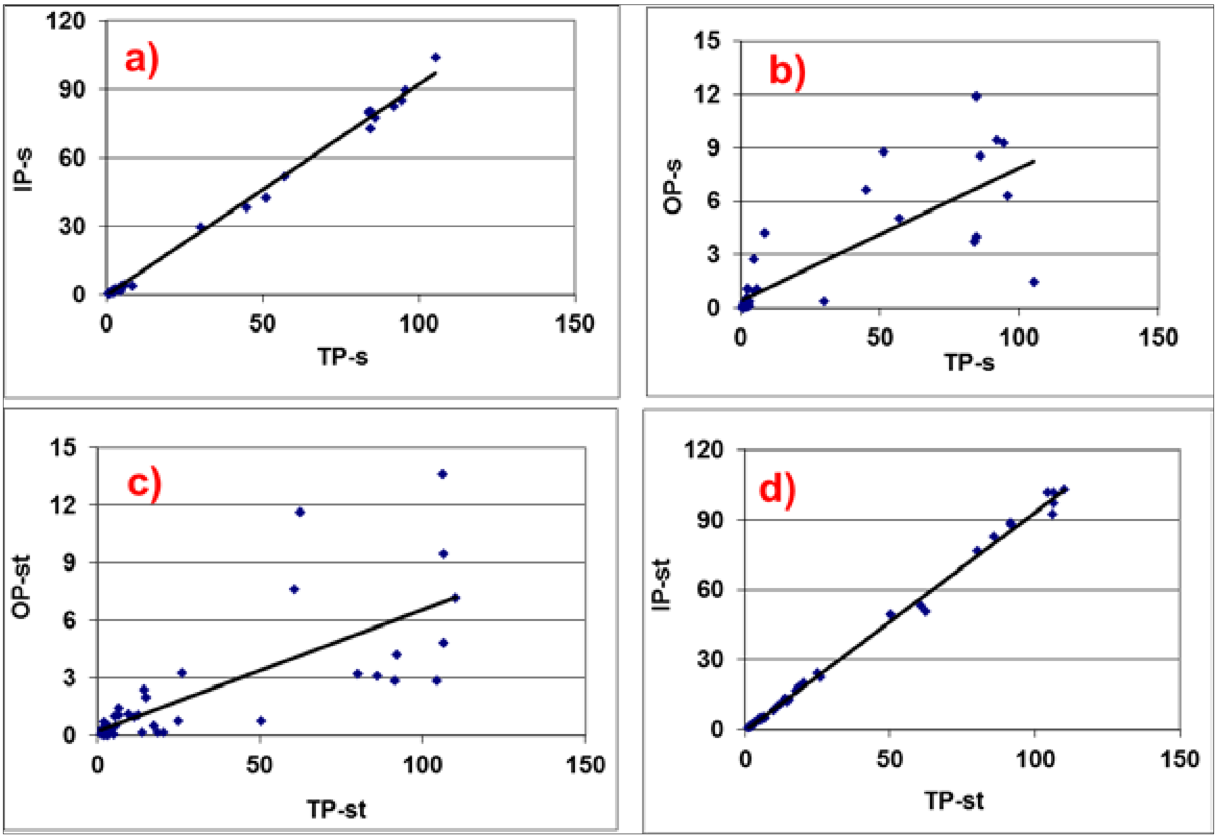

Figure 4. (a) Correlations between total phosphorus (TP) and inorganic phosphorus (IP) in sediments (s); (b) Correlations between total phosphorus (TP) and organic phosphorus (OP) in sediments (s); (c) Correlations between total phosphorus (TP) and inorganic phosphorus (IP) in trap sediments (st) (d) Correlations between total phosphorus (TP) and organic phosphorus (OP) trap sediments (st).

4. Conclusions

Based on the results of the presents study it was possible to conclude that:

1. The sediments of the study area near the Aqaba phosphate loading berth (PLB) are polluted with various species of phosphorus.

2. The concentrations of TP, IP, and OP are highest in the sediments of the sites that are in closer to the PLB area. These high concentrations are mainly attributed to the higher sedimentation rate at the PLB area due to ship loading and due to the high rate of sedimentation from the dust air borne of the heavy (high specific gravity) phosphate particles that settle down onto the bottom sediments during loading of the exported raw phosphate and due to the high rate of sedimentation from the air borne dust. The statistical analysis for these species in trap-sediments and sediments within the PLB area are significantly different from those of all other sites. The abnormally high concentrations of the total phosphorus at the Phsphate Loading Berth sites and the relatively lower concentrations at the other sites indicate that phosphate pollution is located mainly near PLB area and attributed to the high sedimentation rate of phosphate dust particles at this area

3. The concentration of TP, IP and OP are higher in the

stations located to the south of the PLB compared to those located to the north of it. This is because of the eastward and southeastward of prevailing currents and winds.

4. Inorganic Phosphorus (fluorapatite) is the major species of phosphorus in the study area and represents 82.5-97.5 %, 77-94.5 %, of the TP in trap-sediments and sediments, respectively. The concentrations of TP in trap-sediments and sediments have high and significant correlation with IP. The concentrations of TP as P_2O_5 in the sediments represent 0.16-21.74% and 0.34 - 47.50% as TCP, while those of IP represent 0.14-20.55% as P_2O_5 and 0.31-44.90 % as TCP.

5. The low percentage of P_2O_5 in trap-sediments and sediments as compared with raw phosphate rock is attributed to the of the partial dissolution of the inserted raw phosphate (fluorapatite) dust particles in the water of the Gulf of Aqaba and to the effect of the dilution of the deposited phosphate particles by mixing with the sediments. Due to this partial dissolution in the water of the Gulf of Aqaba, highest concentrations DIP in surface (Sw) and near-bottom (Bw) water were recorded at Phosphate Loading Berth Sites. The higher concentrations of DIP around PLB tend to decrease with increasing distance from this site. However, the increase in DIP concentrations in the water is not significant to cause significant increase in the DIP concentrations in the water of the Gulf of Aqaba to abnormal or the hazardous levels.

6. The lowest sedimentation rate in the offshore site (PLBO) at a distance of about 200 m of the PLB is explained by the fact that prevailing currents do not carry phosphate particles in the direction of this site. The deeper position of sedimentation trap (~ 20 m) is another possible reason.

Acknowledgments

The Authors would like to acknowledge the help of the technical staff of the Marine Science Station/Aqaba in the lab and field work. This work was mainly supported by the Deanship of Scientific Research/Yarmouk University.

References

Abed, A. (2012). Review of Uranium in the Jordanian Phosphorites: Distribution,Genesis and Industry. Jordan Journal of Earth and Environmental Sciences 4:35-45.

Abu-Hilal, A. (1985). Phosphate pollution in the Jordan Gulf of Aqaba. Marine Pollution Bulletin 16: 281-285.

Abu-Hilal, A. (1987). Distribution and forms of sedimentary phosphorus near a phosphate-polluted coral reef area in Jordan Gulf of Aqaba, Red Sea. Dirasat 14: 137-150.

Abu-Hilal, A. (1999). Environmental issues in the Gulf of Aqaba: Jordanian perspective. Proceedings; Conference on “The 1999 Maritime Safety Coloquim” Pendragon Applied Research, Nova Scotia, Ca- nada. Aqaba, Jordan. Topic 12: 1-8.

Abu-Hilal, A., Rasheed, M., and Al-Najjar, T. (2008). Potential environmental impact of dissolution of raw phosphate in sea water of the Gulf of Aqaba. Taylor and Francis, Chem. and Ecol. 24: 51-59.

Al-Moghrabi, S.M., and Horani, H.K. (1998). Distribution and seasonal variation on nutrients in the Gulf of Aqaba. Dirasat 25: 226-239.

Al-Rousan, S. (1998). Sediment role in nutrient cycle within the coral reefs of the Gulf of Aqaba, Red Sea. Master Thesis. Yarmouk University. Jordan.

Al-Rousan, S., Rasheed, M., and Badran, M. (2004). Nutrient diffusive fluxes from sediments in the northern Gulf of Aqaba, Red Sea. Scientia Marina 68 (4): 483-490.

Al-Rousan, S., Rasheed, M., Al-Horani, F, and Manasrah, R. (2006). Geochemical and Textural Properties of Carbonate and Terrigenous Sediments along the Jordanian Coast of the Gulf of Aqaba. Journal of Oceanography 62: 839-849.

Al-Rousan, S., Al-Taani, A., and Alrashdan, M. (2016). Effects of pollution on the geochemical properties of marine sediments across the fringing reef of Aqaba, Red Sea, Marine Pollution Bulletin 110, 546–554.

APHA (1971). Standard Methods for the Examination of Water and Wastewater. New York 13: 1-874.

Aspila, K.I., Agemian, H. and Chau, A.S.Y. (1976). A semi-automated meth- od for the determination of inorganic, organic and total phosphate in sediments. Analyst 101: 187-197.

Bani-Awwad, O.M. (2002). The airborne dust and its environmental impact on scle- ractinian coral settlement in the Gulf of Aqaba. Master Thesis. Yarmouk University. Jordan.

Badran, M., and Al Zibdah M (2005). Environmental Quality of Jordanian Coastal Surface Sediment, Gulf of Aqaba, Red Sea. Ambio 34: 615-620.

English, S., Wilkinson, C. and Baker, V. (1994). Survey Manual for Tropical Marine Resources. Australian Institute of Marine Science. Townsville.

Freemantle, M.H., Hulings, N.C., Mulqi, M. and Watton, E.C. (1978). Calcium and phosphate in the Jordan Gulf of Aqaba. Marine Pollution Bulletin 9: 79-80.

Grasshoff, K., K. Kremling and M. Ehrhardt, (1999). Methods of Seawater Analysis. Wiley-Vch, Weinheim, 600 pp.

Hamdan, F.S. (1999). Comparison between the effect of phosphate on the growth and productivity of the branched coral, stylophora pistillata (Esper, 1797) and massive coral, platygyra deadalea (Ellis and Solander, 1786) in the Gulf of Aqaba, Master Thesis. Yarmouk University. Jordan.

Hulings, N.C. and Abu-Hilal, A.H. (1984). The temporal distribution of nutrients in the surface waters of the Jordan Gulf of Aqaba. Dirasat 10: 91-105.

Jordan Phosphate Mines Company, 2020. Personal Communication. Aqaba Office, Aqaba, Jordan.

MSS Report (2020): Environmental appraisal of the Jordanian coast of the Gulf of Aqaba, unpublished report. Marine Science Station, 88p. Aqaba, Jordan.

Mulqui, M.W. (1978). The effect of phosphate rock dust on the calcium, magnesium and phosphate levels in the Jordan Gulf of Aqaba. Master Thesis. Jordan University. Jordan.

Murphy, J. and Riley, J.P. (1962). A modified single solution method for the determination of phosphate in natural waters. Analaltica Chimica Acta 27: 31-36.

Rasheed, M., Badran, M., Richter, C., and Huettel, M. (2002). Effect of reef frame- work and bottom sediment on nutrient enrichment in coral reef of the Gulf of Aqaba. Marine Ecology Progress Series 239: 277-285.

Rasheed, M., Al-Rousan, S. A., and Badran, M.I. (2005). Phosphate enrichment in the northern Gulf of Aqaba: Regulation by carbonate sediments and impact on nitro- gen elevation. Taylor and Francis, Chemistry and Ecology 114:99–208.

Rasheed, M., Manasrah, R., Al-trabeen, K., and Kellie Dixon

L. (2018). Impact of artificial lagoons on seawater quality: evidence from 7 years of physicochemical seawater monitoring. Environmental Monitoring Assessment 21: 244.

Schuhmacher, H., Koss, H. and Brieda, F. (1982). Report on the environmental imp- act of industrial activities in the southern region. Environmental and development studies for the southern region of Jordan. Ministry of Municipal and Rural Affairs (Jordan), and German Agency for Technical Cooperation (GTZ), PP 1-135.

JJEES

JJEES (2023) 14 (3): 232-240
ISSN 1995-6681

Jordan Journal of Earth and Environmental Sciences

The Use of Remote Sensing and GIS for Mapping Silica Sand Deposits in Jordan

Muheeb Awawdeh, Eman Alkhateeb, Nazem Al-Radaideh*

Dept. of Earth & Environmental Sciences, Yarmouk University-Irbid Jordan

Received 31st May 2022; Accepted 11th May 2023

Abstract

Mining is critical to human development. Today it necessitates cutting-edge spatial technology due to a variety of environmental and social constraints. With free remote sensing data such as Sentinel-2 data from the Copernicus program and EO-1 Hyperion, new study opportunities emerge. The goal of this study was to use remote sensing and GIS techniques to map the silica sand deposits in Jordan. The Energy and Minerals Regularity Commission (EMRC) conducted a field investigation for three sites of silica sand (Ras El-Naqab, Qa' El-Disi, and the Al-Jayoshia).

Samples were collected from the exposed surfaces for laboratory analysis (mineralogy and chemistry). The results confirmed that Si and quartz are the main components of the samples. The spectral signature of silica sand from sampled sites was derived from EO-1 Hyperion and Sentinel-2 images and then compared with the spectral signature from the USGS library.

The spectral signature of the EO-1 Hyperion images was close to the USGS library's spectral signature and then used as training sites for mapping silica sand using the Sentinel-2 images. The end results a map of silica sand in Jordan based on both types of images. The study revealed that southern Jordan is abundant in silica sand more than documented in the literature. The integration of hyperspectral data (EO-1 Hyperion) and multispectral data (Sentinel-2) is an effective approach in mapping Earth minerals meaning that full coverage of the study area with hyperspectral images is not required, eventually, cost savings.

Keywords: *Hyperspectral remote sensing, Silica sand, Sentinel-2, Spectral signature*

1. Introduction

The interpretation and processing of satellite images to extract information and parameters, either qualitatively or statistically, is a cornerstone of remote sensing (Royal Cultural Center, 1995). Multispectral and hyperspectral spectral imaging are two different types of spectral imaging that use comparable technologies. They're different imaging methods in that they each have their own set of applications. Remote sensing for species mapping, mineral exploration, food engineering, agriculture, atmospheric studies, ecology, health care, and agriculture are examples of such application spaces. The acquisition of visible, near-infrared, and short-wave infrared images is part of multispectral remote sensing (USGS, 2021).

A multispectral image gathers image data across the electromagnetic spectrum within a specified wavelength range. At these distinct wavelengths, the various materials collected reflect and absorb differently. It is feasible to distinguish between materials using this imaging technology based on their spectrum reflection fingerprints as seen in these remotely sensed images. Direct identification is impossible as a result. For example, Shamsham and Idries (2022) estimated surface soil particles using remote sensing-based data in Al-Ghab Plain, Syria. Hyperspectral remote sensing, on the other hand, analyzes a broad spectrum of light rather than assigning primary colors to each pixel. Its main purpose is to extract a spectrum from each pixel in a scene image to locate objects, detect processes, and identify materials.

There are numerous benefits to using remote sensing with their various types, including (1) large existing databases such as Landsat, Sentinel-2, and Hyperion, (2) the ability to obtain regional perspectives of large areas, (3) ease of integrating information from multiple sensors, (4) no difficulty or danger in covering remote areas, (5) availability of sophisticated computer analysis software, (6) a wide range of energy ranges (such as infrared, UV, and so on), and (7) It is low-cost and fast. Land use mapping, weather forecasting, environmental and natural hazards investigations, and geological mapping are just a few of the applications that have benefited from remote sensing (Chasmer et al., 2020).

In numerous geological research, such as assessing the damage caused by earthquakes, volcanoes, landslides, floods, and melting in polar regions, remote sensing data is a significant source of information. In mineral exploration research, remote sensing (multispectral and hyperspectral data) has become a significant method for finding and mapping minerals without having to go to the field (Treitz & Rogan, 2004; Ayodele & Ajigo 2020). Jordan is rich in minerals that are well-identified by the Natural Resources Authority (NRA), of Jordan. However, the exact borders of the deposits are not delineated as areas, but as points. Therefore, this study came to use advanced technologies (remote sensing and GIS) to map the areas covered by silica

* Corresponding author e-mail: nazem@yu.edu.jo

sand exactly, which may ease the process of accessibility and investment. Besides, such techniques are rarely used in mineral exploration locally. The study approach is based on utilizing the properties of the electromagnetic spectrum in Sentinel-2 and EO-1 Hyperion imageries.

Silica sand in Jordan is described by its exposure on the surface, effectively mineable by open-pit mining, and low content of impurities and heavy minerals, which means it has a high level of purity that facilitates processing and thus gets high value-added products (Madanat et al., 2014). Silica sand deposits in Jordan, belong to the Disi Sandstone Formation of the lower Ordovician age, and the Kurnub Sandstone Formation of the Lower Cretaceous age which are exposed in the south of Jordan (Figure 1). Some of extremely noteworthy silica sand deposits are known from five sites: Ras El-Naqab, Qa' El-Disi, Wadi Siq, Al Jayoshia area, and Petra. The most important one is Ras El-Naqab (Mohsen, 2016). The layers of silica sand exposed in the areas of Ras El- Naqab and Qa' El-Disi are within the sediments of the Lower Ordovician period while the areas of Al-Jayoshia and wadi Al-Siq are in the rocks of the Lower Cretaceous period. The NRA has estimated the reserves in the Ras El- Naqab area at more than 10 billion metric tons. The local consumption of silica sand is limited to the industries of white cement, ceramics, and plumbing molds (Khoury, 2012).

Madani (2011) mapped the basement rocks and the barite mineralization exposed at the El Hudi area in Egypt using the processed short-wave infrared bands of ASTER. Results showed that garnetiferous muscovite granites have gray image signatures on 5/4 band ratio images whereas pegmatite's and postgranitic dykes have black image signatures. Results at the northern Death Valley site (Kruse, 2013) established that data from the EO-1 Hyperion SWIR spectrometer (2.0 – 2.4 µm) can be used to produce useful mineralogic information. Comparison of EO-1 Hyperion data to airborne hyperspectral data (AVIRIS) shows that EO-1 Hyperion provides the ability to remotely map basic surface mineralogy. Minerals mapped at this site include calcite, dolomite, muscovite, hydrothermal silica, and zeolites. Kryniecka (2015) detected sandbars for a selected section of the Lower Vistula (Wisła) river with the use of Sentinel-2 Level 2A optical images. For multispectral images, water indices were used to separate sandbars from water. The analyses have shown that it is possible to detect sandbars in the river channel based on Sentinel-2 satellite data. Harahsheh (2016) used Landsat-8 to identify and map the lithological units in northern Jordan. She applied different methods including false color analysis and different band ratios to minimize noise fraction, image classification, filtering, and lineament extraction. Ibrahim et al., (2018) utilized samples from drill holes extracted from Tiebaghi, New Caledonia. The chemical composition and the hyperspectral reflectance of each sample were obtained. With the resulting regression models, the mineral chemistry of an outcrop in the vicinity of the drill holes was mapped by a scene of Sentinel-2. The work showed the great potential of free satellite imagery in mapping the chemical characteristics of minerals and rocks. El Atillah et al. (2019) investigated the use of different satellite data, such as Sentinel-2A multispectral imagery, in order to direct the prospection program in an efficient manner, saving both time and cost. The image processing methods of Landsat 7, 8, and the Advanced Spaceborne Thermal Emission and Reflection Radiometer (ASTER) were used to create methods for Sentinel-2A images. The assembly of lithological, structural, and hydrothermal alteration data gave an idea of the mineralogy of the study area. The validity of the results was tested by comparison with the field data and the geological maps of the studied site. Aldiri et al, (2020) provided a comprehensive review of the use of the Landsat-8 and Sentinel-2 multispectral sensors in mineral exploration. Landsat-8 and Sentinel-2 data presented effective and accurate mapping tools for mineral exploration. Both sensors identified iron oxides and Al-OH absorption features, in addition to silicate and carbonate minerals. Alsaleh (2022) assessed the spatial variability of soil properties using hyperspectral remote sensing data, N. Jordan.

2. Methodology

2.1 Samples collection and analysis

Thirty surface samples of silica sand were collected from three sites (Ras El-Naqab, Qa' El-Disi, and Al Jayoshia) defined by the Natural Resources Authority (Figure 1). The samples were randomly selected from each site based on the researcher's field observations taking into consideration surficial features such as color and grain size. The location of samples was recorded by Garmin GPSMAP 60Cx handheld GPS. The samples were undergone wet sieving 100 g of dried sediment was sieved with an aperture of 63 microns to separate mud. The fine fraction (less than 63 m) was then analyzed using an XRD and XRF Analyzer X-ray diffraction and X-ray fluorescence to determine their chemical and mineralogical composition.

2.2 Remote sensing datasets

The current work used the multispectral Sentinel-2A and hyperspectral EO-1 Hyperion remote sensing datasets to map silica sand in Jordan. Eighteen Sentinel-2 images were required to cover the whole country, whereas only 3 Hyperion images were found that partially covered the study area (Figure 2) but were quite enough given the presence of silica sand in the south of Jordan (Table 1).

Table 1. Characteristics of Sentinel-2 and EO-1Hyperion images.

	Sentinel-2	EO-1 Hyperion
Type of sensor	Multispectral	Hyperspectral
Number of bands (range of wavelength)	13 bands (0.4-2.2µm)	242 bands (0.4-2.5 µm)
Number of used scenes	18	3
Spatial resolution	10 - 60 m	30 m
Swath width	290 km	7.7 km

All Sentinel-2 images acquired in August 2020, were downloaded with a radiometric resolution of 16 bits. All bands except band 10 were used for analysis. The sites of sampling areas were used as ground truth points for the classification of the remote sensing data.

2.3 Image pre-processing

Image pre-processing prior to the analysis included geometric correction, radiometric correction, atmospheric correction, mosaicking, and stacking. However, Sentinel-2 images did not need any type of correction. Because of the pseudo projection of EO-1 Hyperion images, the images have been re-projected to UTM Zone 36N. To calibrate and compensate for inaccuracies in the pixel values, the flash tool in ENVI software was used to perform radiometric and atmospheric corrections, because of the improperly calibrated detector on the EO-1 Hyperion push broom scanner (HARRIS, 2021).

Hyperspectral imagers are usually affected by noise during acquisition and transmission (Skauli, 2011; Acito et al. 2011). The imagery, contaminated by noise, may cause failures in information extraction and image interpretation. EO-1 Hyperion has 242 bands. The bands (1-7), (58-76), (225-242) are already set to values of zero (Barry, 2001). Other bands such as (121-126), (167-180), (222-224) have severe noise that corresponds to strong water vapor absorption, so those bands are typically removed from processing (Dat et al, 2003). Minimum noise fraction was used to determine the inherent dimensionality of image data to segregate noise in the data, and to reduce the computational requirements for subsequent processing (Boardman and Kruse, 1994).

Sentinel-2A didn't need radiometric or atmospheric correction because ESA supplies a processor that performs atmospheric correction on Sentinel-2 data with worldwide coverage (Sentinel Hub, 2021). A color composite (stacking) was used to create a single raster from multiple bands of Sentinel-2A and EO-1 Hyperion, then, the mosaic was created using Seamless Mosaic workflow in ENVI software.

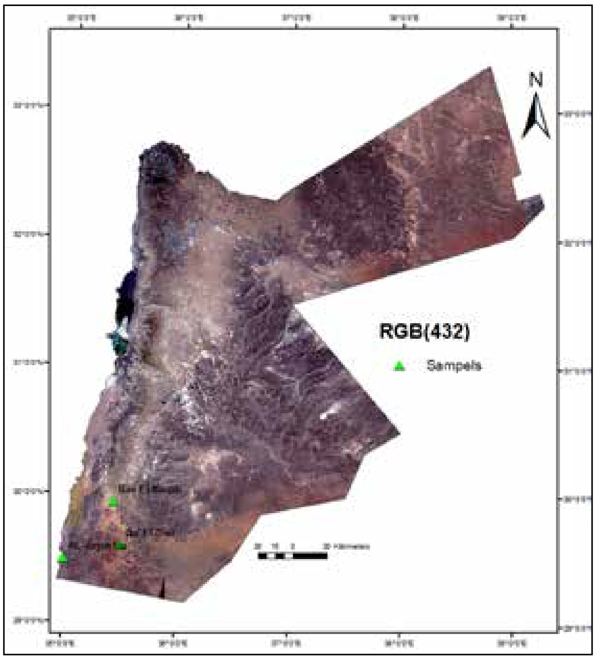

Figure 1. Samples of silica sand superimposed on Sentinel-2 image of Jordan (RGB 432).

2.4 Remote sensing data analysis

Three EO-1 Hyperion images only that were acquired during the period 2002-2005 were available for free from the USGS (2021) (Table 2 and Figure 2).

Table 2. EO-1 Hyperion scenes used to read the electromagnetic signatures.

Scene number	Id	Acquisition Date
Scene1	EO1H1740382003253110KZ	10 September 2003
Scene2	EO1H1740392002275110PY	2 October 2002
Scene3	EO1H1740392005258110KK	15 September 2005

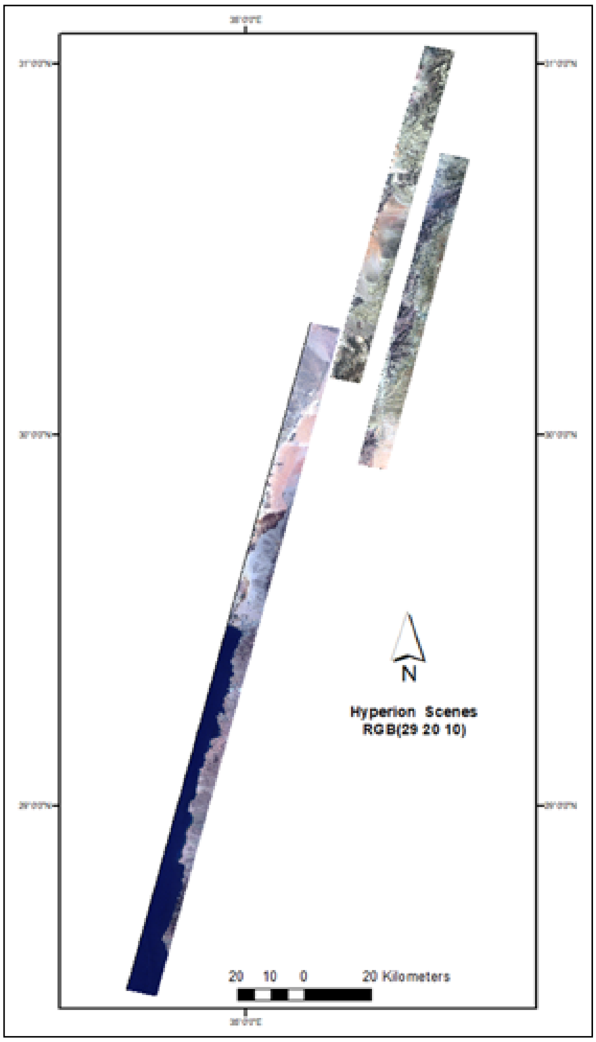

Figure 2. The EO-1 Hyperion images used in this study with true colors RGB (29 20 10).

Kuching (2007) found that the most accurate method of classification of hyperspectral images was maximum likelihood classification. Therefore, the Hyperion images were classified using this method. But, before classification, matched filtering (MF) was adopted to find the abundances of endmembers such as silica sand using partial unmixing.

This method of supervised categorization necessitates the selection of a target region (ROI). The sampled sites were in the province of Scene 1 (Table 2) of the EO-1 Hyperion images from which the electromagnetic spectrums were captured and used as training sites for the mapping silica sand zones in all scenes of the Hyperion images. The color composite RGB (29 20 10) was chosen to read the electromagnetic signature. The large number of bands in the EO-1 Hyperion images increases the ability to distinguish the desired minerals. The more bands, the more pronounced the curve (the signature).

On the other hand, it was not possible to identify the characteristic features clearly by using Sentinel-2. This is due to the very limited number of bands and the adsorption/reflectance features were concentrated at 0.9 micrometers and less (ESA, 2021). To distinguish silica sand, absorption will appear around wavelengths of 1.4 micrometers and 1.9 micrometers due to its hydroxide content (Viallefont-Robinet, 2019).

A supervised classification has been used. Scene 1 of the EO-1 Hyperion satellite was classified based on its mineral content according to Alnawafleh et al. (2013) mineral map (Figure 3). The second step was to utilize the zones of silica sand identified from the Hyperion images as training sites for Sentinel-2 images, bearing in mind that Sentinel-2 images cover the whole country. The ROI (region of interest) was taken in Sentinel-2 Jordan images based on the silica sand zones that were obtained from the classification of the Al-Jayoshia image of the EO-1 Hyperion satellite, in addition to the locations of samples of clay minerals that were taken and analyzed during the field study and based on the mineral map of Jordan from Alnawafleh et al. (2013).

To affirm the results of the mapping, validation was carried out using two methods:(1) Validation using electromagnetic spectrum: The spectral signature from mapped zones of silica sand based on either image (Sentinel-2 or Hyperion) could be compared with the signature of the silica from the USGS library, and (2) Validation using Google Earth: Google Earth was used to ascertain the nature of the areas where silica sand was mapped by visual interpretation and feasible areas for mining. A further step was carried out for comparison purposes. The mapped zones of silica sand from both sensors were intersected to find out the extent of overlap areas

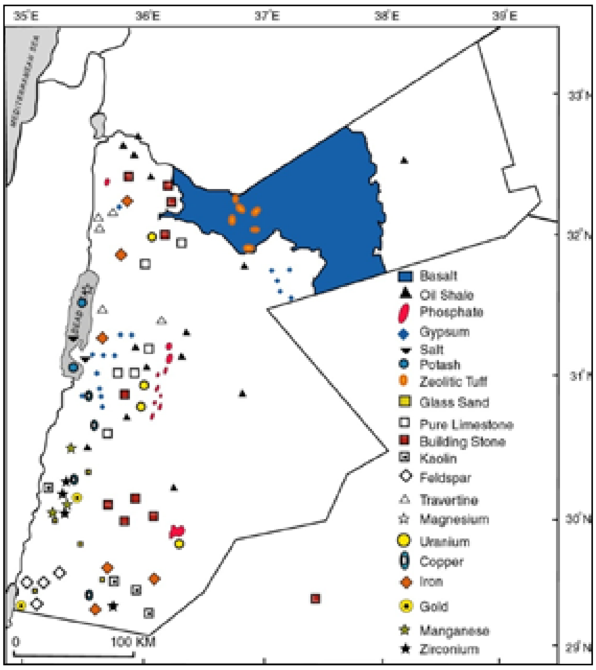

Figure 3. Jordan mineral map (Alnawafleh et al. 2013).

3. Discussion and Results.

3.1 XRF and XRD analysis

The fine fraction of silica sand from Ras El-Naqab region, Qa' El-Disi, and AL-Jayoshia (Figure 4) contain quartz as the major mineral and very minor amounts of calcite, berlinite, despujolsite, and algodonite, (Table 3 and Figure 4). These minerals have been previously linked to quartz.

Table 3. XRF analysis for Ras El-Naqab, Al Jayoshia, and Qa' El-Disi sediments.

Sample site	SiO_2%	Cl %	CaO%	TiO2%	K_2O%	Fe_2O_3%	Total%
Ras El-Naqab	97.8	0.85	0.37	0.39	-----	0.15	≈100%
Qa' El-Disi	83.45	-------	4.23	1.69	4.96	5.54	≈100%
Al Jayoshia	86.97	6.87	4.32	0.60	-----	1.16	≈100%

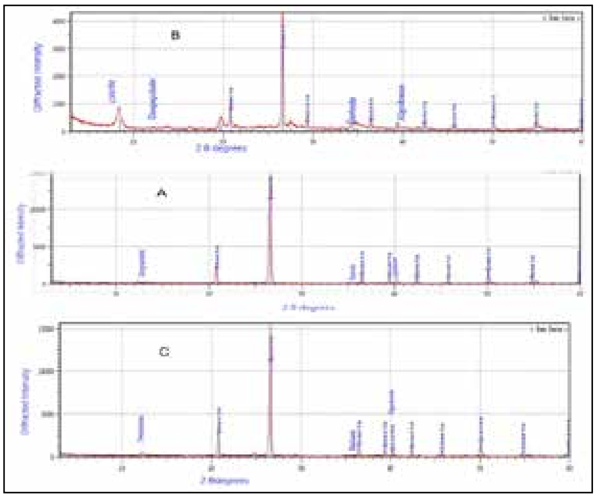

Figure 4. XRD diagram analysis of <63 micron for (A) Ras El-Naqab, (B) Qa' El-Disi and (C) Al-Jayoshia sediments.

The highest proportion of SiO2 was found in Ras El-Naqab (97.80%), followed by the AL-Jayoshia area (86.90%) and Qa' El-Disi (83.45%). The existence of impurities, notably in the form of iron, titanium, and calcium oxides, accounts for the varying percentages. The most important impurity is iron oxide. These contaminants present significant challenges in a variety of applications, including the manufacture of colorless or optical glass, optical fibers, and high-purity ceramics (Chammas, 2001).

Iron (III) oxide percentages were 0.15 % in Ras El-Naqab, 1.16 % in Al-Jayoshia, and 5.54 % in Qa' El-Disi. These results are good, according to EMRC (2014), when considering that the samples were obtained from the surface and evaluated in their natural state, which usually yields a larger percentage of contaminants. Chemical weathering rises as a result of this exposure, resulting in a high percentage of impurities such as iron (III) oxide.

When comparing our XRF findings to those of the EMRC study (2019), it is found that SiO2 and Fe2O3 concentrations are98.72 % and 0.04 %in Ras El- Naqab, and 96.5 % and 0.025 %, in Qa' El-Disi, respectively. The higher quality of silica sand obtained by the Energy and Minerals Regularity Commission (EMRC) is attributed to the subsurface samples and samples washing by wet sieving.

3.2 Spectral signature analyses of silica sand

The signatures of three silica sand samples from Ras El-Naqab, Al-Jayoshia, and Qa' El-Disi are represented by Sentinel-2 spectrum signatures (Figure 5). The signature from these samples was insufficient to determine the mineral composition because it only reveals the spectrum absorption of the iron (III) oxide.

Therefore, high spectral resolution data is essential for this purpose, and hyperspectral technologies play a vital role in this regard. One sample only (Al-Jayoshia) was found within the spatial extent of EO-1Hyperion images (scene 1), just (Figure 1). Its spectral signature was extracted and compared to that of silica sand from the USGS library (Figure 6).

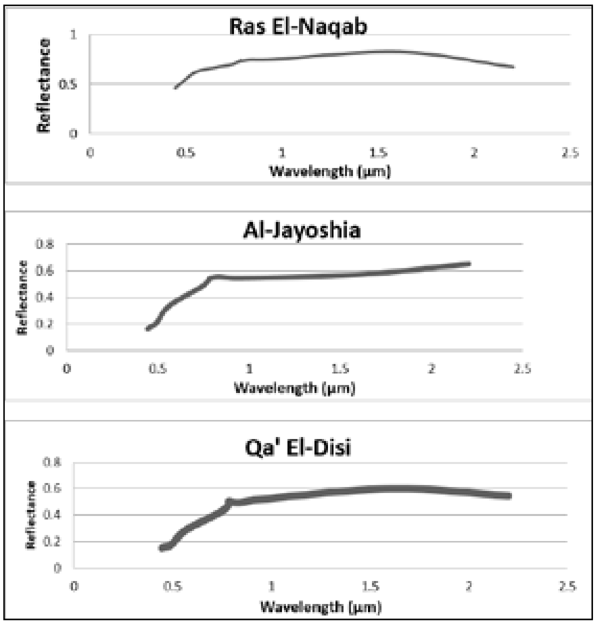

Figure 5. Sentinel-2 spectral signature for Ras El-Naqab (a), Al-Jayoshia (b), and Qa' El-Disi (3). The absorption around 0.9 µm is for iron oxide.

The signature in EO-1 Hyperion images had spectral signature behavior similar to that of a silica sand signature from the USGS library, taking into account the number of bands, where the library spectrum has 3375 bands, whereas the number of Hyperion bands used is only 175 due to the removal of some bands with zero values. The USGS library's silica sand spectral profile (Figure 6) revealed absorptions at 0.9, 1.4, and 1.9 µm. The quantity of the element or compound that triggered the absorption is proportional to the depth of absorption. The absorption patterns around 0.9 to 1.2 µm were caused by iron oxide concentration, whereas the absorption features around 1.4 to 1.9 µm were caused by the hydroxide ion trapped in the silicates, which form a characteristic silica sand impression. Clay minerals and carbonate content are responsible for the absorption properties between 2 and 2.5 µm. The EO-1 Hyperion image (scene 1) was categorized using the extracted spectral signature based on the maximum likelihood method (Figure 7). The identified zones of silica sand from this process were used as training sites for Sentinel-2 classification (Figure 8). The last step was using the mapped zones of silica sand from the Sentinel-2 images as training sites for the classification of the other two EO-1Hyperion images (Scene2) and (Scene3) (Figure 9). The spectral signatures of the mapped zones of silica sand from these images were investigated against signatures of silica sand from the USGS library.

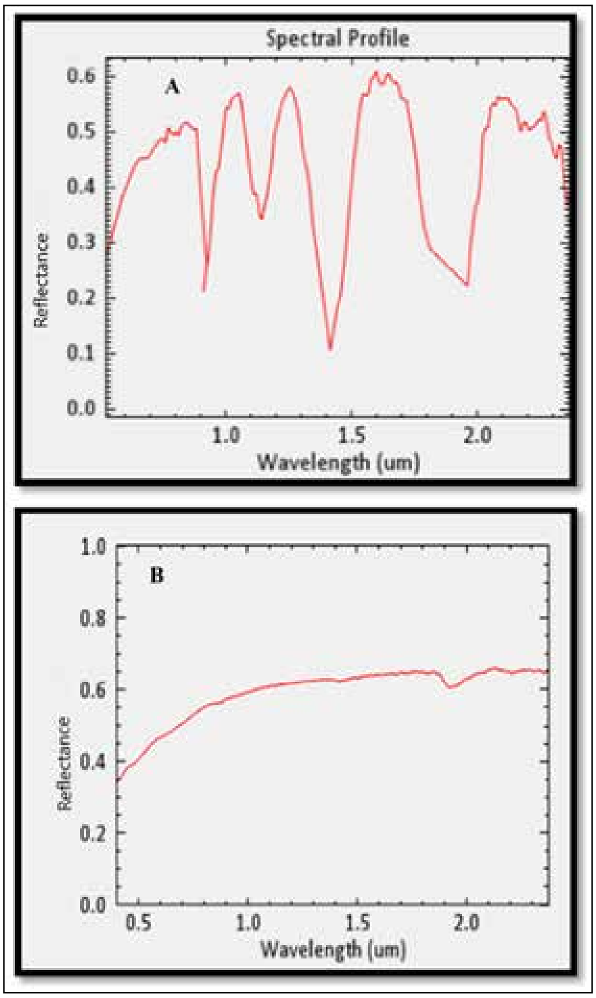

Figure 6. Spectral signature from (Scene1) EO-1Hyperion image (A) with spectral signature for silica sand from the USGS library (B).

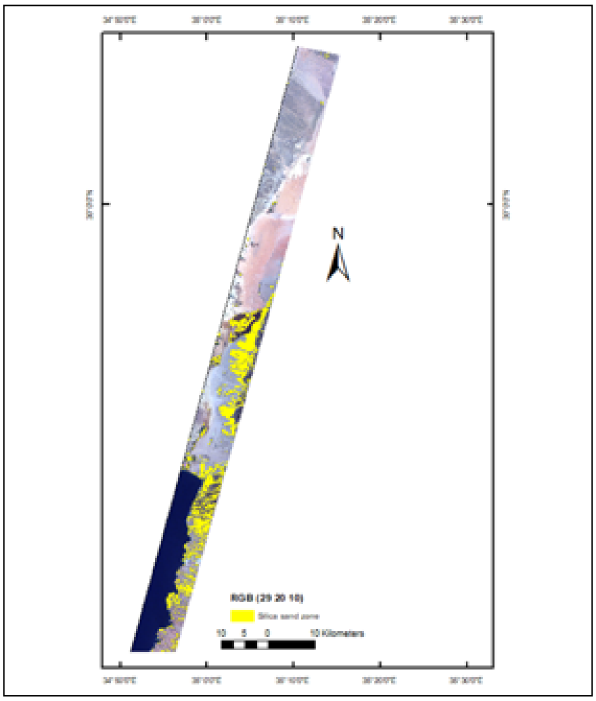

Figure 7. Silica sand zones (yellow color) extracted from EO-1 Hyperion image (scene 1).

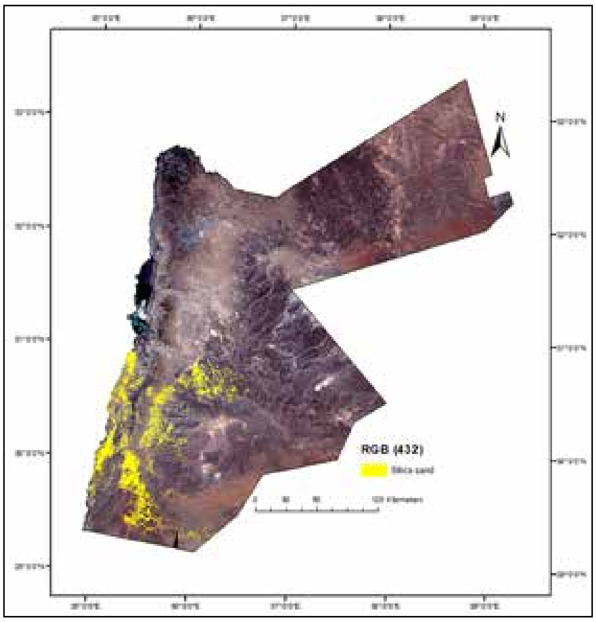

Figure 8. Silica sand zones (yellow color) extracted from Sentinel-2.

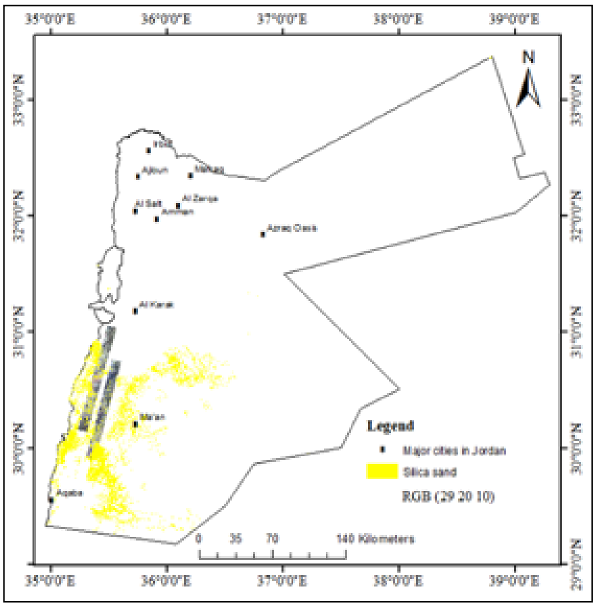

Figure 9. Silica sand zones extracted from Sentinel-2 image overlay EO-1Hyperion images (scenes 2 and 3).

3.3 Validations of results

The existence of silica sand was established by comparing the electromagnetic spectrum from the mapped areas, which was very close to the silica sand spectrum from the USGS library (Figure 6). An overlay GIS operation was carried out to calculate the degree of intersection (overlap) between zones of silica sand from both images (Hyperion and Sentinel) (Figure 10) and found to be 57 %, meaning that these zones were identified using both images. Considering the disparities in image characteristics (spectral and spatial resolution), the outcome is considered acceptable. Moreover, the visual interpretation of Google Earth images (Figure 11) indicated the presence of silica sand in terms of texture, brightness, topography, and land cover. Size from 50.2 km^2 in Qa' El-Disi to 72.7 km^2 in Ras El-Naqab.

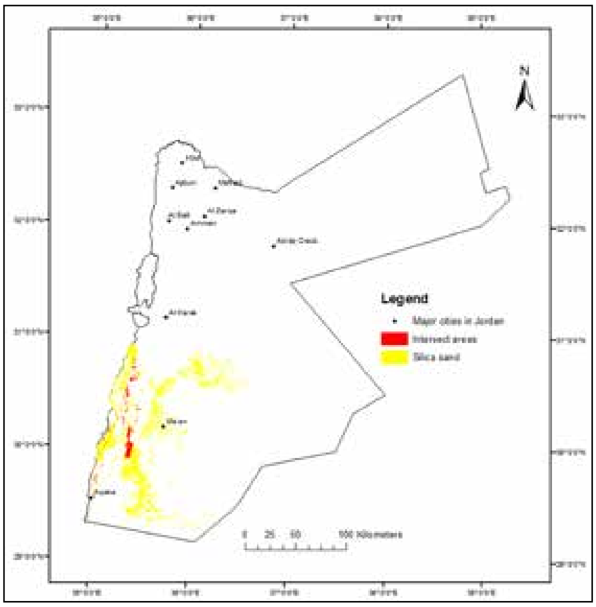

Figure 10. Intersect results of overlaying Sentinel-2 and EO-1 Hyperion silica sand zones.

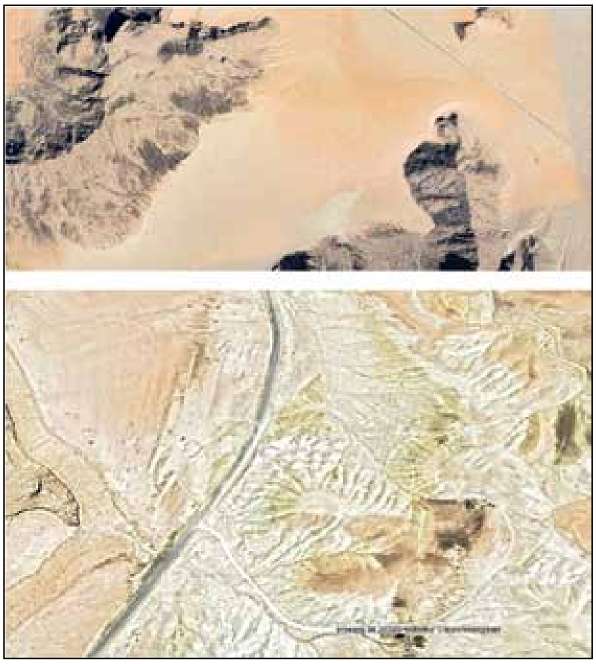

Figure 11. Prospected silica sand in Qa' El-Disi (a), Ras El-Naqab (b) as seen on Google Earth.

Matched Filtering (MF) is also used to validate work by finding the abundance of user-defined endmembers using a partial unmixing. This technique maximizes the response of the known endmember and suppresses the response of the composite unknown background, thus matching the known signature. It provides a rapid means of detecting specific materials based on matches to library or image endmember spectra and does not require knowledge of all the endmembers within an image scene. The Matched Filter (MF) produced a succession of grayscale images, one for each endmember specified (silica sand). In the Hyperion photos, silica sand appeared as bright zones in the higher tail of the histogram (Figure 12).

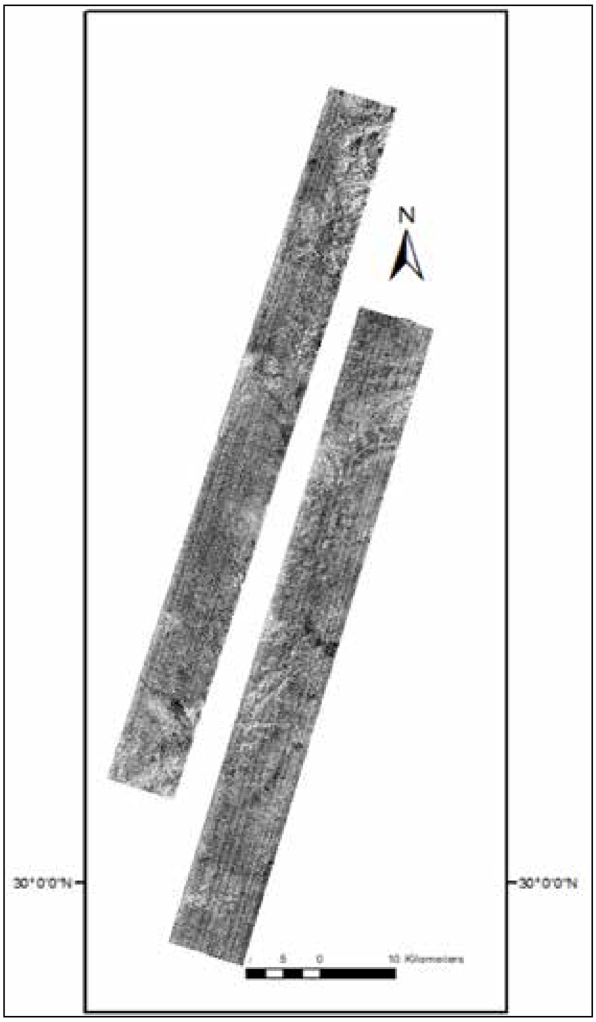

Figure 12. Matched filter for hyperspectral images from EO-1 Hyperion (scene 2, scene 3). Silica sand determine as endmember. Silica sand appears as bright areas.

3.6 The spectral signature and mineral content

The absorptions areas at 0.9 µm and 1.2 µm refer to the iron oxide, 1.4 µm and 1.9 µm absorption are due to OH or H2O, whereas absorptions at 2.0 µm to 2.5 µm at Qa' El-Disi, Al-Jayoshia, and Ras El-Naqab are indicators of clay minerals and carbonates. These absorptions in Qa' El-Disi, Al-Jayoshia, and Ras El-Naqab were different in the electromagnetic spectrum (Figure 13). The greatest iron oxide ratio was 5.45% in Qa' El-Disi, followed by 1.16% in Al-Jayoshia, and 0.15 % in Ras El-Naqab. These iron oxide ratios are related to color changes in samples that can be seen visually. The higher the iron oxide level, the darker the red hue. The shape of the signature is affected by the quantity of iron oxides; the higher the concentration of iron oxides, the higher the absorption rate at 0.9 µm to 1.2 µm in the spectral profile. The absorption of iron oxides in the Al-Jayoshia area appears to be stronger than in the Ras El-Naqab area. The quantity of clay minerals and carbonate also impacts the shape of the spectral signature; the more clay minerals and carbonate in the spectral profile, the higher the absorption rate at 2.0 µm to 2.5 µm. The percentage of carbonate in Ras El-Naqab was 0.37 %, while it was 4.32 %in Al-Jayoshia.

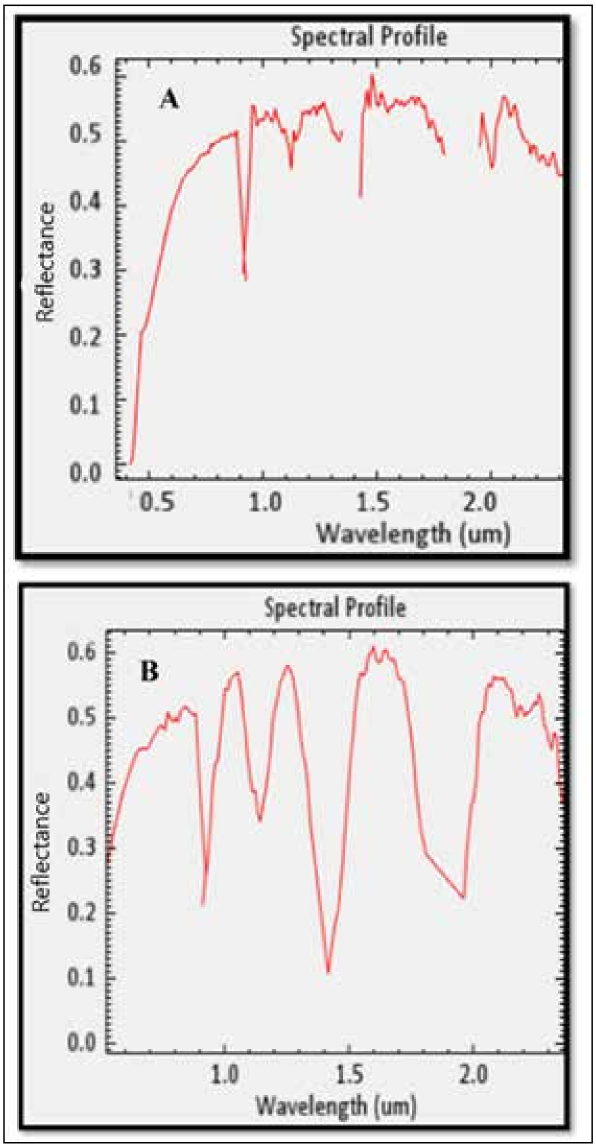

Figure 13. (A) Spectral profile for Ras El-Naqab. The absorption rate was down to (2.9) at0.9µm and to (4.4) at 2.3µm, (B) Spectral profile for the Al-Jayoshia region, with absorption down to (2.1) at 0.9µm and to (3.4) at 2.3µm.

4. Conclusion

This study employed hyperspectral EO-1 Hyperion and multispectral Sentinel-2 data to map silica sand in Jordan. Field investigation of known verified locations was used as reference points (Ras El-Naqab, Qa' El-Disi, and the Al-Jayoshia) in this study. Samples were obtained from the exposed surfaces and analyzed in the lab for the mineral content and chemical composition. The results showed that quartz and silica are the predominant materials in all sites. The presence of impurities such as iron oxides accounts for the varied percentages, which are 0.15 % in Ras El-Naqab, 1.16 % in Al-Jayoshia, and 5.54 % in Qa' El-Disi. These results are good indicators that Ras El- Naqab is promising for silica sand mining.

This study proved the potential integration of hyperspectral data and multispectral remote sensing data for mineral mapping. The large coverage by Sentinel 2 benefited from the high-resolution data from Hyperion for mapping the silica sand in Jordan. Despite the noise in the EO-1 Hyperion data, we were able to map silica sand after image processing. This approach saves the cost of acquiring costly hyperspectral data. However, map validation samples must be collected and analyzed. Remote sensing data is useful for mapping minerals because it eliminates field labor and the need for large numbers of samples to be analyzed. The study confirmed the presence of silica sand in south Jordan, but with larger areas, at least 89 km2. This may shed light on the potential mining of silica sand which can be used in a variety of industries due to its surface exposure and ease of access, as well as its high purity in the natural environment. Other tools and techniques can be applied in this area of research such as the use of thermal bands field spectroradiometer.

Acknowledgments

This research has been supported by the Deanship of Scientific Research and Graduate Studies, Yarmouk University (Grant No. 52/2020).

References

Ababsa, M. ed., 2013. Atlas of Jordan: history, territories and society (Vol. 32).

Abdelhamid, G., 1990. The Geology of Jabal Umm Ishrin Area (Wadi Rum), Map Sheet No. 3049II. Bulletin 14, Natural Resources Authority, Geological Directorate. Map Division, Amman.

Abu Halima, K., 1993. Mineralogy, chemistry and industrial studies of Al-Yamaniyya clay deposits in Aqaba area. Unpublished M.Sc. Thesis, The University of Jordan, Amman.

Adiri, Z., Lhissou, R., El Harti, A., Jellouli, A. and Chakouri, M., 2020. Recent advances in the use of public domain satellite imagery for mineral exploration: A review of Landsat-8 and Sentinel-2 applications. Ore Geology Reviews, 117, p.103332.

Acito, N., Diani, M. and Corsini, G., 2011. Signal-dependent noise modeling and model parameter estimation in hyperspectral images," IEEE Transactions on Geoscience Remote Sensing, vol. 49, no. 8, pp. 2957–2971, Aug. 2011.

Al Kuisi, M., Abed, A.M., Mashal, K., Saffarini, G. and Saqhour, F., 2015. Hydrogeochemistry of groundwater from karstic limestone aquifer highlighting arsenic contamination: case study from Jordan. Arabian Journal of Geosciences, 8(11), pp.9699-9720.

Aladaileh, H., Al Qinna, M., Karoly, B., Al-Karablieh, E. and Rakonczai, J., 2019. An investigation into the spatial and temporal variability of the meteorological drought in Jordan. Climate, 7(6), p.82.

Al-Ansari, N., Ibrahim, N., Alsaman, M. and Knutsson, S., 2014. Water demand management in Jordan. Engineering, 6(1), pp.19-26.

Al-Homoud, A.S. and Tat, A.B., 1997. Engineering geology of the Aqaba-Ras El Naqab highway re-alignment, Jordan. Engineering geology, 47(1-2), pp.107-148.

Anthony, J.W., 1990. Handbook of mineralogy: Arsenates, phosphates, vanadates. Arsenates, phosphates, vanadates, 4. Mineral Data Pub.

Alsaleh, A. 2022. Assessing the Spatial Variability of Soil Properties Using Hyperspectral Remote Sensing Data, N. Jordan. M.Sc. Thesis. Department of Department of Earth and Environmental Sciences, Yarmouk University, Jordan.

Ayodele, O. and Ajigo, I. (2020). Geological Mapping and Gemstones prospecting in Deformed Precambrian Rocks, East of Okemesi Fold Belt, Southwestern Nigeria. Jordan Journal of Earth and Environmental Sciences, 11(4) 290-301.

Baker, M.B., 2017. The Application of Marble and Granite as Building Materials in Jordan. Jordan Journal of Civil Engineering, 11(2), pp.234-238.

Bannari, A., El-Battay, A., Bannari, R. and Rhinane, H., 2018. Sentinel-MSI VNIR and SWIR bands sensitivity analysis for soil salinity discrimination in an arid landscape. Remote Sensing, 10(6), p.855.

Barkley, M.C., Yang, H., Evans, S.H., Downs, R.T. and Origlieri, M.J., 2011. Redetermination of despujolsite, Ca3Mn4+ (SO4) 2 (OH) 6· 3H2O. Acta Crystallographic a Section E: Structure Reports Online, 67(9), pp.i47-i48.

Barry, P., 2001. EO-1/Hyperion science data user's guide, Level 1_B. TRW Space, Defense & Information Systems, Redondo Beach, CA, Rep. HYP. TO, 1.

Barry, R., Sawada, Y. and Kabeto, K., 1998. Crushing performance and contamination tdals of a tungsten carbide ring mill compared to agate grinding. Geoscience ReptShimane Univ (17), pp.1-9.

Bayook, A., 1992. Batn El Ghoul Deposits as a Potential Source for Aluminum (Doctoral dissertation, M. Sc. Thesis, University of Jordan).

Bender, F., 1974. Geology of Jordan. Berlin: Gebrüder Borntraeger.

BMS factories., 2019. [https://www.bm.com.sa/ar], [Date of visit12/13/2021].

Brimhall, G.H., Dilles, J.H. and Proffett, J.M., 2006. The role of geologic mapping in mineral exploration: Society of Economic Geologist Special Publication 12.

Boardman, J. W., and Kruse, F. A., 1994. Automated spectral analysis: A geological example using AVIRIS data, northern Grapevine Mountains, Nevada. Proceedings of the Tenth Thematic Conference on Geologic Remote Sensing, San Antonio, TX,9–12 May1994, (Ann Arbor, MI : ERIM), pp. 1 – 407 – 1 – 418 .

Castaldi, F., Palombo, A., Santini, F., Pascucci, S., Pignatti, S. and Casa, R., 2016. Evaluation of the potential of the current and forthcoming multispectral and hyperspectral imagers to estimate soil texture and organic carbon. Remote Sensing of Environment, 179, pp.54-65.

Chammas, E., Panias, D., Taxiarchou, M., Anastassakis, G.N. and Paspaliaris, I., 2001. Removal of iron and other major impurities from silica sand for the production of high added value materials. In Proceedings of the 9th Balkan Mineral Processing Congress, İstanbul.

Chasmer, L., Cobbaert, D., Mahoney, C., Millard, K., Peters, D., Devito, K., Brisco, B., Hopkinson, C., Merchant, M., Montgomery, J. and Nelson, K., 2020. Remote sensing of boreal wetlands 1: data use for policy and management. Remote Sensing, 12(8), p.1320.

Datt, B., McVicar, T.R., Van Niel, T.G., Jupp, D.L. and Pearlman, J.S., 2003. Preprocessing EO-1 Hyperion hyperspectral data to support the application of agricultural indexes. IEEE Transactions on Geoscience and Remote Sensing, 41(6), pp.1246-1259.

El Atillah, A., El Morjani, Z.E.A. and Souhassou, M., 2019. Use of the Sentinel-2A Multispectral Image for Litho-Structural and Alteration Mapping in Al Glo'a Map Sheet (1/50,000) (Bou Azzer–El Graara Inlier, Central Anti-Atlas, Morocco). Artificial Satellites, 54(3), pp.73-96.

ESA. 2021. [https://sentinel.esa.int/web/sentinel/missions/sentinel-2], [date of visit 20/10/2020].FIS.2020.

[https://www.fis.uni-bonn.de/en/recherchetools/Infobox/professionals/resolution/radiometric-resolution], [date of visit 10/2/2021].

Fomin, D.S., Valdes-Korovkin, I.A., Holub, A.P. and Yudina, A.V., 2019. Dry sieving analysis of soil by vibratory sieve shaker: modification and optimization. Bulletin of VV Dokuchaev Soil Science Institute, 96, pp.149-177.

FPDF. 2008. [www.fpdf.org], [date of visit12/6/2021].

Galvão, L.S., Formaggio, A.R., Couto, E.G. and Roberts, D.A., 2008. Relationships between the mineralogical and chemical composition of tropical soils and topography from hyperspectral remote sensing data. ISPRS Journal of Photogrammetry and Remote Sensing, 63(2), pp.259-271.

Haddadin, M., 1974. Possibilities of bentonite in Jordan. In Natural Resources Authority (NRA) Internal Report, p. 24.

Harahsheh, R., 2016. Geological mapping using remote sensing and GIS technique case study in Umm-Qais–Northern Jordan. MSc thesis. The Hashemite University, Zarqa, Jordan, p.65.

HARRIS.2021. [https://www. l3harrisgeospatial.com /docs/ Hyperionvegetationanalysistutorial.html], [date of visit 8/2/2021].

Harsanyi, J.C. and Chang, C.I., 1994. Hyperspectral image classification and dimensionality reduction: An orthogonal subspace projection approach. IEEE Transactions on geoscience and remote sensing, 32(4), pp.779-785.

Humboldt State University. 2019. [gsp.humboldt.edu], [date of visit 6/1/2020].

Ibrahim, K.M., Moh'd, B.K., Masri, A.I., Al-Taj, M.M., Musleh, S.M. and Alzughoul, K.A., 2014. Volcanotectonic evolution of central Jordan: Evidence from the Shihan Volcano. Journal of African Earth Sciences, 100, pp.541-553.

Khallouf A., Shamsham, S., and Idries Y. (2022). Estimation of Surface Soil Particles Using Remote Sensing-based Data in Al-Ghab Plain, Syria. Jordan Journal of Earth and Environmental Sciences, 13 (1): 26-36.

Khoury, H. N., 2019. Industrial rocks and minerals of Jordan: a review. Arabian Journal of Geosciences, 12(20), p.619.

Khoury, H. N., 2019. Review of clays and clay minerals in Jordan. Arabian Journal of Geosciences, 12(23), p.706.

Khoury, H., 2006. Industrial rocks and minerals in Jordan. Publications of the Deanship of Academic Research. The University of Jordan, Amman.

Khoury, H., 2012. Glass sand in Jordan. Publications of the Deanship of Academic Research. The University of Jordan, Amman.

Kruse, F.A (2004) Mineral Mapping with AVIRIS and EO-1 Hyperion. Proceedings of the 12th JPL Airborne Earth Science Workshop, Pasadena, CA, 2004.

Kryniecka, K. and Magnuszewski, A., 2020. USE OF SENTINEL-2 IMAGES FOR THE DETECTION OF SANDBARS ALONG THE LOWER VISTULA. Acta Scientiarum Polonorum. Formation Circumiectus, 19(2), pp.23-33.

Kurnia, G., Yulianto, B., Jamari, J., Bayuseno, A.P. and Tauviqirrahman, M., 2020, September. Contact mechanism between shaft, key, and crank in the sand sieving machine. In AIP Conference Proceedings 2262(1), p.030015. AIP Publishing LLC.

Machado, G.S., Groszewicz, P.B., de Freitas Castro, K.A.D., Wypych, F. and Nakagaki, S., 2012. Catalysts for heterogeneous oxidation reaction based on metalloporphyrins immobilized on Kaolinite modified with triethanolamine. Journal of colloid and interface science, 374(1), pp.278-286.

Madanat, G.M., Al-Omari, Y. and Sahawneh, J., Ministry OF Energy and Mineral Resources.

Makhlouf, I.M. and Abed, A.M., 1991. Depositional facies and environments in the Umm Ishrin Sandstone Formation, Dead Sea area, Jordan. Sedimentary Geology, 71(3-4), pp.177-187.

Migoń, P., Goudie, A., Allison, R. and Rosser, N., 2005. The origin and evolution of foot slope ramps in the sandstone desert environment of south-west Jordan. Journal of arid environments, 60(2), pp.303-320.

Montes-Herrera, J.C., Cimoli, E., Cummings, V., Hill, N., Lucieer, A. and Lucieer, V., 2021. Underwater Hyperspectral Imaging (UHI): a review of systems and applications for proximal seafloor ecosystem studies. Remote Sensing, 13(17), p.3451.

Nayak, P.S. and Singh, B.K., 2007. Instrumental characterization of clay by XRF, XRD and FTIR. Bulletin of Materials Science, 30(3), pp.235-238.

Nimry, Y. and Haddadin, M., 1970. Glass sand of Ras El-Naqab. Report on Phase, 1.

NOAA,2018. [https://repository. library. noaa. gov/view/noaa/ 25214/ noaa_25214_DS1.pdf], [date of visit 25/6/2018].

Potts, P.J. and West, M. eds., 2008. Portable X-ray fluorescence spectrometry: Capabilities for in situ analysis. Royal Society of Chemistry.

Richards, J.A. and Richards, J.A., 1999. Remote sensing digital image analysis (Vol. 3, pp. 10-38). Berlin: Springer.

Royal Cultural Center., 1995. Remote Sensing Uses. Third Jordanian Scientific Week, Volume II: Scientific Papers (Theme of Mineral Wealth).

Saffarini, G., 1988. Ferried elements abundance in the carbonate-hosted iron occurrences of Jordan. Dirasat (Science), 15(9), pp.190-202.

Saibi, H., Bersi, M., Mia, M.B., Saadi, N.M., Al Bloushi, K.M.S. and Avakian, R.W., 2018. Applications of remote sensing in geoscience. In, Hung. M., Wu, Yi-Hwa (eds) Recent Advances and Applications in Remote Sensing, pp.181-203.

Salimi, A., Ziaii, M., Amiri, A., Zadeh, M.H., Karimpouli, S. and Moradkhani, M., 2018. Using a feature subset selection method and support vector machine to address curse of dimensionality and redundancy in Hyperion hyperspectral data classification. The Egyptian Journal of Remote Sensing and Space Science, 21(1), pp.27-36.

Scanvic, J. Y., 1997. Aerospatiale remote sensing in geology. CRC Press, 280P.

Sentinel Hub.2021. [www.Sentinel-hub.com. [Date of visit 10/8/2020].

Shakrour, O., Tarawneh, K. and Jamal, D., 2010. Exploration, evaluation and investment opportunities of feldspar ore deposits in Jordan. In 6th Jordanian International Mining Conference.

Sharp, R.P., 1988. Earth science field work: Role and status. Annual Review of Earth and Planetary Sciences, 16(1), pp.1-20.

Sivakumar, M., Roy, P., Harmsen, K. Saha, S., 2004. Satellite remote sensing and GIS applications in agricultural meteorology. Proceedings of the Training Workshop 7-11 July, 2003, Dehra Dun, India.

Treitz, P. and Rogan, J., 2004. Remote sensing for mapping and monitoring land-cover and land-use change-an introduction. Progress in planning, 61(4), pp.269-279.

Skauli, T., 2011. Sensor noise informed representation of hyperspectral data with benefits for image storage and processing," Opt. Exp., vol. 19, no. 14, pp. 13 031–13 046, Jul. 2011.

Trinity College Dublin. 2018. [www.tcd.ie/Geology/ undergraduate/ fieldwork.php], [date of visit 20/9/2020].

USGS, 2022. [https://www.usgs.gov/science/remote-sensing-minerals], [date of visit 19/1/2022].

USGS.2021.[https://www.usgs.gov/centers/eros/science/usgs-eros-archive-earth-observing-one-eo-1-hyperion], [date of visit 12/1/2021].

Viallefont-Robinet, F., Bacour, C., Bouvet, M., Kheireddine, M., Ouhssain, M., Idoughi, R., Grignon, L., Munesa, E., Lemaître, F. and Rivière, T., 2019. Contribution to sandy site characterization: Spectro-directional signature, grain size distribution and mineralogy extracted from sand samples.

المملكة الأردنية الهاشمية

صندوق دعم البحث العلمي

الجامعة الهاشمية

المجلة الأردنية
لعلوم الأرض والبيئة

JJEES

مجلة علمية عالمية محكمة

المجلد (١٤) العدد (٣)

http:// jjees.hu.edu.jo/

ISSN 1995-6681

المجلة الأردنية لعلوم الأرض والبيئة

مجلة علمية عالمية محكمة

المجلة الأردنية لعلوم الأرض والبيئة: مجلة علمية عالمية محكمة ومفهرسة ومصنفة، تصدر عن عمادة البحث العلمي في الجامعة الهاشمية وبدعم من صندوق البحث العلمي - وزارة التعليم العالي والبحث العلمي، الأردن.

ترسل البحوث إلكترونيا إلى البريد الإلكتروني التالي:

رئيس تحرير المجلة الأردنية لعلوم الأرض والبيئة

jjees@hu.edu.jo

لمزيد من المعلومات والأعداد السابقة يرجى زيارة موقع المجلة على شبكة الانترنت على الرابط التالي:

www.jjees.hu.edu.jo

المملكة الأردنية الهاشمية صندوق دعم البحث العلمي الجامعة الهاشمية

JJEES

المجلة الأردنية لعلوم الأرض والبيئة

Indexed by Scopus

ELSEVIER

المجلد (14) العدد (3)

مجلة علمية عالمية محكمة تصدر بدعم من صندوق دعم البحث العلمي

ISSN 1995-6681 jjees.hu.edu.jo أيلول 2023